Shear-driven formation of olivine veins by dehydration of ductile serpentinite: a numerical study with implications for porosity production and transient weakening

Stefan M. Schmalholz[1], Evangelos Moulas[2], Ludovic Räss[3,4] and Othmar Müntener[1]

[1]Institute of Earth Sciences, University of Lausanne, 1015 Lausanne, Switzerland

[2]Institut of Geosciences and Mainz Institute of Multiscale Modeling (M[3]ODEL), Johannes Gutenberg University of Mainz, Germany

[3] Laboratory of Hydraulics, Hydrology and Glaciology (VAW), ETH Zurich, Zurich, Switzerland

[4]Swiss Federal Institute for Forest, Snow and Landscape Research (WSL), Birmensdorf, Switzerland

Email, corresponding author: Stefan Schmalholz (stefan.schmalholz@unil.ch)

Evangelos Moulas: evmoulas@uni-mainz.de; Ludovic Räss: luraess@ethz.ch;

Othmar Müntener: Othmar.Muntener@unil.ch

Key points:

- During viscous simple-shearing of serpentinite, en échelon olivine veins form by dehydration and grow in direction parallel to compression
- Dehydration is triggered by self-consistently modelled fluid pressure perturbations using a hydro-mechanical-chemical model
- Porosity production is controlled by three mechanisms: solid volume deformation, solid density variation and reactive mass transfer

Abstract

Serpentinite subduction and associated dehydration vein formation are important for subduction zone dynamics and water cycling. Field observations suggest that en échelon olivine veins in serpentinite mylonites formed by dehydration during simultaneous shearing of serpentinite. Here, we test a hypothesis of shear-driven formation of dehydration veins with a two-dimensional hydro-mechanical-chemical numerical model. We consider the reaction antigorite + brucite = forsterite + water. Shearing is viscous and the shear viscosity decreases with increasing porosity. Total and fluid pressures are initially homogeneous and in the serpentinite stability field. Initial perturbations in porosity, and hence viscosity, cause fluid pressure perturbations during simple shearing. Dehydration nucleates where fluid pressure decreases locally below the thermodynamic pressure defining the reaction boundary. During shearing, dehydration veins grow in direction parallel to the maximum principal stress and serpentinite transforms into olivine inside the veins. Simulations show that the relation between compaction length and porosity as well as the ambient pressure have a strong impact on vein formation, while the orientation of the initial porosity perturbation and a pressure-insensitive yield stress have a minor impact. Porosity production associated with dehydration is controlled by three mechanisms: solid volumetric deformation, solid density variation and reactive mass transfer. Vein formation is self-limiting and slows down due to fluid flow decreasing fluid pressure gradients. We discuss applications to natural olivine veins as well as implications for slow slip and tremor, transient weakening, anisotropy generation and the formation of shear-driven high-porosity bands in the absence of a dehydration reaction.

Plain language summary

Serpentinite is a rock that contains water which is bound within the crystal lattice. When serpentinite is plunging together with tectonic plates into the Earth mantle, the changing

pressure and temperature conditions cause chemical reactions which releases the water bound in the crystal lattice; a process called dehydration. A typical mineral that forms by serpentine dehydration is olivine. Dehydration is important for the global deep water cycle, since much water is transferred with tectonic plates into the mantle and is migrating back to the Earth surface after dehydration. However, many aspects of the water cycle remain still unclear, since dehydration during plunging of tectonic plates involves the incompletely understood interaction of three fundamental mechanical and chemical processes: mechanical deformation of the rock, porous flow of released fluid and chemical reactions involving changes in rock density. Here, we present a new mathematical model to investigate the coupled processes of rock deformation, fluid flow and dehydration reactions. We present computer simulations which can explain why the dehydration occurs in narrow and elongated regions which are termed veins. We propose that our simulations could explain the field observation of many small olivine veins in strongly sheared serpentinite.

1. Introduction

The dehydration of serpentinite at subduction zones is an important process for the global deep water cycle (e.g., Peacock, 1990; Pettke and Bretscher, 2022; Ulmer and Trommsdorff, 1995; Rupke et al., 2004), for the dynamics and seismicity at subduction zones (e.g., Bloch et al., 2018; Hacker et al., 2003) or for arc magmatism due to hydration of the mantle wedge (e.g., Hebert et al., 2009; John et al., 2012). More generally, the interaction of mineral reactions, fluid flow and rock deformation is important for a variety of geodynamic processes, such as chemical and volatile cycling (e.g., Bebout, 2014) or reaction-induced weakening of faults and shear zones (e.g., Labrousse et al., 2010; Sulem and Famin, 2009), as well as for practical applications such as natural carbon storage (e.g., Matter and Kelemen, 2009) or geothermal energy exploitation (e.g., Pandey et al., 2018). However, many aspects of the coupling of mineral reactions, fluid flow and rock deformation are still unclear.

Indirect observations that have been attributed to serpentinite dehydration at subduction zones are aseismic episodic tremor and slow-slip (ETS) phenomena (e.g., Behr and Bürgmann, 2021; Burlini et al., 2009; Tarling et al. 2019). These phenomena are commonly thought to result from episodic fault slip, likely facilitated or promoted by pulses of fluid release associated with fluid pressure variations (e.g., Audet et al., 2009; Connolly, 1997; Frank et al., 2015; Gomberg et al., 2010; Shelly et al., 2006; Taetz et al., 2018). For example, such slow-slip occurs on the plate interface in Cascadia at 30 to 40 km depth (e.g., Gomberg et al., 2010) and for temperatures probably between 400 and 500 °C (e.g., Tarling et al., 2019 and references therein). However, how the dehydration reaction, the associated fluid release and the volumetric and shear deformation of the involved rocks are coupled and actually cause the episodic slow-slip phenomena remains elusive.

Direct observation of the dehydration of serpentinite at subduction zones is not possible in nature. However, field observations in areas with abundant exposed serpentinites

at variable pressure and temperature may provide insight into incipient dehydration stages. In the European Alps, exposed serpentinites, which experienced variable peak pressures and temperatures, are abundant in many regions. Examples are the antigorite serpentinites of Saas Zermatt (Western Alps) or of the Erro-Tobbio unit (Voltri massif, Ligurian Alps, Italy; e.g., Hermann et al., 2000; Peters et al., 2020; Plümper et al., 2017; Scambelluri et al. 1991, Scambelluri et al., 1995; Kempf et al., 2020). These serpentinite bearing regions are key areas that preserve ductile and brittle structures that are related to fluid release. The antigorite serpentinites of the Erro-Tobbio unit exhibit olivine-bearing veins and the metamorphic olivine most likely results from the breakdown of antigorite and brucite (Fig. 1; e.g., Hermann et al., 2000; Plümper et al., 2017; Scambelluri et al., 2004). The serpentinites were initially formed by hydration of subcontinental mantle which was exposed to the Tethyan ocean floor during pre-Alpine extension (e.g. Scambelluri et al., 1995). Subsequently, these serpentinites transformed to antigorite serpentinites during prograde metamorphism associated with Alpine subduction (e.g. Scambelluri et al., 2004; Fig. 2). During subduction, the serpentinites, containing likely few olivine, have been sheared, which generated antigorite serpentinite mylonites (e.g. Scambelluri et al., 1995; Fig. 2). The exhumed antigorite mylonites are dissected by en-échelon olivine veins (e.g. Scambelluri et al., 1995; Fig. 1). The olivine-bearing antigorite serpentinites exposed in the Erro Tobbio region, hence, indicate that during subduction the antigorite serpentinites crossed the brucite-out reaction, enabling olivine formation, but never crossed the antigorite-out reaction before exhumation (e.g. Scambelluri et al., 1995; Fig. 2E). Most likely, the observed olivine veins were formed by the breakdown of mainly brucite when the subducting and actively deforming antigorite serpentinite crossed the pressure and temperature conditions of the brucite-out reaction (Fig. 2E). The olivine veins occur in two settings: as minimally deformed veins within little deformed, variably serpentinized peridotite and as deformed veins within strongly deformed antigorite

serpentinite, described as a serpentinite mylonite (Fig. 1; e.g., Hermann et al., 2000; Plümper et al., 2017). These serpentinite mylonites are cut by en échelon olivine veins, which in turn are dissected by multiple sets of olivine-bearing shear bands (Hermann et al., 2000). Plümper et al. (2017) suggested that the association of undeformed and sheared veins attests that dehydration-induced vein formation was synchronous with ductile deformation in the enclosing serpentinite mylonites. Furthermore, Hermann et al. (2000) hypothesized that (i) multiple sets of olivine shear bands provide evidence for continuous deformation, (ii) sheared olivine-rich veins are probably very weak due to continuous solution and precipitation in the presence of a fluid phase, (iii) fluid produced by the dehydration reaction was (partially) trapped in the serpentinite mylonite and (iv) serpentinite mylonites are not only zones with highly localized deformation but also zones of focused fluid flow. These hypotheses for olivine vein formation imply certain mechanical, hydrological and chemical mechanisms, but these hypotheses have not been tested with theoretical models based on the concepts of continuum mechanics and thermodynamics. Recently, Huber et al. (2022) presented a hydro-chemical (HC) model to study the formation of olivine veins in dehydrating serpentinite. However, they do not consider any solid-mechanical aspects of olivine vein formation and do, hence, not consider volumetric or shear deformation of the serpentinite and associated fluid pressure changes. Therefore, we cannot apply their model to test the hypothesis of shear-driven olivine vein formation.

Here, we test the hydrological, mechanical and chemical feasibility of a hypothesis for the formation of observed olivine veins in serpentinite mylonites with a new two-dimensional (2D) hydro-mechanical-chemical (HMC) model. The hypothesis is (Fig. 2): During viscous shearing of serpentinite, the magnitudes of ambient pressure and temperature were close to the magnitudes required for triggering the dehydration reaction from serpentinite to olivine (Figs. 2E and 3A). The effective viscosity of serpentinite was spatially variable, for example

due to variable porosity or heterogeneities in mineralogy (Fig. 2A). Weak domains, with lower viscosity, cause pressure variations in the sheared serpentinite and pressure is locally smaller than the ambient pressure. If the pressure decreases locally below the reaction pressure, then the dehydration reaction is triggered in these domains. The dehydration forms olivine and signficantly increases the porosity locally, which in turn increases the size of weak domains, consisting of an olivine-fluid mixture. The dehydration region forms vein-like structures that grow in a direction parallel to the maximal compressive stress without any fracturing (Fig. 2A and B). After fluid has escaped the olivine-rich region, the olivine-rich veins, observable in the field, have formed (Fig. 2C). We test this hypothesis with a 2D HMC model because such models are suitable to theoretically study the coupling between chemical reactions, fluid flow and rock deformation (e.g., Kolditz et al., 2015; Poulet et al., 2012). Such coupled models have been applied to study a variety of geodynamic processes, for example, reaction-driven cracking during serpentinization (e.g., Evans et al., 2020), porosity evolution and clogging during serpentinization (e.g. Malvoisin et al., 2021), the impact of dehydration on earthquake nucleation (e.g., Brantut et al., 2011), the impact of shear heating and associated chemical rock decomposition on thrusting (e.g., Poulet et al., 2014) or reactive melt migration (e.g., Aharonov et al., 1997; Baltzell et al., 2015; Bessat et al., 2022; Keller and Katz, 2016; Schiemenz et al., 2011). We apply here an extension of a HMC model that was previously used to model the dehydration reaction: brucite = periclase + water (Schmalholz et al., 2020). Here, we elaborate this HMC model and consider a simple MgO-SiO_2-H_2O (MSH) system for the reaction: antigorite + brucite = forsterite + water (Fig. 3). For simplicity, we consider an isothermal system and a fixed chemical composition so that the reaction antigorite + brucite = forsterite + water is balanced everywhere in the model domain.

The main aim of our study is to investigate the fundamental coupling of dehydration reactions, fluid flow and rock deformation, for which a simplified model is useful. Particular

aims of our study are (1) to test the hypothesis for the shear-driven formation of olivine veins in antigorite serpentinite and (2) to quantify the mechanisms that control the evolution and production of porosity during dehydration of ductily deforming rocks.

2. Mathematical model

2.1. Porous medium densities

We consider a simple MSH system and the reaction antigorite ($Mg_{48}Si_{34}O_{85}(OH)_{62}$) + 20 brucite ($Mg(OH)_2$) = 34 forsterite ($Mg_2SiO_4$) + 51 water ($H_2O$). We assume that antigorite and brucite together represent one solid rock phase with a homogeneous solid density, ρ_s (in kg/m^3), and homogeneous material properties. All model parameters and variables are presented in Table 1. The total density of the porous rock, either consisting of antigorite + brucite or forsterite + water, is

$$\rho_T = \rho_f \phi + \rho_s (1-\phi) \tag{1}$$

with porosity ϕ (volume ratio) and pore-fluid density ρ_f. For simplicity, we assume that the solid phase consists of two components, (1) the non-volatile components, MgO and SiO_2, that remain always in the solid and (2) the volatile component, H_2O, that is liberated during dehydration. We quantify the amount of the non-volatile component as a function of MgO inside the solid with its solid mass (in kg) fraction, X_s, which is $X_s = 0.74$ (68 times the molar mass of MgO / (68 times the molar mass of MgO + 51 times the molar mass of H_2O)) for the solid made of antigorite + brucite in a molar ratio of 1/20. Equivalently, $X_s = 1$ for forsterite. We neglect the SiO_2 in the calculations, because the SiO_2 for the considered reaction cannot vary independently from MgO. The relative density of the solid MgO component in the solid phase is

$$\rho_X = \rho_s X_s \tag{2}$$

2.2. Hydro-chemical model

The conservation of mass (per unit volume) of the solid and the fluid is frequently given by respectively (e.g., McKenzie, 1984)

$$\frac{\partial\left(\rho_s\left(1-\phi\right)\right)}{\partial t} + \nabla\cdot\left[\rho_s\left(1-\phi\right)\mathbf{v}^s\right] = -\Gamma \tag{3}$$

$$\frac{\partial\left(\rho_f\phi\right)}{\partial t} + \nabla\cdot\left[\rho_f\phi\mathbf{v}^f\right] = \Gamma \tag{4}$$

where t is time, $\nabla\cdot$ is the divergence operator, $\mathbf{v}^f$ and $\mathbf{v}^s$ are vectors of the fluid and solid barycentric velocities, respectively, and Γ is a mass transfer rate that quantifies the rate at which mass is transferred from the solid to the fluid phase. Concerning the symbols for vector and tensor quantities, we use indices f and s as superscripts, because vector and tensor components will have additional subscripts indicating the spatial direction, and scalar quantities can be easier distinguished from vector and tensor quantities. In our mathematical model, we do not use the two mass conservation equations (3), for solid mass, and (4), for fluid mass, but instead we use two different mass conservation equations: a conservation equation for total mass and a conservation equation for the total non-volatile component (MgO). The conservation equation of total mass results from the sum of equations (3) and (4) (e.g., Fowler, 1985; Beinlich et al., 2020; Malvoisin et al., 2021; Plümper et al., 2016; Schmalholz et al., 2020):

$$\frac{\partial\rho_T}{\partial t} + \nabla\cdot\left[\rho_f\phi\left(\mathbf{v}^f - \mathbf{v}^s\right)\right] + \nabla\cdot\left(\rho_T\mathbf{v}^s\right) = 0 \tag{5}$$

The relative velocity of the fluid to the solid, $\phi\left(\mathbf{v}^f - \mathbf{v}^s\right)$, in equation (5) is expressed by Darcy's law, here for simplicity in the absence of gravity

$$\phi\left(\mathbf{v}^f - \mathbf{v}^s\right) = -\frac{k\phi^3}{\eta_f}\nabla p_f \tag{6}$$

where ∇ is the gradient operator, k is the permeability coefficient in a porosity-dependent, Kozeny-Carman-type permeability expression, η_f is the fluid viscosity and p_f is the fluid pressure. The conservation equation for the total non-volatile component (MgO) is

$$\frac{\partial}{\partial t}\left[\rho_X\left(1-\phi\right)\right] + \nabla\cdot\left[\rho_X\left(1-\phi\right)\mathbf{v}^s\right] = 0\,. \tag{7}$$

There is no fluid velocity in this conservation equation because we assume that the dissolution of MgO in the fluid is negligible. The main reason why we use mass conservation equations (5) and (7), instead of equations (3) and (4), is that equations (5) and (7) do not include the term for the mass transfer rate, Γ, so that we do not need to specifiy Γ.

We consider a constant temperature and a closed system with constant system composition for the entire model domain, however, H_2O can migrate within our model domain. It has been experimentally demonstrated that dehydration reactions are controlled by fluid pressure (e.g., Llana-Fúnez et al., 2012) and, therefore, we approximate ρ_s, ρ_f and X_s as a function of p_f, which is expressed as (Schmalholz et al., 2020):

$$\begin{aligned} \rho_f &= \rho_f^{EQ}\left(p_f\right) \\ \rho_s &= \rho_s^{EQ}\left(p_f\right)\,, \\ X_s &= X_s^{EQ}\left(p_f\right) \end{aligned} \tag{8}$$

whereby the values of ρ_s^{EQ}, ρ_f^{EQ} and X_s^{EQ} for a range of values of p_f are calculated by equilibrium Gibbs free-energy minimization using the program Perple_X (e.g., Connolly,

1990, 2005, 2009; Fig. 3) with the thermodynamic dataset of Holland and Powell (1998). Newer thermodynamic datasets do not include considerably different values for the Gibbs free energies and the associated densities of the minerals considered here, which is why we still use the Holland and Powell (1998) dataset. We assume that ρ_f always corresponds to ρ_f^{EQ}, as a result of its equation of state (Fig. 3C). Due to the sharp, step-like variation of ρ_s^{EQ} and X_s^{EQ} with varying p_f across the dehydration reaction (Fig. 3C and D) we assume that the reaction is controlled by a kinetic reaction timescale, so that values of ρ_s do not change instantaneously if p_f crosses the value of the reaction pressure at 12.65 kbar (Fig. 3). The kinetic reaction timescales relevant to thermodynamic equilibrium are (e.g., Omlin et al., 2017)

$$\frac{\partial \rho_s}{\partial t} = \frac{\rho_s^{EQ} - \rho_s}{t_{kin}}$$
$$\frac{\partial X_s}{\partial t} = \frac{X_s^{EQ} - X_s}{t_{kin}} \quad (9)$$

where t_{kin} is the characteristic kinetic timescale.

2.3. Mechanical model

The components of the total stress tensor of the two-phase mixture, σ_{ij}, are composed of the total pressure, p, and the components of the total deviatoric stress tensor, τ_{ij}, by the relation $\sigma_{ij} = -p\delta_{ij} + \tau_{ij}$, with δ_{ij} being the Kronecker delta (e.g. Steeb and Renner, 2019). Subscripts i and j are either 1 (representing the horizontal x-direction) or 2 (representing the vertical y-direction). We assume that the contribution of fluid flow to the total deviatoric stress of the mixture is negligible and only consider the solid deformation in the calculation of

the total deviatoric stress (e.g. McKenzie, 1984; Steeb and Renner, 2019). We consider a visco-plastic solid and, hence, the effective shear viscosity, η_s, relates the total deviatoric stress tensor components to the deviatoric strain rate tensor components of the solid, D_{ij}, by the equation $\tau_{ij} = 2\eta_s D_{ij}$, with $D_{ij} = \left(\partial v_i^s / \partial x_j + \partial v_j^s / \partial x_i\right)/2 - \delta_{ij}\left(\partial v_k^s / \partial x_k\right)/3$. Some studies apply the relation $\tau_{ij} = (1-\phi)2\eta_s D_{ij}$ to take into account that the solid deformation only contributes a part to the total deviatoric stress of the mixture (e.g. Keller et al., 2013), while other studies do not consider such porosity factor in the relation between total deviatoric stress of the mixture and partial deviatoric stress of the solid (e.g. Steeb and Renner, 2019). Here, we assume that such porosity effects are implicitely included in a porosity dependent η_s. The porosity dependence of η_s is motivated by studies on partially molten rocks (e.g., Katz et al., 2022; Mei et al., 2002; Schmeling et al., 2012). We consider here two types of porosity dependence of η_s, namely an exponential and a power-law dependence (e.g. Katz et al., 2006; Mei et al., 2002; Schmeling et al. 2012):

$$\tau_{ij} = 2\eta_s D_{ij} = 2\eta_{s0} \exp\left[-a\left(\phi/\phi_0 - 1\right)\right] D_{ij} \tag{10}$$

$$\tau_{ij} = 2\eta_s D_{ij} = 2\eta_{s0} \left(\phi_0/\phi\right)^n D_{ij} \tag{11}$$

where η_{s0} is the reference shear viscosity for a reference porosity, ϕ_0, and a and n are two parameters quantifying the dependence of η_s on ϕ. We further consider a von Mises yield stress, τ_y, to limit the maximal value of the deviatoric stresses. The square root of the second invariant of the deviatoric stress tensor, $\tau_{II} = \sqrt{0.5\left(\tau_{xx}^2 + \tau_{yy}^2\right) + \tau_{xy}^2}$ controls a plastic multiplier, $\vartheta = 1 - \tau_y / \tau_{II}$. If $\vartheta > 0$, then deviatoric stresses are modified using

$$\tau_{ij} = (1-\vartheta)\tau_{ij}\,. \tag{12}$$

One reason why we consider such stress limiter, is to test whether such stress limiter has a significant impact on the numerical simulations of olivine vein formation. A second reason is that this pressure insensitive yield stress can represent any strong nonlinear dependence of the shear viscosity on the deviatoric stress, such as for low-temperature plasticity or exponential creep (e.g. Karato, 2008; Schmalholz and Fletcher, 2011; Tsenn and Carter, 1987). For such exponential creep the stress increases only minor with increasing strain rate, in contrast to the linear viscosity, η_s, for which stresses increase linearly with strain rate, if ϕ is constant.

Furthermore, we consider a poro-visco-elastic volumetric deformation for which the divergence of the solid velocity field is a function of total pressure, p, and fluid pressure, p_f (e.g., Yarushina and Podladchikov, 2015):

$$\nabla \cdot \mathbf{v}^s = -\frac{1}{K_d}\left(\frac{dp}{dt} - \alpha \frac{dp_f}{dt}\right) - \frac{p - p_f}{(1-\phi)\lambda} \tag{13}$$

where λ is the bulk viscosity, K_d is the drained bulk modulus, and $\alpha = 1 - K_d / K_s$ with K_s being the solid bulk modulus. In our model, the magnitude of λ will be linked to the magnitude of η_s (e.g., Katz et al., 2022, and references therein) so that λ is also porosity dependent. We consider elastic bulk deformation in our model to avoid potentially unrealistically large volumetric deformations. If only viscous bulk deformation is considered, then volumetric deformation, represented by the term $\nabla \cdot \mathbf{v}^s$, is essentially unlimited as long as there are differences between p and p_f.

The applied equations for conservation of linear momentum (or force balance equations) without inertial forces and gravity are

$$\nabla \cdot \sigma_{ij} = 0 \tag{14}$$

2.4. Governing system of equations

The equations above can be combined to a system of 11 equations for 11 unknowns, which are p_f, ϕ, ρ_s, ρ_f, X_s, p, v_x^s, v_y^s, τ_{xx}, τ_{yy} and τ_{xy}, assuming that the deviatoric stress tensor is symmetric, $\tau_{xy} = \tau_{yx}$. The deviatoric stress tensor components, τ_{xx}, τ_{yy} and τ_{xy}, are calculated using equations (10). The solid and fluid densities as well as the mass fraction are calculated from the fluid pressure, using the results of thermodynamic calculations represented by equation (8) (thermodynamic relations between ρ_s, ρ_f, X_s and p_f are illustrated in Fig. 3C and D). In our numerical algorithm, described below, we will use equation (5) in combination with (6) to calculate the fluid pressure, p_f, equation (13) to calculate the total pressure, p, equation (7) to calculate the porosity, ϕ, and the two force balance equations (14) to calculate the two solid velocities, v_x^s and v_y^s.

2.5 Numerical algorithm

We discretize the governing system of equations described above using the finite difference method on a regular Cartesian staggered grid. The staggering relies on second-order conservative finite differences (e.g., McKee et al., 2008; Patankar, 2018; Virieux, 1986). The six unknowns τ_{xx}, τ_{yy}, τ_{xy}, ρ_s, ρ_f and X_s can be determined without solving a partial differential equation (PDE) whereas determining the five unknowns p_f, ϕ, p, v_x^s and v_y^s requires the solution of a corresponding PDE. We apply the accelerated pseudo-transient (PT) method to solve the discretized system of governing PDEs in an iterative and matrix-free fashion (e.g., Chorin, 1997; Räss et al., 2022). We use a relaxation, or continuation, approach to handle the various nonlinearities, such as porosity-dependent shear

viscosity and permeablity within the iterative procedure (e.g. Räss et al., 2019a; Schmalholz et al., 2020; Wang et al., 2022). The fundamental features of the applied numerical algorithm and the iterative PT method are described in appendix A1. Furthermore, we present a numerical resultion test and a numerical accuracy test of the applied numerical algorithm in appendix A2.

3. Model configuration, characterstic scales and dimensionless parameters

3.1. Geodynamic scenario

We describe first the geodynamic scenario which represents the motivation for the applied model configuration. We consider an antigorite serpentinite which is sheared during subduction (Fig. 2). For simplicity, the modelled serpentinite is made only of antigorite and brucite. We assume that the serpentinite is mechanically heterogenous. Such heterogeneity is mimicked here by a spatially heterogeneous porosity which causes a heterogeneous viscosity (equations (10) and (11)). The serpentinite includes small regions of higher porosity which generates small regions of lower viscosity. Such viscosity heterogeneities within a deformed, or externally stressed, viscous rock cause pressure variations around the mechanically weaker regions with lower viscosity (e.g. Schmid and Podladchikov, 2003; Moulas et al., 2014; Moulas and Schmalholz, 2020). The pressure variations generate regions with smaller and higher pressure with respect to the ambient background pressure (e.g. Moulas et al., 2014). Recently, Conoiu et al. (2019) showed with laboratory rock deformation experiments and numerical simulations that such pressure variations can cause mineral phase transformations. During subduction and shearing, such pressure variations cause no metamorphic reactions as long as the ambient pressure of the serpentinite is well within the antigorite + brucite stability field and pressure variations do not generate locally pressure magnitudes that are below the

reaction pressure (see potential prograde pressure-temperature path in Fig. 3A). However, if the ambient pressure in the sheared serpentinite is close to the reaction pressure, then pressure variations can generate locally pressures that are below the reaction pressure and trigger dehydration (Fig. 2B). We consider here such scenario where the ambient pressure is close to the reaction pressure in order to investigate dehydration reactions which are triggered by shearing-induced pressure variations. This scenario is motivated by field observations from the Erro Tobbio region (Fig. 1). In this region, the exhumed antigorite serpentinite exhibits locally metamorphic olivine veins which indicate that the serpentinite has locally crossed the brucite-out reaction during subduction (Fig. 2E). However, before exhumation back to the surface, the antigorite serpentinite has never crossed the antigorite-out reaction, because this reaction would have generated peridotite (Fig. 2E). Therefore, the olivine veins in the exhumed antigorite serpentinites, exposed in the Erro Tobbio region, have likely formed in a relatively narrow ambient pressure and temperature range (Fig. 2E).

3.2. Model configuration

We assume that p_f and p are initially identical and correspond to the ambient pressure, p_a. The ambient porosity, ϕ_a, is 2%, except in an elliptical region in the model center where the porosity exhibits a Gaussian distribution (Fig. 4). The initial Gaussian distribution of the porosity is: $\phi_0 = \phi_a + A_\phi \exp\left[-\left(x/r\right)^2 - \left(y/2r\right)^2\right]$. A_ϕ is the amplitude of the initial porosity perturbation and the distance r controls the width, or variance, of the porosity distribution (Fig. 4). We apply here an elliptical form of the Gaussian distribution with an axis ratio of 2 and with the long axis either parallel to the vertical y-direction or at 45° to the vertical direction (see the two blue dashed lines in Fig. 4). The origin of the coordinate system is at the center of the elliptical region with positive coordinates indicating towards the

356 right side and upwards (Fig. 4). We will also present two simulations with a random initial
357 perturbation of the porosity. The shear and bulk viscosities are smaller in the central region of
358 the model due to the higher porosity. We assume a constant temperature of 500 °C for which
359 the thermodynamic reaction pressure in our model is at 12.65 kbar (Fig. 3). The exact
360 temperature value is not essential for our study, because the variation of the solid and fluid
361 densities with varying fluid pressure is similar for temperatures between 450 and 550 °C (Fig.
362 3A and B). We apply far-field simple shear for the boundary velocities (Fig. 4) so that the
363 divergence, or volume change, of the entire model domain is zero. Shearing is parallel to the
364 horizontal x-direction and the orientations of the maximal and minimal principal stresses, σ_1
365 and σ_3 respectively, associated with the far-field shearing are oriented at 45 ° to the shearing
366 direction (Fig. 4). Boundary conditions for ϕ and p_f are of Dirichlet type, with boundary
367 values fixed to the initial ambient values.

368

369 *3.3. Compaction length, characteristic time and dimensionless parameters*

370 In our simulations, we always consider the same dehydration reaction with its
371 associated fluid pressure versus density relations (Fig. 3C). Therefore, the characteristic
372 pressure for our simulations is fixed and corresponds to the reaction pressure of 12.65 kbar.
373 Hence, we present the results for pressures and densities in dimensional form. However, the
374 magnitudes of other quantities such as ambient permeability, shear viscosities, far-field
375 shearing rate or size of the initial porosity perturbation are arbitrary in our model, as long as
376 they are within a range that is realistic for natural conditions. Therefore, we will describe the
377 performed simulations with a set of dimensionless numbers and not with a table including
378 specific dimensional magnitudes for each model parameter. Furthermore, we will present the

379 spatial and temporal evolution of the simulations with dimensionless coordinates and a
380 dimensionless time, respectively, to emphasize their general applicability.

381 To describe the hydro-mechanical features of the model configuration, we will use a
382 characteristic length scale, δ, and a characteristic time scale, t_C. In a viscously deformable
383 porous medium, the compaction of the poro-viscous medium and associated spatial variations
384 in solid and fluid velocities occur over a characteristic length scale which is termed the
385 compaction length (e.g. McKenzie, 1984). We use this compaction length as δ. Similarly, the
386 compaction and associated porous fluid flow occurs over a characteristic time scale, which we
387 use as t_C. The δ and t_C are given by:

388
$$\delta = \sqrt{\frac{k\phi^3}{\eta_f}\left[\lambda(\phi) + \frac{4}{3}\eta_s(\phi)\right]} \qquad (15)$$
$$t_C = r^2\eta_f / \left(k\phi^3 K_s\right)$$

389 In our model with porosity dependent effective permeability as well as porosity
390 dependent shear and bulk viscosities, both δ and t_C depend on ϕ. We consider two different
391 relations between η_s and ϕ (equations (10) and (11)) which control the relation between δ
392 and ϕ (Fig. 5). We make δ dimensionless by dividing it by r and discuss in the following
393 the relation between δ / r and ϕ applied in the simulations. For simplicity, the porosity
394 exponent in the effective permeabilty is always 3 in the simulations (equation (6)). To
395 quantify and label the applied $\delta / r - \phi$ relations we introduce the dimensionless parameter Ω_1
396 that represents the value of δ / r for the ambient porosity ϕ_a, that is:

397
$$\Omega_1 = \left.\frac{\delta}{r}\right|_{\phi=\phi_a} . \qquad (16)$$

For simulations with an exponential dependence of η_s on ϕ (equation (10)) we employ 6 different values of Ω_1, ranging approximately between 0.008 and 0.2 (legend in Fig. 5A). We use mostly $a = 1/2.5$, but also present two simulations with $a = 1/1.65$ (equation (10); Fig. 5A and C). With increasing ϕ, values of δ / r first increase and then decrease (Fig. 5A). The maximum value of δ / r is approximately 25 times larger than the minimum value of δ / r for each displayed $\delta / r - \phi$ curve (Fig. 5A). The variation of η_s, normalized by the viscosity for the ambient porosity, η_{sa}, with increasing ϕ is displayed in figure 5C. For comparison, we illustrate representative values for experimentally determined shear viscosities for partially molten rock as function of porosity (experimental data is taken from the compilation of Katz et al., 2022; see figure caption for all references). The experimental data shows that the effective shear viscosity of a porous medium can vary 3 to 4 orders of magnitude when the porosity varies between approximately 2 and 25%.

For η_s with power-law dependence on ϕ (equation (11)) we use three values for the power-law exponent, namely n = 2, 3 and 4, (Fig. 5C) in order to obtain values of δ / r that are increasing, constant or decreasing, respectively, with increasing ϕ (Fig. 5B). For all three δ / r versus ϕ relations the values of $\Omega_1 \approx 0.035$ (Fig. 5B).

For all applied $\delta / r - \phi$ relations, the values of Ω_1 are approximately between 0.01 and 0.1 which means that r is approximately 10 to 100 times larger than δ for the poro-viscous medium with ambient porosity. Such values for Ω_1 are suitable, because deformation associated with compaction occurs over a distance which is several times larger than δ (e.g. McKenzie, 1984). If $\Omega_1 \ll 0.01$, then compaction occurs over a distance much smaller than the porosity distribution, the compaction is essentially spatially unrelated to the porosity perturbation and it is unfeasible to numerically resolve both the porosity perturbation and the

compaction which occurs on a much smaller length scale. If, on the other hand, $\Omega_2 \gg 0.1$, then compaction occurs on spatial scales larger or equal to the size of the porosity perturbation and it is difficult to generate significant fluid pressure perturbations within small areas around the weak region with increased porosity. Similar values for Ω_1, as applied here, are also typically used in simulations of porosity waves (e.g. Simpson and Spiegelman, 2011; Dohmen and Schmeling, 2021). Hence, we chose the applied values of Ω_1 because they are suitable to model poro-viscous deformation and associated pressure perturbations caused by the initial porosity perturbations.

To describe the presented numerical simulations, we use several more dimensionless ratios:

$$\begin{aligned} \Omega_2 &= \left.\frac{\bar{D}_{xy}\eta_s}{p_a}\right|_{\phi=\phi_a} \\ \Omega_3 &= \frac{w}{r} \\ \Omega_4 &= \left.\frac{\lambda}{\eta_s}\right|_{\phi=\phi_a} \\ \Omega_5 &= \left.\frac{t_{kin}}{t_C}\right|_{\phi=\phi_a} \end{aligned} \tag{17}$$

where w is the model width and $\bar{D}_{xy}$ is the applied far-field simple shear rate (Fig. 4). All dimensionless ratios that are dependent on the porosity are specifed for the applied ambient porosity, ϕ_a = 2%. In most of the presented simulations with an initial Gaussian porosity distribution, we apply $\Omega_2 = 0.11$, which means that the shear stress resulting from the applied far-field simple shear is approximately one order of magnitude smaller than the ambient pressure. We further apply $\Omega_3 = 40$ to have a model domain significantly larger than the applied porosity perturbation, $\Omega_4 = 2$, which is supported by theoretical models and

experiments (e.g. Katz et al., 2022), and $\Omega_5 = 0.0025$, so that the kinetic time scale is significantly faster than the hydraulic diffusion time scale. If a different dimensionless parameter was applied, it will be mentioned in the description of the results. The applied values of Ω_1 will be given when the simulations are discussed below.

Furthermore, we will discuss the magnitudes of δ and t_C as well as the applied dimensional ratios with respect to realistic quantities below. In the figures, physical units are displayed in square braces, for example $\left[kg / m^3\right]$. The horizontal, x, and vertical, y, coordinates are normalized by r and the simulation time as well as all displayed rates, e.g. $\nabla \cdot \mathbf{v}^s$, will be normalized by t_C, whereby t_C is calculated for the ambient porosity, ϕ_a.

4. Results

4.1 Overview

The result section is structured in two general parts. In the first part, we investigate the impact of ambient pressure, compaction length, yield stress and geometry of the initial porosity distribution on the formation of dehydration veins. In the second part, we focus on one simulation to quantify the mechanisms which cause the production and evolution of porosity during deformation and dehydration.

4.2. Impact of ambient pressure on dehydration vein formation

With the first three simulations we test the impact of the ambient pressure, p_a, on the formation of dehydration veins (Fig. 6). We apply $\Omega_1 = 0.033$ and an exponential relation between η_s (a=1/2.5) and ϕ (Fig. 5A and C). The amplitude of the initial ϕ perturbation is

461 $A_\phi = 12$ and the maximal ϕ in the model center is 24%. Hence, the minimum initial η_s in the
462 model center is approximately 100 times smaller than η_{sa} (Fig. 5C). The long axis of the
463 initial Gaussian ϕ distribution is oriented 45° with respect to the vertical y-direction so that
464 the long axis is parallel to the maximal principal stress for the applied far-field simple shear (
465 σ_1 in Fig. 4). We apply p_a of 14.5 (Fig. 6A to D), 13.5 (Fig. 6E to H) and 12.75 kbar (Fig. 6I
466 to L). If in the simulations p_f decreases below 12.7 kbar, then an increase of ρ_s begins due
467 to the dehydration reaction in our discretized model (Fig. 3C). For p_a of 14.5 kbar, p_f does
468 not decrease below 12.7 kbar in the model domain (Fig. 6A to D). During significant simple
469 shearing, the ϕ perturbation is sheared and rotated (see red porosity contours in Fig. 6A to D)
470 and p_f perturbations are always present around the region with higher ϕ (Fig. 6A to D). No
471 vein-like structure with increased ϕ, oriented parallel to σ_1, develops in the model when no
472 dehydration reaction takes place. For p_a of 13.5 kbar, p_f decreases locally below 12.7 kbar
473 after some shearing (black contour lines in Fig. 6F to H; see contour labels in panel Fig. 6I)
474 and two separate, elongated regions with decreased p_f and increased ϕ develop (Fig. 6F to
475 H). ϕ in these regions is increased with respect to the ϕ_a (change of red contour line in Fig.
476 6E to H). For p_a of 12.75 kbar, a single elongated region with p_f < 12.7 kbar develops in
477 which ϕ is increased with respect to ϕ_a (Fig. 6I to L). In summary, the results show that (i) if
478 no dehydration reaction takes place, no elongated, or vein-like, region with increased ϕ
479 develops, (ii) for the applied model configuration, p_a of 13.5 kbar is sufficiently close to the
480 reaction pressure of 12.65 kbar so that shear-driven perturbations in p_f can trigger
481 dehydration and (iii) dehydration during shearing generates elongated, vein-like regions of
482 increased ϕ which are oriented parallel to σ_1 (Fig. 6).

483

484 *4.4. Impact of porosity dependence of compaction length*

485 We apply p_a of 12.75 kbar, the same configuration as for the simulation displayed in
486 figure 6I to L, and use Ω_1 = 0.0082, 0.033 and 0.082 for an exponential dependence of η_s on
487 ϕ (Fig. 5A). For Ω_1 = 0.0082, two elongated, separate regions with ρ_s > 3000 kg/m^3
488 developed during shearing, indicating the reaction from serpentinite to olivine (Fig. 7A to D).
489 This simulation was run until it failed to converge, which was caused by extremely sharp
490 gradients in material properties around the two vein tips. For Ω_1 = 0.033, one continuous
491 elongated region with ρ_s > 3000 kg/m^3 develops (Fig. 7E to H), showing the formation of an
492 olivine vein. For Ω_1 = 0.082, also one continuous elongated region with increased values of
493 ρ_s develops, but maximal values of ρ_s are slightly below 3000 kg/m^3 (Fig. 7I to L). The time
494 evolution of maximal values of ρ_s, minimal values of p_f and relative increase of ϕ will be
495 discussed further below.

496 We perform three additional simulations for the same configuration as for the
497 simulations presented in figure 7, but for a power-law dependence of η_s on ϕ (see Fig. 5B)
498 with three different values of the power-law exponent, n. For n = 4 and Ω_1 = 0.033, values
499 of δ / r monotoneously decrease with increasing ϕ (Fg. 5B). In this simulation, an elongated
500 region with increased ρ_s and decreased p_f develops (Fig. 8A to D). However, maximal
501 values of ρ_s < 2850 kg/m^3. For n = 3 and Ω_1 = 0.036, values of δ / r are constant with
502 increasing ϕ, and also an elongated region with increased ρ_s and decreased p_f develops
503 (Fig. 8E to H). Maximal values of ρ_s are just slightly larger than 2900 kg/m^3. For n = 2 and
504 Ω_1 = 0.033, values of δ / r monotoneously increase with increasing ϕ, and two separate,

505 elongated regions with increased ρ_s and decreased p_f develop (Fig. 8I to L). For this
506 simulation, maximal values of ρ_s > 3000 kg/m^3.

507 The temporal evolution of the dehydration and olivine formation depends on the
508 applied $\delta / r - \phi$ relations and the value of Ω_1 (Figs. 7 and 8). We performed a total of
509 seven simulations for an exponential dependence of η_s on ϕ and with different values of Ω_1
510 (Fig. 9) to study the temporal evolution of maximal values of ρ_s (Fig. 9A), minimal values of
511 p_f (Fig. 9B) and the maximal relative increase of ϕ (Fig. 9C). The presented maximal or
512 minimal values correspond to the maximal or minimal value in the entire model domain at
513 one particular numerical time step. Maximal values of ρ_s start to increase faster for smaller
514 values of Ω_1 (Fig. 9A) and corresponding minimal values of p_f are smaller for smaller Ω_1
515 (Fig. 9B). Smaller Ω_1 favor the development of larger perturbations of p_f, however, these
516 perturbations for smaller Ω_1 also decay faster compared to simulations with larger Ω_1 (Fig.
517 9B). For larger Ω_1, the perturbations of p_f become smaller and, hence, maximal ρ_s reach
518 smaller values (Fig. 9A). For the largest Ω_1 of 0.16, maximal ρ_s < 2875 kg/m^3, which is the
519 average density between the density of antigorite+brucite and forsterite in our model (Fig.
520 3C). If we run the same simulation with Ω_1 = 0.16 again, but now with p_a of 12.71 kbar,
521 then maximal ρ_s > 3000 kg/m^3, which confirms that the closer p_a is to the reaction pressure,
522 the more intense is the dehydration and progress of the reaction (compare with Fig. 6). To
523 investigate the relative evolution of ϕ, we store at each numerical grid point the ratio of the
524 initial to the current value of ϕ. For each numerical time step, we determine the maximal
525 value of this porosity ratio and plot its evolution with progressive simulation time (Fig. 9C).
526 In all simulations the maximal porosity ratio is continuously increasing, showing that
527 dehydration is continuously ongoing. At the end of the simulations, maximal values of the

porosity ratio are between 10 and 25, showing that ϕ increases more than an order of magnitude during the simulations.

For the three simulations with a power-law dependence of η_s on ϕ, maximal values of ρ_s start to increase faster for larger values of n, but maximal ρ_s during the simulations is smaller for larger n (Fig. 9D). Only for n = 2 the simulation generates ρ_s > 3000 kg/m^3. Minimal values of p_f are smallest for n = 4 and similar for n = 3 and 2 (Fig. 9E). The larger the n, the faster the minimum p_f develops during the simulations (Fig. 9D). In simulations with n = 4 and 3, the increase of the maximal porosity ratio is considerably slowing down with time and this ratio is even decreasing towards the end of the simulation for n = 4 (Fig. 9F). This decrease of the porosity ratio with shearing indicates that the progress of the dehydration reaction slows down in the simulation, in agreement with the decrease of maximal ρ_s (Fig. 9D).

In summary, the simulations (Figs. 7, 8 and 9) described above confirm that the relation between δ / r and ϕ has a strong impact on the development of the dehydrating region, the progress of olivine formation and the geometry of olivine veins. For our model configuration, the most suitable conditions for the formation of a single olivine vein are for an exponential dependence of η_s on ϕ and for values of Ω_1 approximately between 0.016 and 0.1.

4.5. Impact of plasticity and orientation of porosity perturbation

In regions with constant ϕ, η_s is also constant and the modelled poro-viscous medium flows like a linear viscous fluid. To test the impact of significant nonlinear flow, we apply a

pressure-insensitive yield stress, τ_y, corresponding to a von Mises type yield criterion (equation (12)). We perform the simulation with Ω_1 = 0.033, for which results are shown in figure 6I to L and 7E to H, with τ_y = 100 MPa, that is approximately a factor of 0.08 of the reaction pressure magnitude (Fig. 10A to D). Without application of τ_y, the maximal shear stresses in this simulation correspond to approximately 150 MPa. Overall, the simulation with τ_y = 100 MPa is similar to simulations without the application of a yield stress, τ_y. The application of a yield stress, τ_y, and the associated nonlinear viscous flow, or creep, does, hence, not significantly impact the formation of olivin veins.

A similar result is obtained for two simulations, with and without τ_y, for which the initial orientation of the long axis of the elliptical Gaussian porosity distribution was vertical (Fig. 8E to L). For these two smulations with an exponential relation between η_s and ϕ, a = 1/1.65 (see Fig. 5A and C), Ω_1 = 0.016, Ω_2 = 0.16 and $A_\phi = 12$ so that the minimum initial η_s in the model center is again approximately 100 times smaller than η_{sa}, similar to the simulations with a = 1/2.5. For this initial geometrical ϕ perturbation, the olivine veins with $\rho_s \approx$ 3000 kg/m^3 are also parallel to σ_1, but the veins are curved in their center, resulting from the initial ϕ perturbation. Compared to the simulation without τ_y (Fig. 10E to H), the simulation with τ_y = 125 MPa is shorter and slightly thicker at comparable simulation stages (Fig. 10I to L).

We finally apply initially a random ϕ perturbation and τ_y = 100 MPa to test whether olivine veins associated with dehydration occur for more realistic ϕ perturbation and nonlinear creep (Fig. 11). We generated the initial porosity distribution with the random field generator presented in Räss et al. (2019). All other parameters are the same as for the

simulation presented in figures 6I to L and 7E to H. With progressive shearing, several veins with ρ_s >3000 kg/m^3 (Fig. 11A to D) and ϕ >0.5 (Fig. 11E to H) develop. The long axes of these veins are oriented parallel to σ_1 and have an orientation similar to an en échelon geometry. The values of τ_{II} are smallest inside the veins due to the low, porosity-dependent η_s. Due to this porosity dependence of η_s, the magnitudes of τ_{II} are very heterogeneous throughout the model. The area-averaged value of τ_{II} in the model for each time step is a proxy for the area-averaged shear strength and effective viscosity of the model domain, if a constant far-field shearing rate is applied, as done here. The increase of the areas with smaller τ_{II} with progressive shearing (Fig. 11) indicates, hence, a decrease of the average viscosity and, consequently, a weakening of the rock unit represented by the model domain (e.g. Schmalholz et al., 2020).

In summary, the simulations with different initial ϕ perturbations and nonlinear creep, modelled here in a simple way by the application of τ_y show that (i) the geometry of the initial ϕ perturbation and the type of flow law for the solid deformation do not strongly impact the dehydration and olivine vein formation and (ii) olivine veins are formed in our model also for more realistic model configurations considering random initial ϕ perturbations and nonlinear flow laws for the solid.

4.6. Mechanisms of porosity production

In the presented simulations, the modelled dehydration reaction, the porous fluid flow and the solid deformation all can affect the production and evolution of ϕ. However, which mechanisms exactly produce ϕ and their relative importance is unclear. One reason is that in our coupled HMC model, most quantities, such as solid and fluid densities, porosity, fluid

595 pressure, shear and bulk viscosities and solid and fluid velocities, vary in space and time. We,
596 therefore, first investigate the evolution of several quantities for a particular simulation, which
597 is the one displayed in figure 6I to L and 7E to H. Due to the point symmetry of the vein with
598 respect to the coordinate origin, we only show the upper, left half of the vein (Fig. 12). The
599 divergence of the solid velocity, $\nabla \cdot \mathbf{v}^s = \partial v_x^s / \partial x + \partial v_y^s / \partial y$, indicates a volumetric change
600 associated with dehydration vein formation (Fig. 12). A positive value of $\nabla \cdot \mathbf{v}^s$ indicates
601 volume increase, or dilation (Bordeaux colors in Fig. 12). The solid velocities indicate mainly
602 the applied far-field simple shear deformation (black arrows in Fig. 12), with some deviations
603 around the dehydrating region. The fluid velocities (blue arrows in Fig. 12) are completely
604 different compared to the solid velocities. For the first time step, fluid flow only occurs in the
605 central region where the porosity, and hence permeability, is high (Fig. 12A). During
606 dehydration vein formation, fluid flow mainly is localized along the boundaries of the veins
607 which are characterized by higher values of $\nabla \cdot \mathbf{v}^s$ (Fig. 12B to D). The fluid velocities
608 indicate fluid flow from the boundary of the dehydrating region towards the centre of the vein
609 (Fig. 12B to D). For the first time step, the ϕ distribution indicates the initial, oblique
610 Gaussian geometry (blue contour in Fig. 12). With progressive deformation and vein
611 formation, the region with higher ϕ grows in direction parallel to the dehydration vein. At the
612 beginning of shearing, there is a small region with p_f <12.7 kbar (red contours in Fig. 12A)
613 and this region is growing in a direction parallel to the vein (Fig. 7A). The region with ρ_s >
614 2700 kg/m^3 (dashed grey contours in Fig. 12) also increases in direction parallel to the vein.
615 In the early stages of shearing, nowhere in the model ρ_s > 2700 kg/m^3, since there are no
616 contours for ρ_s = 2700 kg/m^3 (Fig. 12A).

617 To quantify the relative contribution of the mechanisms controlling the temporal
618 variation of ϕ, we post-process our numerical results (i.e. calculate values from saved

numerical results). We quantify the mass transfer rate, Γ, associated with the dehydration reaction, which can be expressed by (using equation (3)):

$$\Gamma = -\frac{d\left(\rho_s\left(1-\phi\right)\right)}{dt} - \rho_s\left(1-\phi\right)\nabla\cdot\mathbf{v}^s . \tag{18}$$

Note that in equation (18) the material time derivative (d/dt, including the advection term, $\mathbf{v}^s\nabla\cdot\left[\rho_s\left(1-\phi\right)\right]$) is used and, hence, the divergence term is different compared to equation (3). Therefore, equation (18) represents an approximation of Γ since the advective term is not taken into account, here for simplicity of the post-processing. Equation (18) can be rearranged to provide an expression for the temporal variation of the porosity:

$$\frac{1}{\left(1-\phi\right)}\frac{d\phi}{dt} = \nabla\cdot\mathbf{v}^s + \frac{1}{\rho_s}\frac{d\rho_s}{dt} + \frac{\Gamma}{\rho_s\left(1-\phi\right)} \tag{19}$$

Equation (19) shows that the temporal variation of the porosity is controlled by three mechanisms: (1) volumetric deformation of the solid (i.e. divergence of solid velocity field; first term on right-hand side of equation (19)), (2) temporal variation of solid density (second term) and (3) mass transfer of H_2O from the solid to the fluid phase associated with the dehydration reaction (third term). We display the spatial distribution of the four terms in equation (19) for the simulation displayed in figure 12 at a dimensionless time of 0.008 (Fig. 13). All four terms represent rates, have units of 1/s, such as the unit of solid volumetric deformation rate $\nabla\cdot\mathbf{v}^s$, and are normalized by multiplying with t_C for ϕ_a. The rate of ϕ, quantified by the term on the left-hand side of equation (19), is positive and largest in the region of increased ϕ, indicating an increase of ϕ with time (Fig. 8A). The sum of the three terms on the right-hand side of equation (19) provides essentially the same result as the term on the left-hand side of equation (19), indicating the accuracy of equation (19) (Fig. 13A and B). The magnitudes of the relative contributions of solid volumetric deformation (Fig. 13C),

641 solid density variation (Fig. 13D) and mass transfer (Fig. 13E) to the temporal variation of
642 porosity are similar, because the spatial distribution and magnitude of these three terms are
643 similar (Fig. 13 D to E). Therefore, solid volumetric deformation, solid density variation and
644 reactive mass transfer equally contribute to the porosity variation and, hence, to the evolution
645 of the dehydration veins.

646 To investigate the temporal variation of the relative importance of solid volumetric
647 deformation rate, solid density rate and mass transfer rate on the rate of ϕ, we record the
648 maximum value of each rate for each numerical time step and plot these maximum rates
649 versus the dimensionless model time (Fig. 14). All rates first increase and then decrease.
650 During the initial stages of vein formation, the mass transfer rate is fastest and the volumetric
651 deformation rate is slowest. Subsequently, there is a time interval where the mass transfer rate
652 is still fastest, but the solid density rate is slowest. Afterwards, until the end of the simulation,
653 the solid volumetric deformation rate is fastest and the solid density rate is slowest. In
654 summary, the results indicate that all three rates always contribute to ϕ production, but with
655 varying relative importance as function of time.

656

657 **5. Discussion**

658 *5.1. Shear-driven dehydration and olivine vein formation*

659 Field observations have led previous authors to hypothesize that en échelon
660 metamorphic olivine veins have been caused by shear deformation, but this hypothesis has not
661 been tested with a HMC model. Our simulations show that it is hydrologically, mechanically
662 and chemically feasible to form olivine veins by dehydration reactions which are triggered
663 during ductile shearing of serpentinite. A thermodynamic reaction, such as the dehydration
664 reaction considered here, is typically controlled by a narrow zone in pressure-temperature

665 space (e.g. Fig. 2E and 3). In isothermal models, such as the one presented here, the reaction
666 occurs, therefore, across a narrow pressure range (Fig. 3C). In our model, the fluid pressure,
667 p_f, controls the reaction which is supported by theoretical and experimental studies (e.g.
668 Dahlen, 1992; Llana-Fúnez et al., 2012). The p_f is initially homogeneous and everywhere in
669 the model domain within the serpentinite stability field, and represents the ambient fluid
670 pressure, p_a. Only if p_a is close to the reaction pressure and if the shear-driven p_f
671 perturbations are significant, then p_f can decrease locally below the reaction pressure during
672 shearing and trigger the dehydration reaction (Fig. 6). For our model configuration, p_a of
673 13.5 kbar was close enough to trigger dehydration for a reaction pressure of 12.65 kbar
674 (pressure difference of 0.85 kbar; Fig. 6). Assuming an average density of the overlying rock
675 of 3000 kg/m^3 for this pressure difference, the dehydration can be triggered in our model
676 when the rocks are within a vertical distance of approximately 2.5 to 3 km to the depth at
677 which the reaction would occur with respect to a lithostatic pressure.

678 Our model for shear-driven dehydration is different to published models of similar
679 dehydration reactions, because in these published models an initially heterogeneous
680 distribution of p_f is applied such that initial values of p_f involve already different values
681 that correspond to the stability fields on both sides of the reaction (e.g. Huber et al., 2022;
682 Malvoisin et al., 2015; Schmalholz et al., 2020). Therefore, the initial condition in these
683 models guarantees that the initial p_f will trigger the dehydration reaction. In contrast, in our
684 model also the evolution of a heterogeneous p_f distribution is simulated (Fig. 6). Whether
685 this evolving p_f distribution can trigger dehydration and eventually generate an olivine vein,
686 depends on the applied value of p_a and model parameters, such as the applied $\delta / r - \phi$
687 relation (Figs. 6, 7 and 8). Only if the fluid pressure decreases locally below the reaction

688 pressure, an olivine vein can form. Consequently, our model predicts mechanical deformation
689 as a potential mechanism by which dehydration veins can be formed locally. An alternative
690 possibility for triggering locally dehydration, is an initially heterogeneous chemical
691 composition of the serpentinite in which some regions, having for example brucite, dehydrate
692 while other regions, for example exclusively composed of antigorite, do not dehydrate (e.g.
693 Plümper et al., 2017). Such chemical mechanism does not require any solid deformation.
694 However, for such mechanism the orientation of the olivine veins is entirely controlled by the
695 initial chemical composition. The specific en échelon geometry of olivine veins is most likely
696 not caused by initial chemical heterogeneity in a non-deforming rock, especially since these
697 veins are formed in a strongly sheared antigorite serpentinite.

698 Field data show that in the Erro Tobbio region the olivine in the studied veins is
699 indeed metamorphic olivine, which is also supported by geochemical studies (e.g., Peters et
700 al., 2020). Furthermore, in all presented simulations, the formation of dehydration veins is not
701 a run-away process, but a self-limiting process (Fig. 9). In the low-pressure regions, where
702 dehydration takes place, p_f first decreases and then increases again which slows down the
703 dehydration reaction (Fig. 9B and E). Hence, the simulation with initial random porosity
704 perturbation shows the formation of several veins with similar length, which stop growing
705 after some amount of shear (Fig. 11). The simulation does not show the formation of a single
706 vein which grows across the entire model domain (Fig. 11). The formation of many veins of
707 similar size and orientation, and the absence of few, large veins is in agreement with natural
708 observations (Fig. 1). Therefore, based on published geochemical studies, structural
709 observations and our modelling results, we propose that the formation of observed olivine
710 veins was the result of a coupled deformation-reaction process that accelerated mineral
711 dehydration along particular orientations, controlled by the local stress field in the sheared

712 serpentinite. Similar veins made of metamorphic olivine have been described from subducted
713 serpentinite, such as in the Zermatt-Saas unit in the Central Alps (e.g., Kempf et al., 2020).

714

715 *5.2. Rescaling to dimensional parameters*

716 We consider here one specific dehydration reaction which controls the relation
717 between fluid pressure and densities (Fig. 3). We did, hence, not rearrange the governing
718 system of equations into a dimensionless system of equations for which model parameters are
719 commonly clustered in dimensionless numbers, such as Damköhler or Péclet numbers (e.g.
720 Jones and Katz, 2018). However, most model parameters, such as shear viscosities,
721 permeabilities or far-field shearing rate, are arbitrary in our model. Therefore, we did not
722 perform the simulations for a specific set of parameter magnitudes, but we used dimensionless
723 ratios to quantify the relations between model parameters (equations (16) and (17)). We
724 assume now particular values for the model parameters and discuss the applicability and
725 consequences of the chosen dimensionless ratios for the natural situation. We applied Ω_4 =
726 λ / η_s = 2, which is based on theoretical and experimental results (see Katz et al., 2022 and
727 references therein), and we assume η_s = 10^{17} Pa s. Despite the importance of antigorite
728 serpentinite, its rheology at lithospheric-scale pressure and temperature conditions remains
729 not well constrained (e.g. David et al., 2018; Hirauchi et al., 2020, and references therein).
730 However, for the ambient pressure and temperature conditions considered here, viscosities of
731 antigorite serpentinite of approximately 10^{17} Pa s seem feasible based on experimental studies
732 (e.g., Chernak and Hirth, 2010; Hilairet et al., 2007). We further assume η_f = 10^{-3} Pa s, ϕ_a =
733 0.02 and r = 10 cm. Applied values of Ω_1 range between 0.0082 and 0.16 (Fig. 9). For the
734 values assumed above, values of Ω_1 between 0.0082 and 0.16 require values for the product

735 $k\phi_a^3$, which represents the ambient permeability, approximately between 10^{-27} and 10^{-24} m^2,
736 respectively. Note, that we could have used also the permeability formulation
737 $k\phi^3 = k\phi_a^3 \left(\phi / \phi_a\right)^3 = k_0 \left(\phi / \phi_a\right)^3$ and then k_0 would represent the ambient permeability. Such
738 values for $k\phi_a^3$ indicate that the serpentinite should be essentially impermeable in the regions
739 where the olivine veins form. Experimental studies suggest that serpentinite permeability
740 decreases exponentially with depth and is in the order of 10^{-23} and 10^{-21} m^2 at a depth of 7 km
741 below seafloor (e.g. Hatakeyama et al., 2017). Permeabilities at much greater depth and
742 ambient pressure, as the 12.75 kbar ambient pressure considered here, could hence be smaller
743 than 10^{-23} m^2. The extrapolation of Hatakeyama et al. (2017) (their equation 1), for their
744 sepertinite termed Sengen-03, suggests a permeability of 10^{-26} m^2 already for a confining
745 pressure of approximately 6 kbar. Therefore, permeabilites between 10^{-24} and 10^{-26} m^2, or in
746 other words an effectively impermeable antigorite serpentinite as required in our models, is
747 not unrealistic for natural antigorite serpentinite under a confining pressure of approximately
748 12.75 kbar and the assumed temperature of 500 °C. Furthermore, η_s could have potentially
749 been smaller than 10^{17} Pa s during significant shearing, for example due to a strongly
750 nonlinear deformation behavior as mimicked here with a pressure-insensitive yield stress, so
751 that required values for $k\phi_a^3$ could also have been larger than 10^{-24} m^2, keeping values of Ω_1
752 the same.

753 For Ω_2 we applied a value of 0.11 which requires a value of $\bar{D}_{xy}$ of approximately 10^{-9}
754 s^{-1}. For a typical subduction velocity of 3 cm/yr, a shear zone must be 1 m thick so that a
755 relative shear velocity across the shear zone generates a shearing rate of 10^{-9} s^{-1}. Such strain
756 rate and η_s = 10^{17} Pa s generates a shear stress in the order of 100 MPa and we also applied a
757 yield stress in some simulations to limit shear stresses to 100 MPa (Figs. 10A to D and 11).
758 Such stress magnitudes agree with recent estimates of England and Smye (2023), who suggest

shear stresses of up to 100 MPa at subduction interfaces. Fast shearing rates of 10^{-9} s^{-1} are presumably more likely achieved during aseismic slow slip events, whereby shearing velocities are larger than a few centimeters per year. For example, typical slip velocities associated with long term slow slip events are between 35 and 70 cm/yr (1 to 2 mm/day; see review of Behr and Bürgmann, 2021, and references therein) and for such faster slip velocities strain rates of 10^{-9} s^{-1} are achievable in shear zones with thicknesses of up to approximately 20 m.

For the parameters assumed above, for $k\phi_a^3 = 10^{-25}$ m^2 and for a typical solid bulk modulus $K_s = 10^{11}$ Pa, the characterstic time (t_C, equation (15)) for ϕ_a is approximately 30 years. A typical dimensionless duration, normalized by t_C, of a simulation is in the order of 0.03 (Fig. 9), which corresponds to a natural duration of approximately 1 year. If the value of $k\phi_a^3 = 10^{-24}$ m^2, then the duration is in the order of one month. The applied value of $\Omega_5 =$ 0.0025 means that the characteristic kinetic time, or duration, should be at least one order of magnitude faster than the duration of the vein formation.

In summary, the rescaled dimensional quantities suggest that if our model is approximating the natural process of shear-driven olivine vein formation, then the serpentinite should have been effectively impermeable and the shear deformation should have been fast, potentially related to aseismic slow slip events.

5.3. Shear-driven high-porosity fluid bands without dehydration

In our simulation with $p_a = 14.5$ kbar, in which no dehydration reaction ocurrs (Fig. 6A to D), one might expect the formation of elongated regions with increased ϕ due to a process similar to the process that forms localized melt bands during simple shearing of

782 partially molten rock (e.g. Holtzman et al., 2003; Katz et al., 2006; Spiegelman, 2003;
783 Stevenson, 1989). However, in the simulation with p_a = 14.5 kbar no such bands with high ϕ
784 formed (Fig. 6A to D). One reason might be that the characteristic time scale of fluid flow, t_C,
785 is too short with respect to the duration of shearing, because the final dimensionless time of
786 the simulation with p_a = 14.5 kbar is 0.176 (Fig. 6D). This means that t_C is approximately a
787 factor of 5 larger than the duration of the simulation. To test the impact of t_C, we performed
788 the same simulation with p_a = 14.5 kbar, but now for a value of $k\phi_a^3$ that is 100 times larger,
789 so that t_C is 100 times shorter and the corresponding Ω_1 is 10 times larger, namely Ω_1 = 0.33
790 (Fig. 15A to D). For such values of t_C and Ω_1, the simulation shows indeed the formation of
791 an elongated region with high ϕ which is oriented parallel to the orientation of σ_1 (Fig. 15A
792 to D). We also performed the simulation with an initially random perturbation (Fig. 11) for
793 p_a = 14.5 kbar and for the same values of t_C and Ω_1 = 0.33 as for the simulation shown in
794 figure 15A to D. This simulation also shows the formation of elongated regions of high ϕ,
795 oriented parallel to σ_1 (Fig. 15E to H). For both simulations shown in figure 15 the final
796 dimensionless time is now > 1, indicating that t_C is shorter than the duration of shearing so
797 that significant fluid flow can occur during the shearing. The two simulations with p_a = 14.5
798 kbar and Ω_1 = 0.33 show that during shearing of serpentinite without reaction, that is during
799 the formation of serpentinite mylonites, elongated high-porosity regions, with lower shear
800 viscosity might have formed. The formation of such elongated high-porosity regions could
801 have been one mechanism causing the formation of shear bands in the antigorite serpentinite
802 which are frequently observed in the Erro Tobbio region. Once p_a will become close to the
803 reaction pressure, due to continued burial, these high-porosity, low-viscosity fluid bands

might then have favored the generation of olivine veins, similar to our simulations with an oblique initial Gaussian ϕ distribution.

5.4. Simplifications

The modelled process involves the coupling of a metamorphic reaction, porous fluid flow and rock deformation and, hence, the studied process and the applied HMC model are already quite complex. On the other hand, we needed to simplify each of the hydraulic, mechanical and chemical processes to develop the mathematical model.

For the hydraulic process, we consider a standard Darcy flow model with a specific porosity dependent (cubic dependence using $k\phi^3$), isotropic permeabilty. This exponent of ϕ can also differ from 3 and values between 1 and 25 have been reported (e.g. David et al., 1994). Furthermore, this exponent can also vary during a compaction process (e.g., Hommel et al., 2018), the porosity-permeability relations could be more complex (e.g. Costa, 2006; Hommel et al., 2018) and/or the porosity-permeability relation could also be spatially variable in the serpentinite. Therefore, there is considerable uncertainty concerning the natural porosity-permeability relation in the serpentnite, especially at 12.75 kbar and 500 °C ambient pressure and temperature, respectively.

For the mechanical shearing process, we consider a flow law in which the shear viscosity is only a function of porosity. In a natural serpentinite with constant porosity, the relationship between deviatoric stress and strain rate could be nonlinear due to an effective shear viscosity that depends on the stress magnitude, the mineral grain size and the chemical composition. Such nonlinearity can be mathematically represented by a power-law relationship between deviatoric stress, τ, and strain rate, D, of the form $\tau^m \approx D$ (e.g. Montesi and Zuber, 2002). If $m \gg 1$, then τ increases insignificantly with increasing D. To

828 test the impact of such nonlinear stress-strain rate relationships, we have performed also
829 simulations with a pressure-insensitive yield stress, in which stress remains constant for
830 increasing strain rate and which represents a considerably nonlinear flow law for $m \gg 1$.
831 Concerning the effective shear viscosities: During olivine vein formation, ρ_s changes
832 continuously from ρ_s for serpentinite to ρ_s for olivine indicating a transient transformation
833 from brucite to olivine (Fig. 9). Furthermore, in modelled regions with ρ_s > 3000 kg/m^3,
834 values of ϕ > 0.4 (Fig. 11). In nature, the fluid is likely distributed along mineral grain
835 boundaries and we assume that a mixture of transforming brucite-olivine grains and fluid with
836 ϕ > 0.4 has a low effective shear viscosity. An individual, fully transformed olivine grain has
837 a much larger shear viscosity and could potentially also deform in a frictional-plastic manner
838 at 500 °C. Moreover, we apply a constant value of a for the exponential $\eta_s - \phi$ relationship
839 (equation (10)) over the entire ϕ range between 0.02 and ~0.6. However, a could also vary
840 with ϕ, especially for higher values of ϕ > ~0.2.

841 For the chemical process, we consider, for simplicity, a fixed chemical composition
842 for which forsterite + water results from dehydration of antigorite + brucite + a small amount
843 of free water. We consider this small amount of free water simply to be able to apply the
844 governing two-phase equations for solid-fluid mixtures in the entire model domain and to
845 calculate thermodynamically the fluid density in the stability field of antigorite + brucite (Fig.
846 3C). Natural chemical compositions, in for example the Erro-Tobbio unit, are more complex
847 and feature a higher chemical variability as considered in our model. However, the main aim
848 of our study is to investigate the fundamental coupling between dehydration reactions, fluid
849 flow and rock deformation, justifying the use of a simplified MSH system. A more elaborated
850 system would be the FMASH system which also considers aluminium, Al, and iron, Fe (e.g.,
851 Padrón-Navarta et al., 2013). One effect of the FMASH system, applied to our isothermal

852 model, would be that both brucite and olivine could be stable at the same pressure over a
853 range of pressure, within a so-called divariant field (e.g., Padrón-Navarta et al., 2013).
854 Consequently, the H_2O liberation would not be controlled by a specific pressure, but would
855 rather occur over a pressure interval. Such pressure interval is already considered in our
856 model, because the modelled reaction does not occur sharply at one specific fluid pressure,
857 but over an interval between 12.6 and 12.7 kbar. Considering a FMASH system would allow
858 to constrain this pressure interval better. Furthermore, our model suggests that natural areas of
859 serpentinite dehydration, consisting of olivine and water, are mechanically weak due to their
860 high, up to 0.6, porosity and water content; as proposed by Hermann et al. (2000). After the
861 formation of the dehydration veins, the water eventually escapes the dehydration region, so
862 that finally only olivine is left in the veins.

863

864 *5.5. Potential applications to deep-seated slow slip and tremor*

865 The presented model could potentially be applied to investigate fluid-related processes
866 causing episodic tremor and slow-slip events (ETS; e.g., Behr and Bürgmann, 2021; Peng &
867 Gomberg 2010). Despite the lack of consensus on the inter-relationships between mineral
868 dehydration, fluid flow, critical stress and ETS, the coincidence of the location of low-
869 frequency earthquakes to regions with high Vp/Vs ratios requires the consideration of fluid
870 flow and mineral dehydration in these settings (e.g., Behr and Bürgmann 2021; Burlini et al.
871 2009; Kato et al. 2010; Shelly et al. 2006; Van Avendonk et al., 2010). For example, Van
872 Avendonk et al. (2010) infer a zone of very high Vp/Vs of 6 at the top of the subducting
873 Cocos slab between 35 and 55 km depth, lying downdip of the seismogenic zone. They
874 propose that these high Vp/Vs ratios are due to several-meter thick shear zones under high
875 pore pressure and that the hydrous pore fluids were generated by prograde dehydration
876 reactions. The 35 to 55 km depth range with inferred high Vp/Vs ratios corresponds to the

depth range and ambient pressure considered in our model. In addition, the correlation of rapid-tremor migration to pore-pressure waves suggests that this coincidence can be explained by the coupled processes of dehydration, fault weakening and tremor migration (e.g., Van Avendonk et al. 2010; Cruz-Atienz et al. 2018). Thus, the formation of fluid-filled veins, as modelled here, can be correlated to the transient weakening that is inferred in regions of mineral dehydration. Furthermore, the dehydration reaction, generating olivine-fluid bearing veins, and the subsequent fluid escape, leaving behind olivine-only veins, will cause a viscosity inversion: when significant fluid is present in the olivine bearing veins, then the effective viscosity of the olivine-fluid veins is smaller than the viscosity of the serpentinite; but once the fluid has escaped the veins the effective viscosity of the olivine-only veins is larger than the viscosity of the serpentinte. Such viscosity variation and inversion likely strongly impacts the spatial and temporal evolution of the stress in the serpentinites. We predict that, under the presence of a general anisotropic stress field, the vein formation will lead to an increase of the anisotropic effective viscosity of the subducted mantle rocks as a result of the different effective viscosities of serpentinite and olivine + fluid assemblages. When the fluid is completely drained from these veins, the anisotropy and viscosity contrast between olivine and serpentinite will be permanent.

6. Conclusions

We developed an isothermal 2D hydro-mechanical-chemical model to investigate the generation of dehydration veins in a ductily deforming serpentinite for the reaction antigorite + brucite = forsterite + water. The model predicts shear-driven formation of dehydration veins and, hence, supports the hypothesis of shear-driven formation of metamorphic olivine veins in the antigorite serpentinites of the Erro Tobbio unit (Fig. 1).

The fluid and total pressures are initially homogeneous in the model and correspond to the serpentinite stability field. The applied model, hence, does not *a priori* prescribe that dehydration takes place. In contrast, the model is able to predict the self-consistent generation of fluid pressure perturbations during shearing of mechanically heterogeneous serpentinite, which trigger the dehydration reaction and cause the formation of olivine veins. The modelled veins consist of a weak forsterite-water mixture and grow in a direction parallel to the maximal principal stress which is controlled by the applied far-field simple shearing. The modelled growth of dehydration veins is not an unstable, or runaway, process, but a self-limiting process because the fluid pressure perturbations that drive dehydration decrease during progressive shearing due to fluid flow.

The applied initial porosity geometry and a pressure-insensitive yield strength, mimicking a strongly stress dependent effective viscosity, have a minor impact on olivine vein formation. In contrast, the applied ambient fluid pressure and the relationship between compaction length and porosity have a strong impact on olivine vein formation. For the applied model configuration, a shear viscosity with exponential dependence on porosity (i) provides a compaction length which first increases and subsequently decreases with increasing porosity and (ii) is most suitable for the formation of olivine veins.

The rate of porosity production during dehydration is controlled by the rates of three mechanisms: the rate of solid volumetric change, the rate of solid density change and the rate of reactive mass transfer. All three mechanisms contribute in approximately equal parts to the porosity production during shearing.

Olivine veins are observed in several high pressure serpentinites in the Western Alps and Liguria. The modelled veins have a similar orientation as natural en échelon olivine veins in serpentinite mylonite. The self-limiting feature of the modelled vein growth might also explain the natural observation of many smaller olivine veins and the absence of few large

olivine veins. Furthermore, the presented model can explain transient weakening and the generation of mechanical anisotropy during dehydration when the elongated, parallel and high-porosity veins consist of a fluid-olivine mixture. The eventual escape of the fluids will cause a viscosity and anisotropy inversion since olivine-only veins are stronger than serpentinite. Such transient weakening, anisotropy generation and viscosity inversion may be important processes during slow slip and tremor observed at subduction zones. Rescaling of the model results to natural conditions suggests that the serpentinite should have been effectively impermeable, with ambient permeabilities smaller than approximately 10^{-24} m^2, during olivine vein formation and the shearing rate should have been in the order of 10^{-9} s^{-1}, presumably during periods of slow slip.

Acknowledgements

S.M.S. is grateful for theoretical advices from Y. Podladchikov and for practical programming help of T. Duretz. This work was supported by the University of Lausanne and the Swiss Geocomputing Centre. E.M. acknowledges the Johannes Gutenberg University of Mainz for financial support. L.R. acknowledges financial support from the Swiss University Conference and the Swiss Council of Federal Institutes of Technology through the Platform for Advanced Scientific Computing (PASC) program, obtained via the PASC project GPU4GEO. O.M. is grateful for scientific discussions with M. Scambelluri and J. Hermann in the field, where the idea of weak olivine veins was born 30 years ago. There is no conflict of interest.

Availability Statement

The Julia programming language used in the scope of this study is licensed under MIT License. The latest version of the code is available for download from GitHub at: https://github.com/PTsolvers/PseudoTransientHMC.jl (last access: 05 April 2023). Past and future versions of the software are available from a permanent DOI repository (Zenodo) at: https://doi.org/10.5281/zenodo.7797414 (Schmalholz and Räss, 2023). The codes are written using the Julia programming language and execute on graphical processing units (GPUs). Refer to the repository's README for additional information.

Appendix

A1. Numerical algorithm

To determine the unknowns p_f, p, ϕ, v_x^s and v_y^s we employ the iterative accelerated pseudo-transient (PT) method (Räss et al., 2022) using a finite difference discretization on a regular Cartesian staggered grid, described in Schmalholz et al. (2020). For example, equation (7) is used to solve for ϕ. Therefore, a PT derivative of ϕ, written as $\Delta^{PT}\phi / \Delta t_\varphi^{PT}$, is added to the left-hand side of equation (7), which yields

$$\frac{\Delta^{PT}\phi}{\Delta t_\varphi^{PT}} = \frac{\partial}{\partial t}\left[\rho_X\left(1-\phi\right)\right] + \nabla\cdot\left[\rho_X\left(1-\phi\right)\mathbf{v}^s\right]. \tag{A1}$$

Within a PT iteration loop the value of ϕ is iteratively updated and the value of $\Delta^{PT}\phi / \Delta t_\varphi^{PT}$ converges towards zero during the interations. The iterations are stopped once the value of $\Delta^{PT}\phi / \Delta t_\varphi^{PT}$ is smaller than a specified tolerance value. This tolerance value corresponds to the residual of the numerically solved PDE (see also Halter et al., 2022). The unknowns p_f, p, v_x^s and v_y^s are determined with the same PT method within the same iteration loop. The system of PT equations is:

$$\begin{aligned}
\frac{\Delta^{PT} p_f}{\Delta t_{pf}^{PT}} &= -\frac{\partial \rho_T}{\partial t} + \nabla\cdot\left[\rho_f \frac{k\phi^3}{\eta_f}\nabla p_f\right] - \nabla\cdot\left(\rho_T \mathbf{v}^s\right) \\
\frac{\Delta^{PT}\phi}{\Delta t_\varphi^{PT}} &= \frac{\partial}{\partial t}\left[\rho_X\left(1-\phi\right)\right] + \nabla\cdot\left[\rho_X\left(1-\phi\right)\mathbf{v}^s\right] \\
\frac{\Delta^{PT} v_i^s}{\Delta t_v^{PT}} &= \nabla\cdot\sigma_{ij} \\
\frac{\Delta^{PT} p}{\Delta t_p^{PT}} &= -\nabla\cdot\mathbf{v}^s - \frac{1}{K_d}\left(\frac{dp}{dt} - \alpha\frac{dp_f}{dt}\right) - \frac{p-p_f}{\left(1-\phi\right)\lambda}
\end{aligned} \tag{A2}$$

To discretize the physical time derivatives, such as $\partial \rho_T / \partial t$, we employ a "physical" time step, Δt. The applied values of Δt and of the pseudo-transient (PT), Δt^{PT}, time steps are typically:

$$
\begin{aligned}
\Delta t &= 4 \times 10^{-6} \frac{r^2 \eta_f}{k \phi_a^3 K_s} \\
\Delta t_{\phi}^{PT} &= \Delta t \\
\Delta t_{pf}^{PT} &= C_{pf} \frac{\max\left(\Delta x, \Delta y\right)^2}{\max\left(\frac{k \phi^3 K_s}{\eta_f}\right)} \\
\Delta t_{v}^{PT} &= C_{v} \frac{\max\left(\Delta x, \Delta y\right)^2}{\max\left(\eta^s\right)} \\
\Delta t_{p}^{PT} &= C_{p} \frac{\max\left(\eta^s\right) dx}{w}
\end{aligned}
\tag{A3}
$$

where Δx and Δy are horizontal and vertical numerical grid spacing, respectively, and the values of the factors C_{pf}, C_v and C_p can vary for different simulations, mainly to reduce the number of required PT iteration loops. More information concerning the choice of such PT time steps can be found in Räss et al. (2022) and Wang et al. (2022). Upon convergence, these iterations provide results which are equivalent to results of a numerical-implicit method, since the gradients of the numerical variables are updated in each iteration.

For reasons of numerical efficiency, we approximate the thermodynamic relations of the densities and mass fractions with the fluid pressure, obtained with Gibbs free-energy minimization, with analytical functions (Fig. 3C and D):

$$\rho_f = 1194 \times \ln\left(\frac{p_f}{p_{ini}} + 1\right)^{1/3.5}$$

$$\rho_s^{EQ} = -\tanh\left(600 \times \frac{p_f - p_R}{p_{ini}}\right) \times 323.32 + 2848 + \left(\frac{p_f}{p_{ini}} - 0.0078\right) \times 30.4762 \qquad \text{(A4)}$$

$$X_s^{EQ} = -\tanh\left(600 \times \frac{p_f - p_R}{p_{ini}}\right) \times 0.1292 + 0.8707$$

where p_R is the reaction pressure, here 12.65 kbar. We use the functions above in the numerical algorithm to calculate densities and mass fraction from the current fluid pressure. We provide a general overview, in the form of a simple flowchart, of the structure of the numerical algorithm and the order of the governing equations in which they are solved in figure A1.

A2. Numerical resolution and accuracy test

We present here the results of a numerical resolution and accuracy test. Such tests are essential to determine whether the evolution of the dehydrating region is independent of (1) the employed numerical resolution and (2) the applied tolerance to exit the PT iteration loop. We performed the simulation shown in figure 7E to H with the following different numerical resolutions: 500×500, 700×700 and 900×900 grid points (Fig. A2). For a dimensionless model time of 0.036, the ratio of the maximum porosity in the model domain divided by the maximum porosity for a simulation with 900 × 900 grid points is plotted versus the corresponding resolution for simulations with different resolution (Fig. A2A). Similar ratios are plotted for the minimum fluid pressure in the model domain and the average value of the fluid velocity. The higher the resolution, the less the three ratios vary, indicating the convergence of the numerical results upon increasing numerical resolution. The evolution of the minimum fluid pressure in the model domain with time is shown for different numerical

1005 resolutions (Fig. A2B). With larger numerical resolution, the temporal evolution of the
1006 minimum fluid pressure varies less, indicating again the convergence of the numerical results
1007 for increasing numerical resolution. Finally, the spatial distribution of p_f at a dimensionless
1008 time of 0.036 is displayed for the three different resolutions (Fig. A2C to E). For numerical
1009 resolutions of 500×500, 700×700 and 900×900 the contours of p_f are smooth and the
1010 colormaps of p_f are very similar (Fig. A2C to E). The numerical resolution test shows that
1011 the applied numerical model provides results which converge for increasing numerical
1012 resolution and are, hence, not dependent on the numerical resolution. For the presented
1013 numerical simulations, a numerical resolution of 900×900 was applied.

1014 We present also a test for the numerical accuracy of the applied iterative PT solver. If
1015 the partial differential equations are solved correctly, then the left hand sides of equations
1016 (A2) are zero. However, since these equations are solved with numerical approximations, the
1017 value of the left hand side of the numerical form of equations (A2) is not exactly equal to
1018 zero. The deviation from zero is typically called a residual. During the iterative solution,
1019 iterations are performed until all residuals at all numerical grid points for all equations
1020 decrease below a certain tolerance value. We calculated the first time step for a the simulation
1021 shown in figure 7E to H for different values of the tolerance (Fig. A3). We choose three
1022 representative quantities to test their change with a change of the tolerance. These quantities
1023 are the minimum fluid pressure in the model domain, the maximal total pressure in the model
1024 domain and the maximal value of the second invariant of the deviatric stress tensor (Fig. A3).
1025 All three quantities stop changing once the tolerance decreases below a value of 10^{-6}. The
1026 results presented in figure A3 show the convergence of the results with decreasing tolerance.
1027 A tolerance of 10^{-6} was applied in the presented simulations.

References

Aharonov, E., M. Spiegelman, and P. Kelemen (1997), Three-dimensional flow and reaction in porous media: Implications for the Earth's mantle and sedimentary basins, Journal of Geophysical Research-Solid Earth, 102(B7), 14821-14833, doi:10.1029/97jb00996.

Audet, P., M. G. Bostock, N. I. Christensen, and S. M. Peacock (2009), Seismic evidence for overpressured subducted oceanic crust and megathrust fault sealing, Nature, 457(7225), 76-78, doi:10.1038/nature07650.

Baltzell, C., E. M. Parmentier, Y. Liang, and S. Tirupathi (2015), A high-order numerical study of reactive dissolution in an upwelling heterogeneous mantle: 2. Effect of shear deformation, Geochemistry Geophysics Geosystems, 16(11), 3855-3869, doi:10.1002/2015gc006038.

Bebout, G. E. (2014), Chemical and Isotopic Cycling in Subduction Zones, in Treatise on Geochemistry, edited by H. D. Holland and K. K. Turekian, pp. 703-747, Elsevier.

Behr, W. M., and R. Bürgmann (2021), Whats down there? The structures, materials and environment of deep-seated tremor and slip.

Beinlich, A., T. John, J. Vrijmoed, M. Tominaga, T. Magna, and Y. Podladchikov (2020), Instantaneous rock transformations in the deep crust driven by reactive fluid flow, Nature Geoscience, 13(4), 307-311.

Bessat, A., S. Pilet, Y. Y. Podladchikov, and S. M. Schmalholz (2022), Melt Migration and Chemical Differentiation by Reactive Porosity Waves, Geochemistry Geophysics Geosystems, 23(2), doi:10.1029/2021gc009963.

1050 Bloch, W., T. John, J. Kummerow, P. Salazar, O. S. Krüger, and S. A. Shapiro (2018),
1051 Watching Dehydration: Seismic Indication for Transient Fluid Pathways in the Oceanic
1052 Mantle of the Subducting Nazca Slab, Geochemistry, Geophysics, Geosystems, 19(9), 3189-
1053 3207, doi:https://doi.org/10.1029/2018GC007703.

1054 Brantut, N., J. Sulem, and A. Schubnel (2011), Effect of dehydration reactions on earthquake
1055 nucleation: Stable sliding, slow transients, and unstable slip, Journal of Geophysical
1056 Research: Solid Earth, 116(B5).

1057 Burlini, L., G. Di Toro, and P. Meredith (2009), Seismic tremor in subduction zones: Rock
1058 physics evidence, Geophysical Research Letters, 36, doi:10.1029/2009gl037735.

1059 Chernak, L. J., and G. Hirth (2010), Deformation of antigorite serpentinite at high temperature
1060 and pressure, Earth and Planetary Science Letters, 296(1-2), 23-33,
1061 doi:10.1016/j.epsl.2010.04.035.

1062 Chorin, A. J. (1997), A numerical method for solving incompressible viscous flow problems,
1063 Journal of computational physics, 135(2), 118-125.

1064 Cionoiu, S., E. Moulas, and L. Tajčmanová (2019), Impact of interseismic deformation on
1065 phase transformations and rock properties in subduction zones, Scientific Reports, 9(1), 1-6.

1066 Connolly, J. (1990), Multivariable phase diagrams; an algorithm based on generalized
1067 thermodynamics, American Journal of Science, 290(6), 666-718.

1068 Connolly, J. (1997), Devolatilization-generated fluid pressure and deformation-propagated
1069 fluid flow during prograde regional metamorphism, Journal of Geophysical Research: Solid
1070 Earth, 102(B8), 18149-18173.

1071 Connolly, J. (2005), Computation of phase equilibria by linear programming: a tool for
1072 geodynamic modeling and its application to subduction zone decarbonation, Earth and
1073 Planetary Science Letters, 236(1-2), 524-541.

1074 Connolly, J. (2009), The geodynamic equation of state: What and how, Geochemistry
1075 Geophysics Geosystems, 10, doi:10.1029/2009gc002540.

1076 Costa, A. (2006), Permeability-porosity relationship: A reexamination of the Kozeny-Carman
1077 equation based on a fractal pore-space geometry assumption, Geophysical research letters,
1078 33(2).

1079 Cruz-Atienza, V. M., C. Villafuerte, and H. S. Bhat (2018), Rapid tremor migration and pore-
1080 pressure waves in subduction zones, Nature Communications, 9(1), 2900,
1081 doi:10.1038/s41467-018-05150-3.

1082 Dahlen, F. A. (1992), Metamorphism of nonhydrostatically stressed rocks, American Journal
1083 of Science, 292(3), 184-198.

1084 David, T.-F. Wong, W. Zhu, and J. Zhang (1994), Laboratory measurement of compaction-
1085 induced permeability change in porous rocks: Implications for the generation and
1086 maintenance of pore pressure excess in the crust, pure and applied geophysics, 143, 425-456.

1087 David, E. C., N. Brantut, L. N. Hansen, and T. M. Mitchell (2018), Absence of Stress-Induced
1088 Anisotropy During Brittle Deformation in Antigorite Serpentinite, Journal of Geophysical
1089 Research-Solid Earth, 123(12), 10616-10644, doi:10.1029/2018jb016255.

1090 Dohmen, J., and H. Schmeling (2021), Magma ascent mechanisms in the transition regime
1091 from solitary porosity waves to diapirism, Solid Earth, 12(7), 1549-1561.

1092 England, P. C., and A. J. Smye (2023), Metamorphism and Deformation on Subduction
1093 Interfaces: 1. Physical Framework, Geochemistry, Geophysics, Geosystems, 24(1),
1094 e2022GC010644.

1095 Evans, O., M. Spiegelman, and P. B. Kelemen (2020), Phase-Field Modeling of Reaction-
1096 Driven Cracking: Determining Conditions for Extensive Olivine Serpentinization, Journal of
1097 Geophysical Research: Solid Earth, 125(1), e2019JB018614.

1098 Fowler, A. C. (1985), A mathematical model of magma transport in the asthenosphere,
1099 Geophysical & Astrophysical Fluid Dynamics, 33(1-4), 63-96,
1100 doi:10.1080/03091928508245423.

1101 Frank, W. B., N. M. Shapiro, A. L. Husker, V. Kostoglodov, H. S. Bhat, and M. Carnpillo
1102 (2015), Along-fault pore-pressure evolution during a slow-slip event in Guerrero, Mexico,
1103 Earth and Planetary Science Letters, 413, 135-143, doi:10.1016/j.epsl.2014.12.051.

1104 Gomberg, J., Cascadia, and B. W. Group (2010), Slow-slip phenomena in Cascadia from
1105 2007 and beyond: A review, Bulletin, 122(7-8), 963-978.

1106 Hacker, B. R., S. M. Peacock, G. A. Abers, and S. D. Holloway (2003), Subduction factory 2.
1107 Are intermediate-depth earthquakes in subducting slabs linked to metamorphic dehydration
1108 reactions?, Journal of Geophysical Research: Solid Earth, 108(B1).

1109 Halter, W. R., E. Macherel, and S. M. Schmalholz (2022), A simple computer program for
1110 calculating stress and strain rate in 2D viscous inclusion-matrix systems, Journal of Structural
1111 Geology, 160, 104617.

1112 Hatakeyama, K., I. Katayama, K.-i. Hirauchi, and K. Michibayashi (2017), Mantle hydration
1113 along outer-rise faults inferred from serpentinite permeability, Scientific Reports, 7(1), 13870,
1114 doi:10.1038/s41598-017-14309-9.

1115 Hebert, L. B., P. Antoshechkina, P. Asimow, and M. Gurnis (2009), Emergence of a low-
1116 viscosity channel in subduction zones through the coupling of mantle flow and
1117 thermodynamics, Earth and Planetary Science Letters, 278(3-4), 243-256,
1118 doi:10.1016/j.epsl.2008.12.013.

1119 Hermann, J., O. Müntener, and M. Scambelluri (2000), The importance of serpentinite
1120 mylonites for subduction and exhumation of oceanic crust, Tectonophysics, 327(3-4), 225-
1121 238.

1122 Hilairet, N., B. Reynard, Y. B. Wang, I. Daniel, S. Merkel, N. Nishiyama, and S. Petitgirard
1123 (2007), High-pressure creep of serpentine, interseismic deformation, and initiation of
1124 subduction, Science, 318(5858), 1910-1913, doi:10.1126/science.1148494.

1125 Hirauchi, K., I. Katayama, and Y. Kouketsu (2020), Semi-brittle deformation of antigorite
1126 serpentinite under forearc mantle wedge conditions, Journal of Structural Geology, 140,
1127 doi:10.1016/j.jsg.2020.104151.

1128 Holland, T., and R. Powell (1998), An internally consistent thermodynamic data set for
1129 phases of petrological interest, Journal of metamorphic Geology, 16(3), 309-343.

1130 Holtzman, B., N. Groebner, M. Zimmerman, S. Ginsberg, and D. Kohlstedt (2003), Stress-
1131 driven melt segregation in partially molten rocks, Geochemistry, Geophysics, Geosystems,
1132 4(5).

1133 Hommel, J., E. Coltman, and H. Class (2018), Porosity–permeability relations for evolving
1134 pore space: a review with a focus on (bio-) geochemically altered porous media, Transport in
1135 Porous Media, 124(2), 589-629.

1136 Huber, K., J. C. Vrijmoed, and T. John (2022), Formation of Olivine Veins by Reactive Fluid
1137 Flow in a Dehydrating Serpentinite, Geochemistry, Geophysics, Geosystems, 23(6),
1138 e2021GC010267, doi:https://doi.org/10.1029/2021GC010267.

1139 John, T., N. Gussone, Y. Y. Podladchikov, G. E. Bebout, R. Dohmen, R. Halama, R. Klemd,
1140 T. Magna, and H. M. Seitz (2012), Volcanic arcs fed by rapid pulsed fluid flow through
1141 subducting slabs, Nature Geoscience, 5(7), 489-492, doi:10.1038/ngeo1482.

1142 Jones, D. W. R., and R. F. Katz (2018), Reaction-infiltration instability in a compacting
1143 porous medium, Journal of Fluid Mechanics, 852, 5-36.

1144 Karato, S. (2008), Deformation of Earth materials, Cambridge University Press, Cambridge.

1145 Kato, A., et al. (2010), Variations of fluid pressure within the subducting oceanic crust and
1146 slow earthquakes, Geophysical Research Letters, 37, doi:10.1029/2010gl043723.

1147 Katz, R. F., D. W. R. Jones, J. F. Rudge, and T. Keller (2022), Physics of melt extraction from
1148 the mantle: speed and style, Annual Review of Earth and Planetary Sciences, 50, 507-540.

1149 Katz, R. F., M. Spiegelman, and B. Holtzman (2006), The dynamics of melt and shear
1150 localization in partially molten aggregates, Nature, 442(7103), 676-679.

1151 Keller, T., and R. F. Katz (2016), The role of volatiles in reactive melt transport in the
1152 asthenosphere, Journal of Petrology, 57(6), 1073-1108.

1153 Keller, T., D. A. May, and B. J. Kaus (2013), Numerical modelling of magma dynamics
1154 coupled to tectonic deformation of lithosphere and crust, Geophysical Journal International,
1155 195(3), 1406-1442.

1156 Kempf, E. D., J. Hermann, E. Reusser, L. P. Baumgartner, and P. Lanari (2020), The role of
1157 the antigorite + brucite to olivine reaction in subducted serpentinites (Zermatt, Switzerland)
1158 (vol 113, 16, 2020), Swiss Journal of Geosciences, 113(1), doi:10.1186/s00015-020-00377-z.

Kolditz, O., H. Shao, W. Wang, and S. Bauer (2016), Thermo-hydro-mechanical chemical processes in fractured porous media: modelling and benchmarking, 313 pp., Springer, doi:10.1007/978-3-319-11894-9.

Labrousse, L., G. Hetenyi, H. Raimbourg, L. Jolivet, and T. B. Andersen (2010), Initiation of crustal-scale thrusts triggered by metamorphic reactions at depth: Insights from a comparison between the Himalayas and Scandinavian Caledonides, Tectonics, 29, doi:10.1029/2009tc002602.

Llana-Fúnez, S., J. Wheeler, and D. R. Faulkner (2012), Metamorphic reaction rate controlled by fluid pressure not confining pressure: implications of dehydration experiments with gypsum, Contributions to Mineralogy and Petrology, 164(1), 69-79, doi:10.1007/s00410-012-0726-8.

Malvoisin, B., Y. Y. Podladchikov, and A. V. Myasnikov (2021), Achieving complete reaction while the solid volume increases: Anumerical model applied to serpentinisation, Earth and Planetary Science Letters, 563, doi:10.1016/j.epsl.2021.116859.

Matter, J. M., and P. B. Kelemen (2009), Permanent storage of carbon dioxide in geological reservoirs by mineral carbonation, Nature Geoscience, 2(12), 837-841, doi:10.1038/ngeo683.

McKee, S., M. F. Tomé, V. G. Ferreira, J. A. Cuminato, A. Castelo, F. Sousa, and N. Mangiavacchi (2008), The MAC method, Computers & Fluids, 37(8), 907-930.

McKenzie, D. (1984), The generation and compaction of partially molten rock, J. Petrology, 25, 713-765.

Mei, S., W. Bai, T. Hiraga, and D. Kohlstedt (2002), Influence of melt on the creep behavior of olivine–basalt aggregates under hydrous conditions, Earth and Planetary Science Letters, 201(3-4), 491-507.

1182 Montesi, L. G. J., and M. T. Zuber (2002), A unified description of localization for
1183 application to large-scale tectonics, Journal of Geophysical Research-Solid Earth, 107(B3),
1184 doi:204510.1029/2001jb000465.

1185 Moulas, E., J.-P. Burg, and Y. Podladchikov (2014), Stress field associated with elliptical
1186 inclusions in a deforming matrix: Mathematical model and implications for tectonic
1187 overpressure in the lithosphere, Tectonophysics, 631, 37-49, doi:10.1016/j.tecto.2014.05.004.

1188 Moulas, E., and S. M. Schmalholz (2020), The importance of interfacial instability for viscous
1189 folding in mechanically heterogeneous layers, Geological Society, London, Special
1190 Publications, 487(1), 45-58.

1191 Moulas, E., S. M. Schmalholz, Y. Podladchikov, L. Tajčmanová, D. Kostopoulos, and L.
1192 Baumgartner (2019), Relation between mean stress, thermodynamic, and lithostatic pressure,
1193 Journal of metamorphic geology, 37(1), 1-14.

1194 Omlin, S., B. Malvoisin, and Y. Y. Podladchikov (2017), Pore fluid extraction by reactive
1195 solitary waves in 3-D, Geophysical Research Letters, 44(18), 9267-9275.

1196 Padrón-Navarta, J. A., V. L. Sánchez-Vizcaíno, J. Hermann, J. A. Connolly, C. J. Garrido, M.
1197 T. Gómez-Pugnaire, and C. Marchesi (2013), Tschermak's substitution in antigorite and
1198 consequences for phase relations and water liberation in high-grade serpentinites, Lithos, 178,
1199 186-196.

1200 Pandey, S. N., V. Vishal, and A. Chaudhuri (2018), Geothermal reservoir modeling in a
1201 coupled thermo-hydro-mechanical-chemical approach: A review, Earth-Science Reviews,
1202 185, 1157-1169, doi:10.1016/j.earscirev.2018.09.004.

1203 Patankar, S. (2018), Numerical heat transfer and fluid flow, Taylor & Francis.

1204 Peacock, S. M. (1990), Fluid processes in subduction zones, Science, 248(4953), 329-337,
1205 doi:10.1126/science.248.4953.329.

1206 Peng, Z. G., and J. Gomberg (2010), An integrated perspective of the continuum between
1207 earthquakes and slow-slip phenomena, Nature Geoscience, 3(9), 599-607,
1208 doi:10.1038/ngeo940.

1209 Peters, D., T. Pettke, T. John, and M. Scambelluri (2020), The role of brucite in water and
1210 element cycling during serpentinite subduction – Insights from Erro Tobbio (Liguria, Italy),
1211 Lithos, 360-361, 105431, doi:https://doi.org/10.1016/j.lithos.2020.105431.

1212 Pettke, T., and A. Bretscher (2022), Fluid-mediated element cycling in subducted oceanic
1213 lithosphere: The orogenic serpentinite perspective, Earth-Science Reviews, 225,
1214 doi:10.1016/j.earscirev.2021.103896.

1215 Plümper, O., T. John, Y. Y. Podladchikov, J. C. Vrijmoed, and M. Scambelluri (2017), Fluid
1216 escape from subduction zones controlled by channel-forming reactive porosity, Nature
1217 Geoscience, 10(2), 150-156.

1218 Poulet, T., A. Karrech, K. Regenauer-Lieb, L. Fisher, and P. Schaubs (2012), Thermal–
1219 hydraulic–mechanical–chemical coupling with damage mechanics using ESCRIPTRT and
1220 ABAQUS, Tectonophysics, 526, 124-132.

1221 Poulet, T., M. Veveakis, M. Herwegh, T. Buckingham, and K. Regenauer-Lieb (2014),
1222 Modeling episodic fluid-release events in the ductile carbonates of the Glarus thrust,
1223 Geophysical Research Letters, 41(20), 7121-7128, doi:10.1002/2014gl061715.

1224 Räss, L., T. Duretz, and Y. Podladchikov (2019a), Resolving hydromechanical coupling in
1225 two and three dimensions: spontaneous channelling of porous fluids owing to decompaction
1226 weakening, Geophysical Journal International, 218(3), 1591-1616.

Räss, L., D. Kolyukhin, and A. Minakov (2019b), Efficient parallel random field generator for large 3-D geophysical problems, Computers & Geosciences, 131, 158-169, doi:10.1016/j.cageo.2019.06.007.

Räss, L., I. Utkin, T. Duretz, S. Omlin, and Y. Y. Podladchikov (2022), Assessing the robustness and scalability of the accelerated pseudo-transient method, Geosci. Model Dev., 15(14), 5757-5786, doi:10.5194/gmd-15-5757-2022.

Rupke, L. H., J. P. Morgan, M. Hort, and J. A. D. Connolly (2004), Serpentine and the subduction zone water cycle, Earth and Planetary Science Letters, 223(1-2), 17-34, doi:10.1016/j.epsl.2004.04.018.

Scambelluri, M., J. Fiebig, N. Malaspina, O. Muntener, and T. Pettke (2004), Serpentinite subduction: Implications for fluid processes and trace-element recycling, International Geology Review, 46(7), 595-613, doi:10.2747/0020-6814.46.7.595.

Scambelluri, M., O. Muntener, J. Hermann, G. B. Piccardo, and V. Trommsdorff (1995), Subduction of water into the mantle - history of an Alpine peridotite, Geology, 23(5), 459-462, doi:10.1130/0091-7613(1995)023<0459:Sowitm>2.3.Co;2.

Scambelluri, M., E. H. H. Strating, G. B. Piccardo, R. L. M. Vissers, and E. Rampone (1991), Alpine olivine-bearing and titanium clinohumite-bearing assemblages in the Erro Tobbio peridotite (Voltri-massif, NW Italy), Journal of Metamorphic Geology, 9(1), 79-91, doi:10.1111/j.1525-1314.1991.tb00505.x.

Schiemenz, A., Y. Liang, and E. M. Parmentier (2011), A high-order numerical study of reactive dissolution in an upwelling heterogeneous mantle-I. Channelization, channel lithology and channel geometry, Geophysical Journal International, 186(2), 641-664, doi:10.1111/j.1365-246X.2011.05065.x.

Schmalholz, S. M., and R. C. Fletcher (2011), The exponential flow law applied to necking and folding of a ductile layer, Geophysical Journal International, 184(1), 83-89, doi:10.1111/j.1365-246X.2010.04846.x.

Schmalholz, S. M., E. Moulas, O. Plumper, A. V. Myasnikov, and Y. Y. Podladchikov (2020), 2D Hydro-Mechanical-Chemical Modeling of (De)hydration Reactions in Deforming Heterogeneous Rock: The Periclase-Brucite Model Reaction, Geochemistry Geophysics Geosystems, 21(11), doi:10.1029/2020gc009351.

Schmalholz, S. M., and L. Räss (2023), PTsolvers/PseudoTransientHMC.jl: PseudoTransientHMC.jl 0.1.0 (v0.1.0), edited, Zenodo, doi:https://doi.org/10.5281/zenodo.7797414.

Schmeling, H., J. P. Kruse, and G. Richard (2012), Effective shear and bulk viscosity of partially molten rock based on elastic moduli theory of a fluid filled poroelastic medium, Geophysical Journal International, 190(3), 1571-1578, doi:10.1111/j.1365-246X.2012.05596.x.

Schmid, D. W., and Y. Y. Podladchikov (2003), Analytical solutions for deformable elliptical inclusions in general shear, Geophysical Journal International, 155, 269-288.

Scott, T., and D. Kohlstedt (2006), The effect of large melt fraction on the deformation behavior of peridotite, Earth and Planetary Science Letters, 246(3-4), 177-187.

Shelly, D. R., G. C. Beroza, and S. Ide (2007), Non-volcanic tremor and low-frequency earthquake swarms, Nature, 446(7133), 305-307.

Simpson, G., and M. Spiegelman (2011), Solitary wave benchmarks in magma dynamics, Journal of Scientific Computing, 49, 268-290.

1272 Spiegelman, M. (2003), Linear analysis of melt band formation by simple shear,
1273 Geochemistry, Geophysics, Geosystems, 4(9).

1274 Steeb, H., and J. Renner (2019), Mechanics of poro-elastic media: a review with emphasis on
1275 foundational state variables, Transport in Porous Media, 130, 437-461.

1276 Stevenson, D. J. (1989), Spontaneous small-scale melt segregation in partial melts undergoing
1277 deformation, Geophysical Research Letters, 16(9), 1067-1070.

1278 Sulem, J., and V. Famin (2009), Thermal decomposition of carbonates in fault zones: Slip-
1279 weakening and temperature-limiting effects, Journal of Geophysical Research: Solid Earth,
1280 114(B3).

1281 Taetz, S., T. John, M. Brocker, C. Spandler, and A. Stracke (2018), Fast intraslab fluid-flow
1282 events linked to pulses of high pore fluid pressure at the subducted plate interface, Earth and
1283 Planetary Science Letters, 482, 33-43, doi:10.1016/j.epsl.2017.10.044.

1284 Tarling, M. S., S. A. F. Smith, and J. M. Scott (2019), Fluid overpressure from chemical
1285 reactions in serpentinite within the source region of deep episodic tremor, Nature Geoscience,
1286 12(12), 1034-1042, doi:10.1038/s41561-019-0470-z.

1287 Tsenn, M. C., and N. L. Carter (1987), Upper limits of power law creep of rocks,
1288 Tectonophysics, 136(1-2), 1-26.

1289 Ulmer, P., and V. Trommsdorff (1995), Serpentine Stability to Mantle Depths and
1290 Subduction-Related Magmatism, Science, 268(5212), 858-861,
1291 doi:doi:10.1126/science.268.5212.858.

1292 Van Avendonk, H. J. A., W. S. Holbrook, D. Lizarralde, M. M. Mora, S. Harder, A. D.
1293 Bullock, G. E. Alvarado, and C. J. Ramirez (2010), Seismic evidence for fluids in fault zones

on top of the subducting Cocos Plate beneath Costa Rica, Geophysical Journal International, 181(2), 997-1016, doi:10.1111/j.1365-246X.2010.04552.x.

Virieux, J. (1986), P-SV wave propagation in heterogeneous media: Velocity-stress finite-difference method, Geophysics, 51(4), 889-901.

Wang, L. H., V. M. Yarushina, Y. Alkhimenkov, and Y. Podladchikov (2021), Physics-inspired pseudo-transient method and its application in modelling focused fluid flow with geological complexity, Geophysical Journal International, 229(1), 1-20, doi:10.1093/gji/ggab426.

Yarushina, V. M., and Y. Y. Podladchikov (2015), (De) compaction of porous viscoelastoplastic media: Model formulation, Journal of Geophysical Research: Solid Earth, 120(6), 4146-4170.

Figures with captions

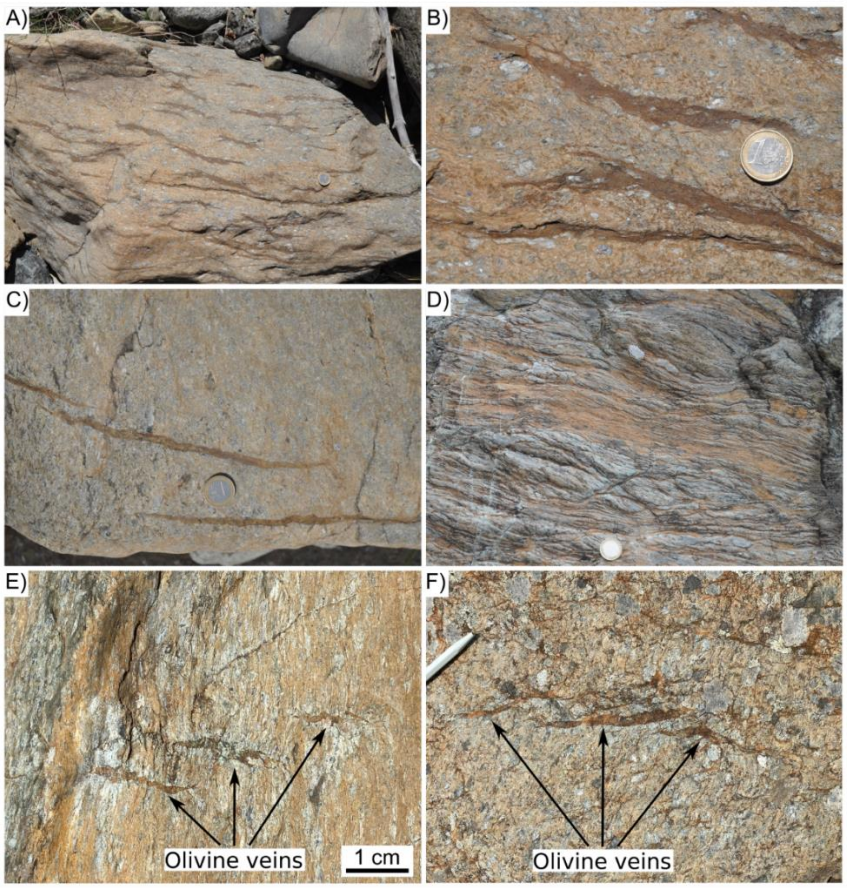

Figure 1. Natural examples of metamorphic olivine veins in antigorite serpentinite from the Erro Tobbio ultramafic rocks, Ligurian Alps, Italy. A) Overview on the limited spatial extent of olivine bearing veins (with darker color) in weakly deformed serpentinized peridotite. Coin diameter is 2.4 cm. B) Olivine veins with characteristic spacing and aspect ratios in serpentinised peridotite. Detail of picture in A). C) olivine-bearing veins in a serpentinised peridotite, foliation is sub vertical, extent of veins is ca. 20 cm. D) Serpentinite mylonite with different generations of olivine veins. An earlier set is subparallel to the foliation, younger shear bands dissect serpentinite mylonite and olivine veins. Top-to-the-left shear sense. Note the late stage serpentine veins perpendicular to the foliation. E) and F) En échelon olivine veins in antigorite serpentinite. Coordinates: A) and B) at 44.56081°N, 8.81376°E; C) at 44.57147°N, 8.80825°E; D) at 44.56958°N, 8.80814°E; E) and F) at 44.57140°N, 8.80784°E.

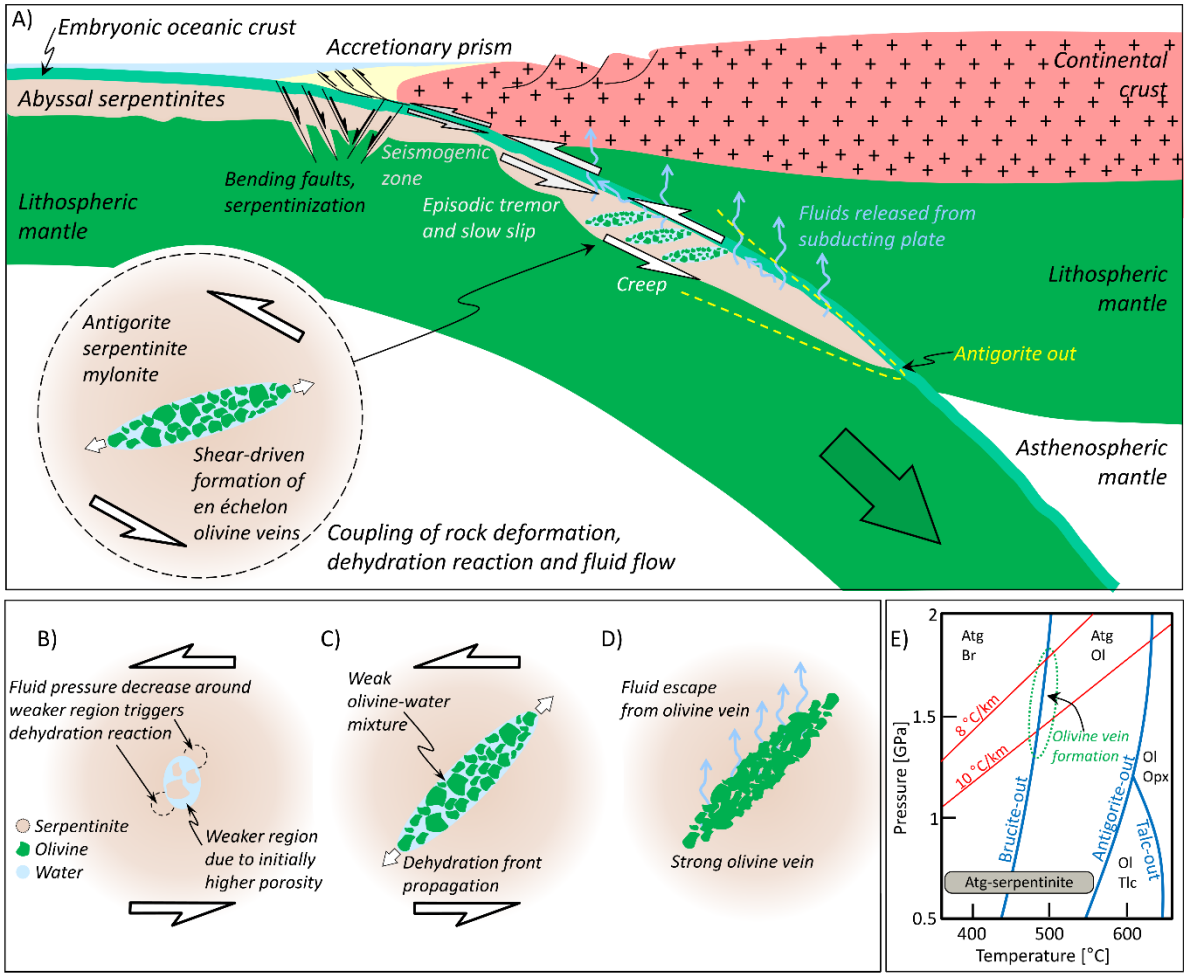

Figure 2. Simple sketches illustrating the geodynamic setting (A) and the hypothesis for shear-driven dehydration and olivine vein formation in viscous serpentinite (B to D; see text for details). E) Simplified phase diagram showing the Brucite-out and Antigorite-out reactions, two common subduction geotherms (in °C/km), the likely region of olivine vein formation (green dashed ellipse) and typical minerals. The phase diagram is strongly simplified for a MSH system after figure 6 in Padrón-Navarta et al. (2013). Mineral abbreviations: Atg = antigorite, Br = brucite, Ol = olivine, Opx = orthopyroxene and Tlc = talc.

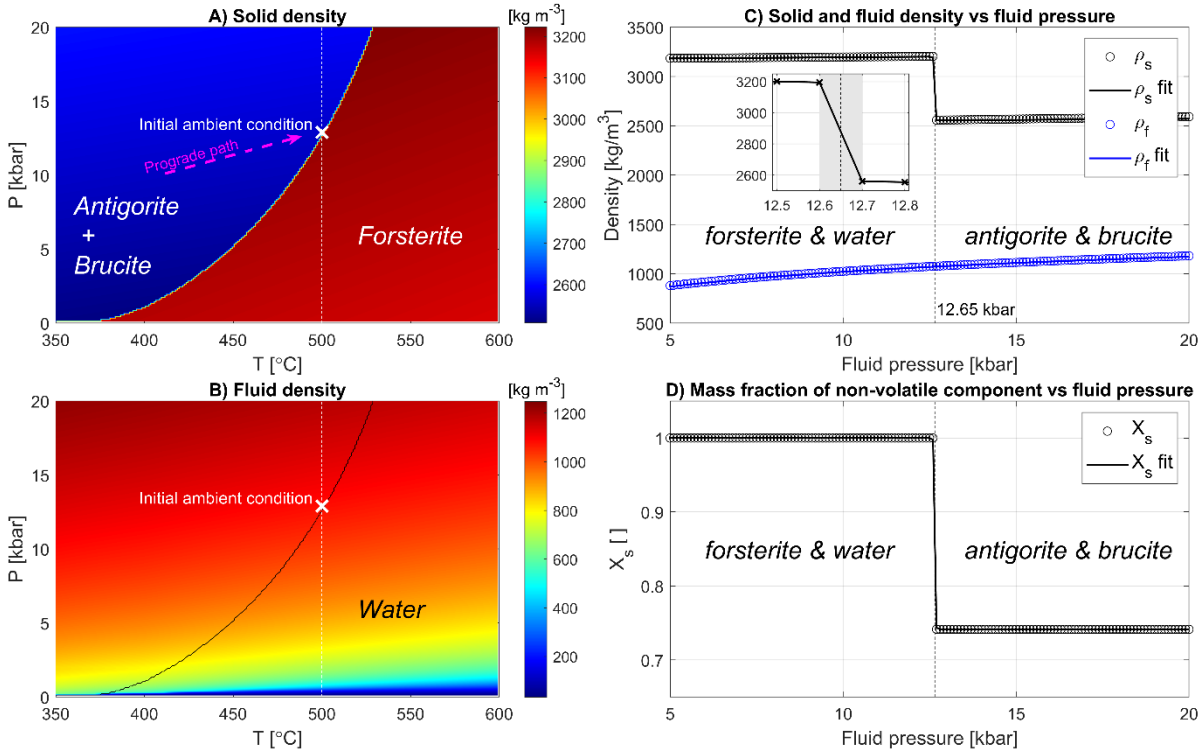

Figure 3. Thermodynamic results obtained from Gibbs' free energy minimization for the system antigorite + brucite = forsterite + water (see text for exact chemical formulas). Density fields of solid (A) and fluid (B) in thermodynamic pressure, P, and temperature, T, space. Corresponding profiles of solid and fluid densities (C) and mass fraction of MgO (D) as a function of fluid pressure at 500 °C. The circles in the three profiles in panels C) and D) are the results from Gibbs energy minimization and the corresponding solid lines are analytical approximations of these profiles, which are used in the numerical algorithm (see Appendix).

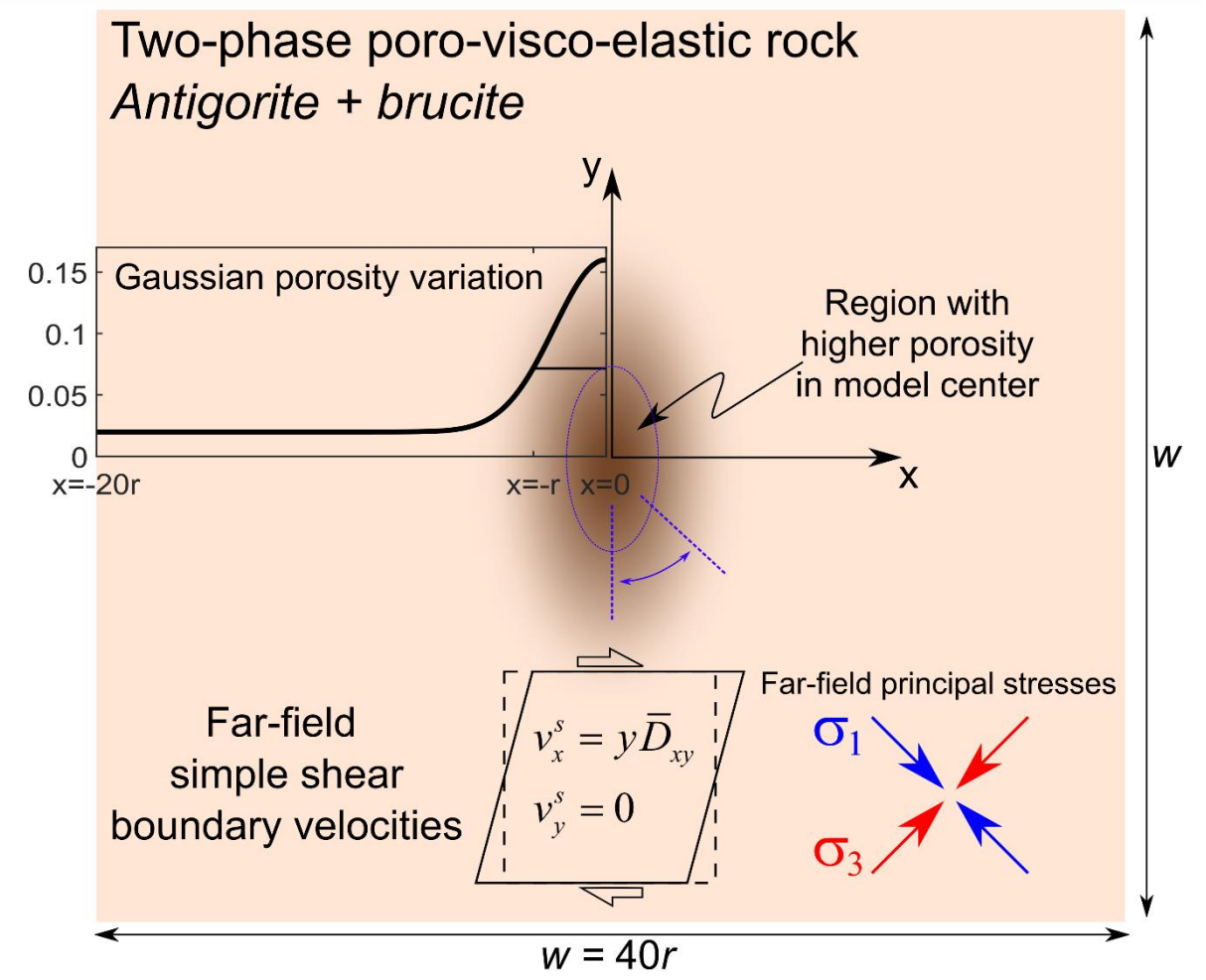

1341

1342 Figure 4. Sketch of the model configuration and the applied far-field simple shear (bottom
1343 sketch; see text for details). The intitial distribution of the porosity is described by a 2D
1344 Gaussian distribution, having an initial horizontal bandwidth of $2\,r$ (graph in left middle of
1345 the sketch) and a vertical bandwidth of $4\,r$. The width and height of the model is $40\,r$ and the
1346 applied far-field shearing rate is $\bar{D}_{xy}$. The orientation of the maximal and minimal principal
1347 stresses, σ_1 and σ_3 respectively, associated to the far-field simple shearing are indicated in
1348 the bottom right.

1349

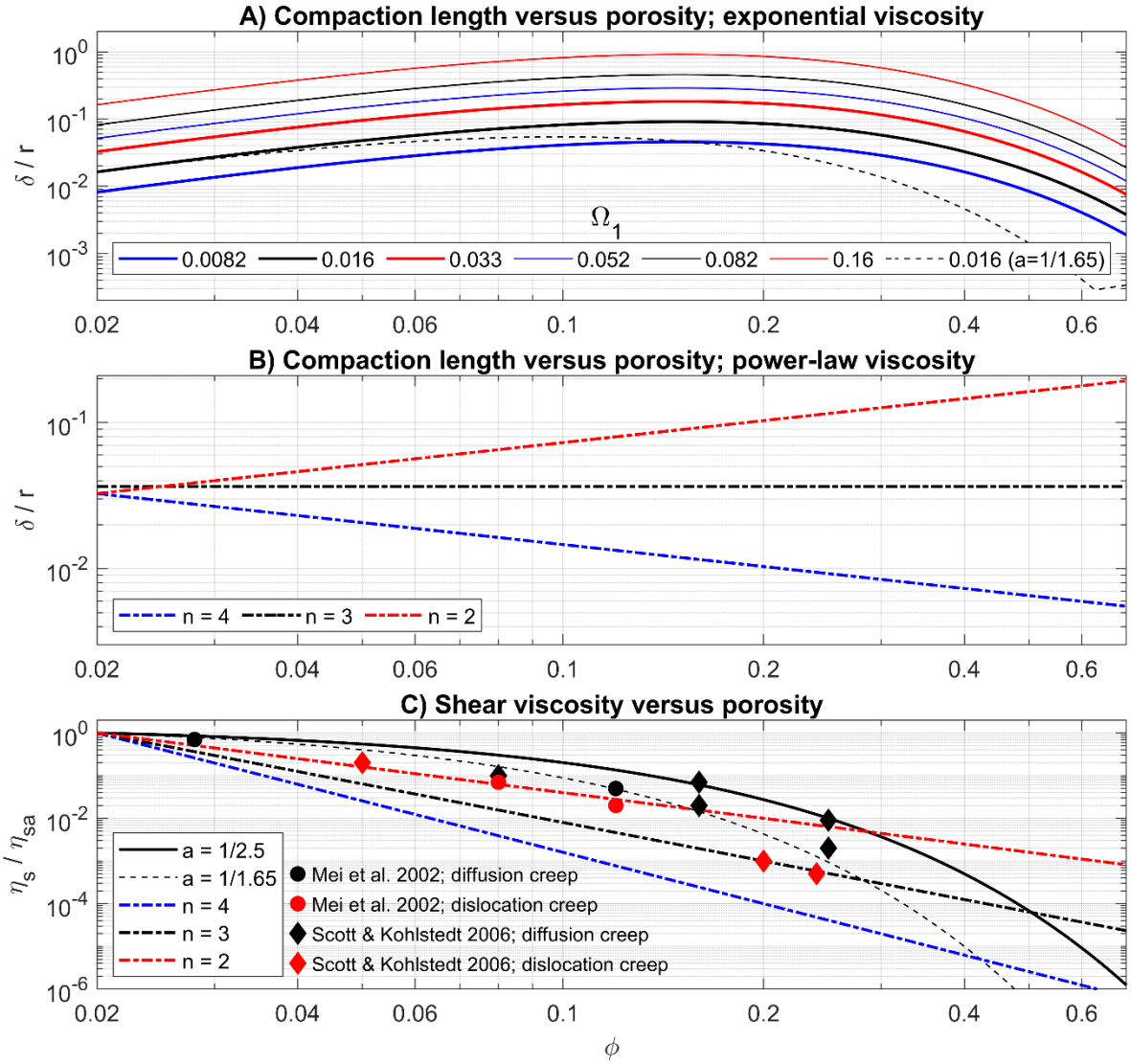

Figure 5. The relations between normalized compaction length, δ / r, and porosity, ϕ, applied in the simulations. A) Curves of δ / r versus ϕ for shear viscosities, η_s, that are an exponential function of ϕ. The parameter a is always 1/2.5, except for one curve with a = 1/1.65 (see equation (10)). B) Curves of δ / r versus ϕ for η_s that are a power-law function of ϕ. The applied power-law exponents, n, are indicated in the legend (see equation (11)). C) Applied values of η_s, normalized by the shear viscosity for the ambient porosity, η_{sa}, versus ϕ. Diamonds and circles indicate representative experimental data for the shear viscosities of partially molten rocks (data taken from the compilation in Katz et al., 2022, their figure 2b, with original references given in the legend).

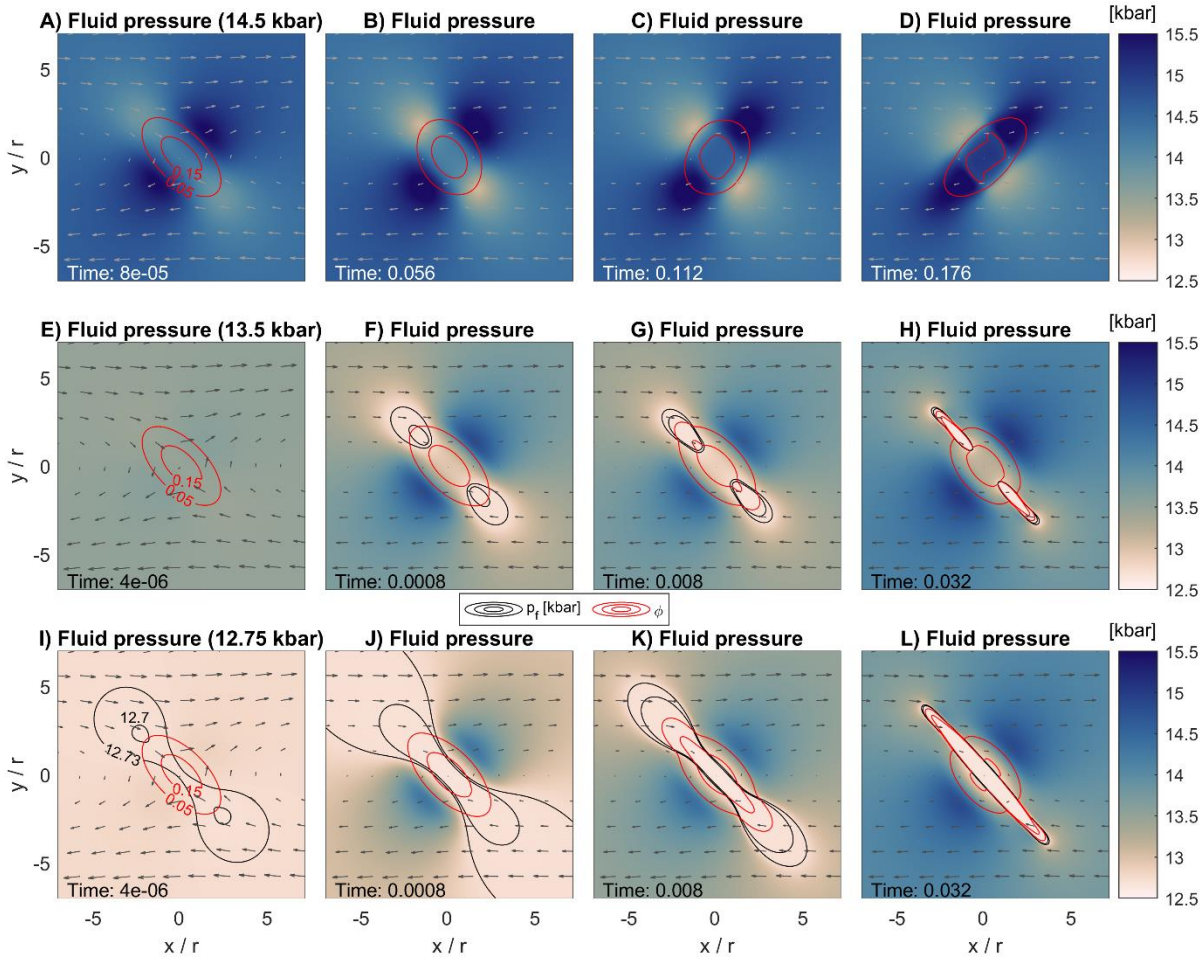

Figure 6. Color plots showing the evolution of fluid pressure, p_f, with progressive simple shearing for three values of the ambient pressure, p_a. Time displayed in panels is dimensionless and normalized by t_C for the ambient porosity (eqn. (15)). Panels A) to D) show results for p_a of 14.5 kbar, E) to H) for p_a of 13.5 kbar and I) to L) for p_a of 12.75 kbar. Red contours indicate porosity, ϕ, and black contours p_f (contour labels given in panel I). For better comparison, the color scale is the same for all panels. Applied parameters in the simulations: $\Omega_1 = 0.033$, $\Omega_2 = 0.11$, $\Omega_3 = 40$, $\Omega_4 = 2$ and $\Omega_5 = 0.0025$.

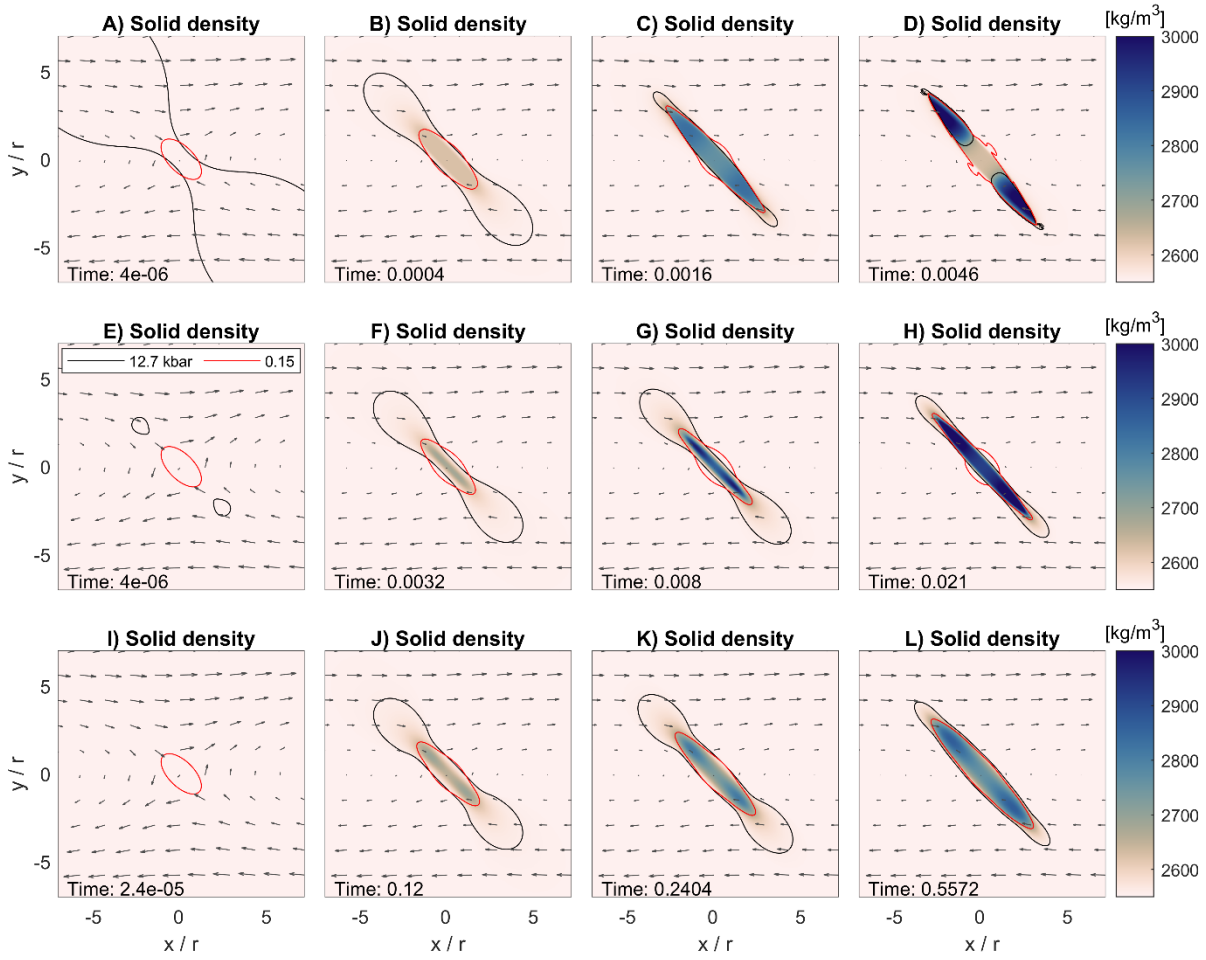

1370

1371 Figure 7. Color plots showing the evolution of solid density, ρ_s, with progressive simple

1372 shearing for three values of Ω_1 and for a shear viscosity with exponential dependence on

1373 porosity (Fig. 5A). Time displayed in panels is dimensionless and normalized by t_C for the

1374 ambient porosity (eqn. (15)). Ambient pressure is always 12.75 kbar. Panels A) to D) show

1375 results for $\Omega_1 = 0.0082$, E) to H) for $\Omega_1 = 0.033$ and I) to L) for $\Omega_1 = 0.16$ (see Fig. 5A). Red

1376 contours indicate porosity, ϕ, of 0.15 and black contours indicate fluid pressure, p_f, at 12.7

1377 kbar (contour labels given in panel E). Applied parameters in the simulations: $\Omega_2 = 0.11$,

1378 $\Omega_3 = 40$, $\Omega_4 = 2$ and $\Omega_5 = 0.0025$.

1379

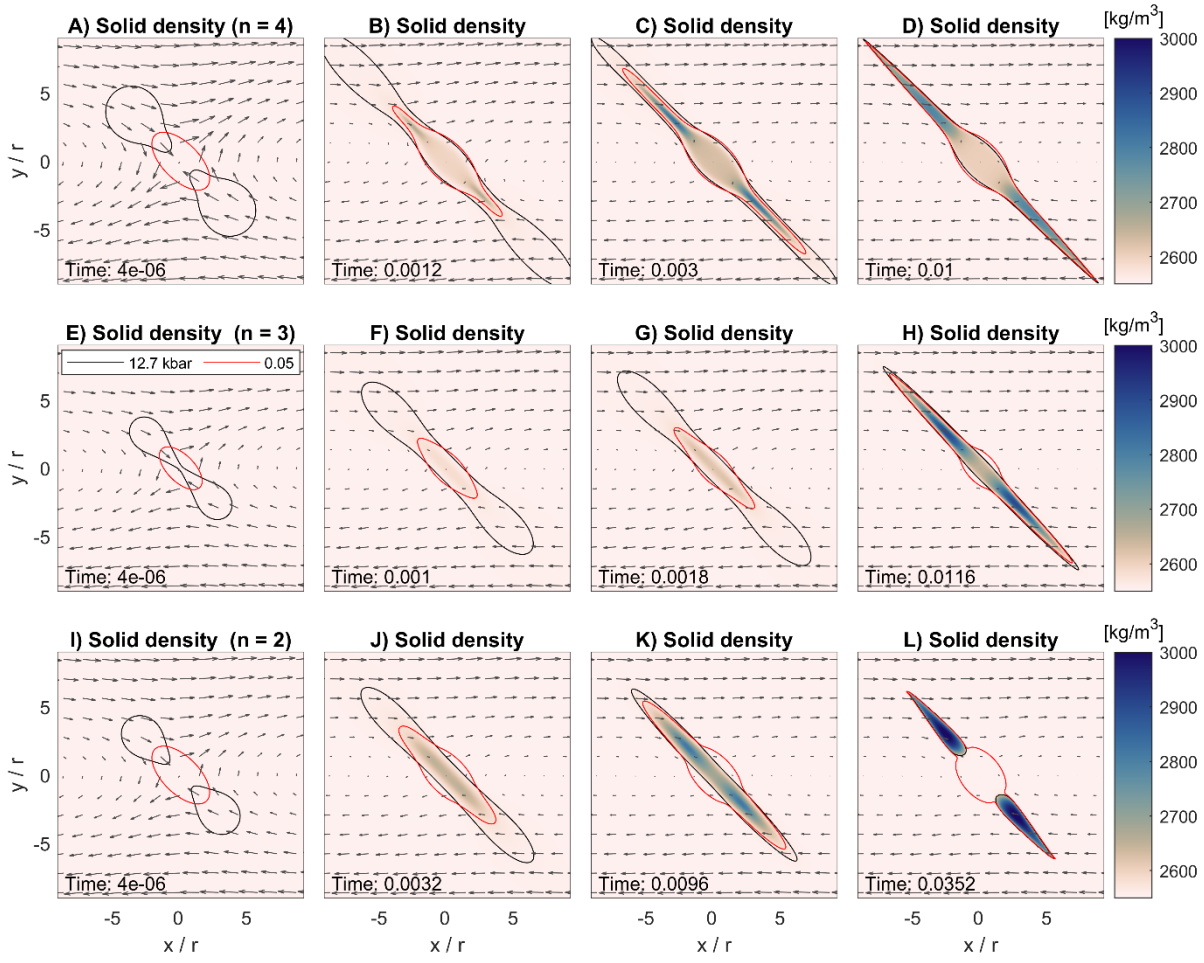

1380

1381 Figure 8. Color plots showing the evolution of solid density, ρ_s, with progressive simple

1382 shearing for a shear viscosity with power-law dependence on porosity (Fig. 5B). The three

1383 δ / r versus ϕ relations displayed in figure 5B are applied in the displayed three simulations.

1384 Time displayed in panels is dimensionless and normalized by t_C for the ambient porosity

1385 (eqn. (15)). Ambient pressure is always 12.75 kbar. Panels A) to D) show results for $n = 4$, E)

1386 to H) for $n = 3$ and I) to L) for $n = 2$ (see Fig. 5B). Red contours indicate porosity, ϕ, of 0.05

1387 and black contours indicate fluid pressure, p_f, at 12.7 kbar (contour labels given in panel E).

1388 Applied parameters in the simulations: $\Omega_2 = 0.11$, $\Omega_3 = 40$, $\Omega_4 = 2$ and $\Omega_5 = 0.0025$.

1389

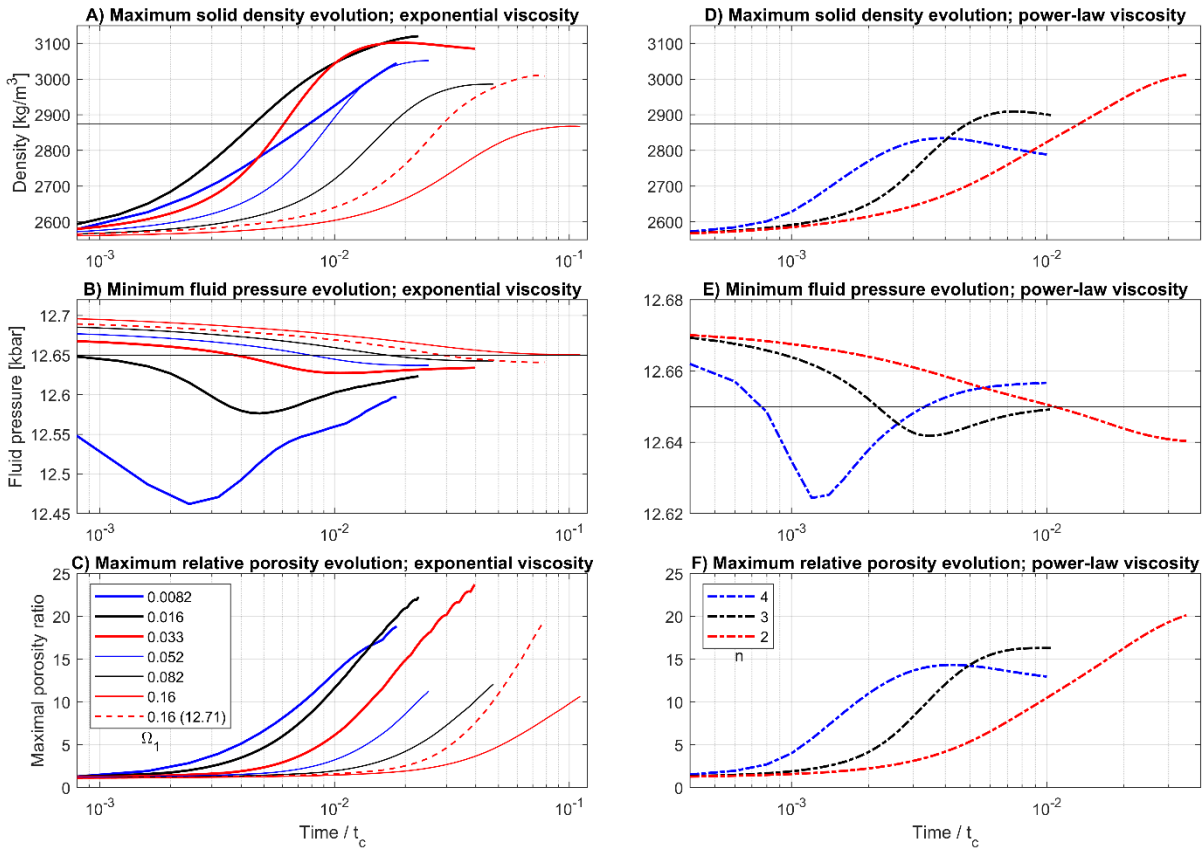

1390

1391 Figure 9. Time evolution of maximum solid density (A and D), minimum fluid pressure (B
1392 and E), and maximum relative porosity increase (C and F). The porosity ratio is the ratio of
1393 the current to the initial porosity at a numerical grid point and the maximal porosity ratio
1394 displays the maximal value for each numerical time step. Time displayed in panels is
1395 dimensionless and normalized by t_C for the ambient porosity (eqn. (15)). A) to C) shows
1396 results for simulations with the δ / r versus ϕ relations displayed in figure 5A and D) to F)
1397 shows results for simulations with the δ / r versus ϕ relations displayed in figure 5B. Legend
1398 in C) applies also to panels A) and B) nd legend in F) applies also to panels D) and E).

1399

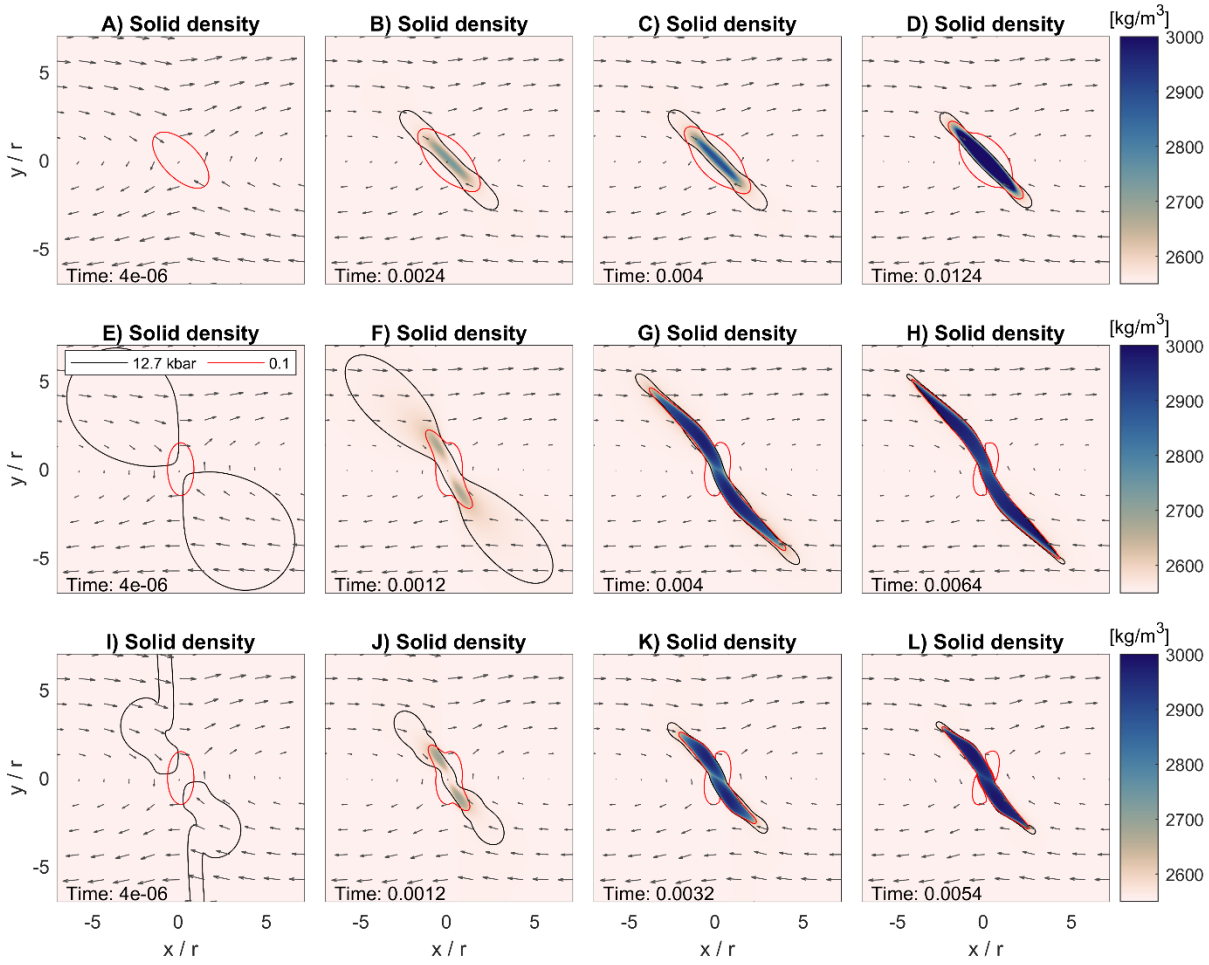

1400

1401 Figure 10. Color plots showing the evolution of solid density, ρ_s, with progressive simple

1402 shearing for three simulations for a shear viscosity with exponential dependence on porosity

1403 (Fig. 5A). A) to D) shows the simulation displayed in figure 7E to H but with a yield stress of

1404 100 MPa. E) to H) shows a simulation for an initial distribution of porosity with a vertical

1405 long axis of the Gaussian distribution (see vertical blue dashed line in Fig. 4). The parameter

1406 a = 1/1.65 (see Fig. 5A and C). I) to L) shows the simulation displayed in E) to H) with an

1407 applied yield stress of 125 MPa. Time displayed in panels is dimensionless and normalized by

1408 t_C for the ambient porosity (eqn. (15)).

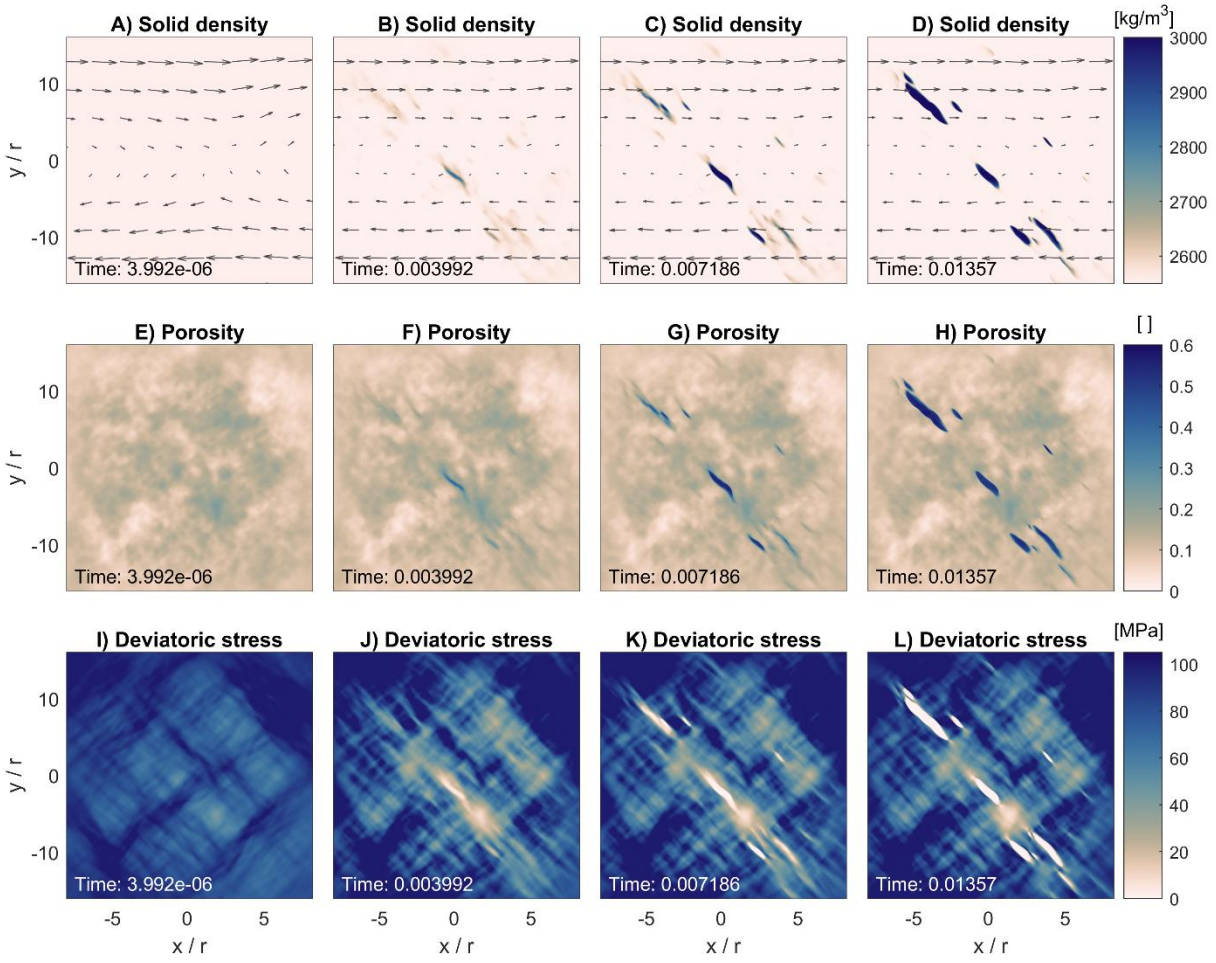

1411 Figure 11. Results for a simulation with an initial random porosity distribution and a yield
1412 stress of 100 MPa. A) to D) shows time evolution of solid density, E) to H) of porosity and I)
1413 to L) of the square root of the second invariant of the deviatoric stress tensor,
1414 $\tau_{II} = \sqrt{0.5\left(\tau_{xx}^2 + \tau_{yy}^2\right) + \tau_{xy}^2}$. Time displayed in panels is dimensionless and normalized by t_C
1415 for the ambient porosity (eqn. (15)). Exponential porosity dependence of shear viscosity with
1416 a = 1/2.5 (Fig. 5C). Applied parameters in the simulations: $\Omega_1 = 0.036$, $\Omega_2 = 0.39$, $\Omega_4 = 2$
1417 and $\Omega_5 = 0.0025$.

1418

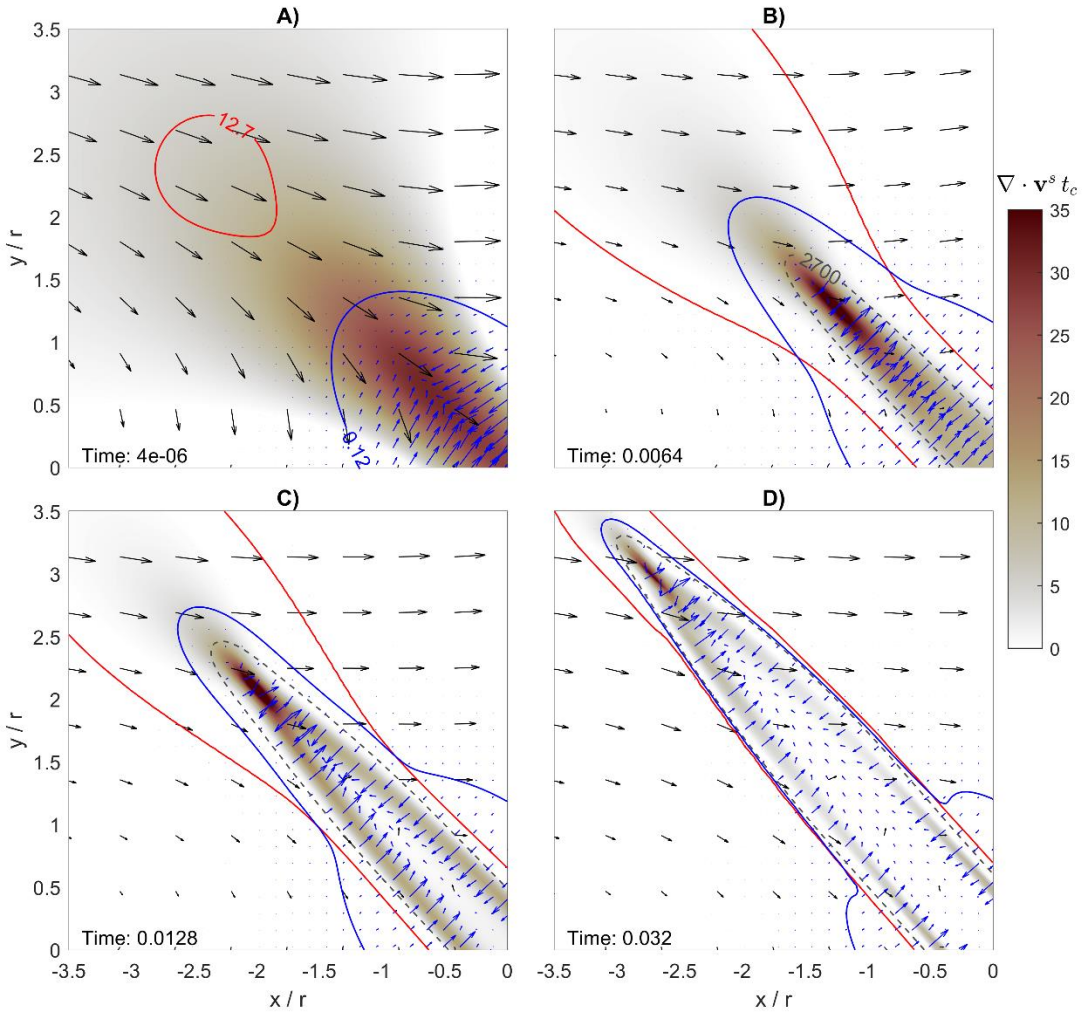

Figure 12. Evolution of a dehydration vein for the simulation shown in figure 7E to H. Time displayed in panels is dimensionless and normalized by t_C for the ambient porosity (eqn. (15)). The colormaps show the dimensionless divergence of the solid velocity, the blue arrows show the fluid velocity field and the black arrows show the solid velocity field. The red contour indicates fluid pressure, p_f = 12.7 kbar, whereby values of p_f are always smaller inside the contour. The blue contour indicates porosity, ϕ = 0.12, whereby values of ϕ are always larger inside the contour. The dashed grey contour indicates solid density ρ_s = 2700 kg/m^3, whereby values of ρ_s are always larger inside the contour. There are no solid density contours in panel A) because all densities are < 2700 kg/m^3.

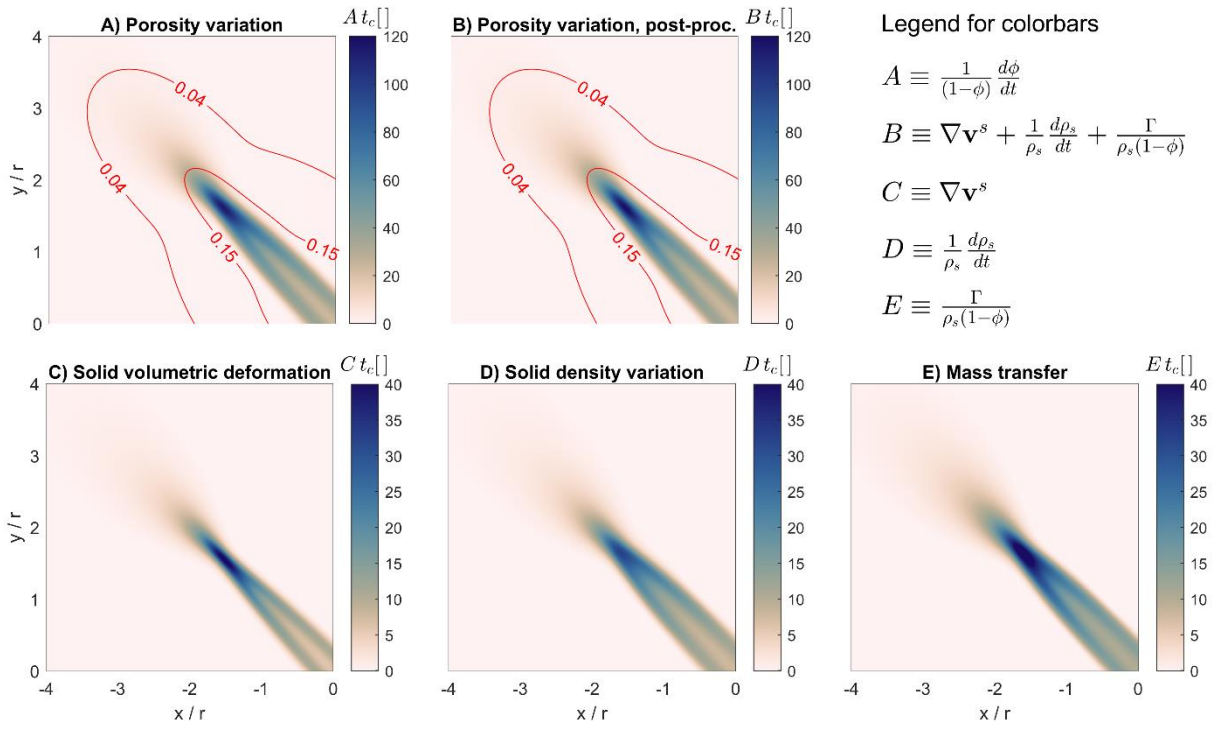

Figure 13. The three mechanisms that control the temporal porosity variation (see equation (19)) for the simulation shown in figure 7E to H at a dimensionless time of 0.008. Panel A) shows the colormap of the quantity displayed in the legend for A, which represents the porosity rate, B) shows the colormap of the quantity displayed in the legend for B, C) shows the colormap of the quantity displayed in the legend for C, which represents the rate of solid volumetric deformation, D) shows the colormap of the quantity displayed in the legend for D, which represents the rate of solid density variation, and E) shows the colormap of the quantity displayed in the legend for E, which represents the rate of mass transfer. All displayed terms represent dimensionless rates which are normalized by t_C for the ambient porosity (eqn. (15)). Symbols are explained in Table 1.

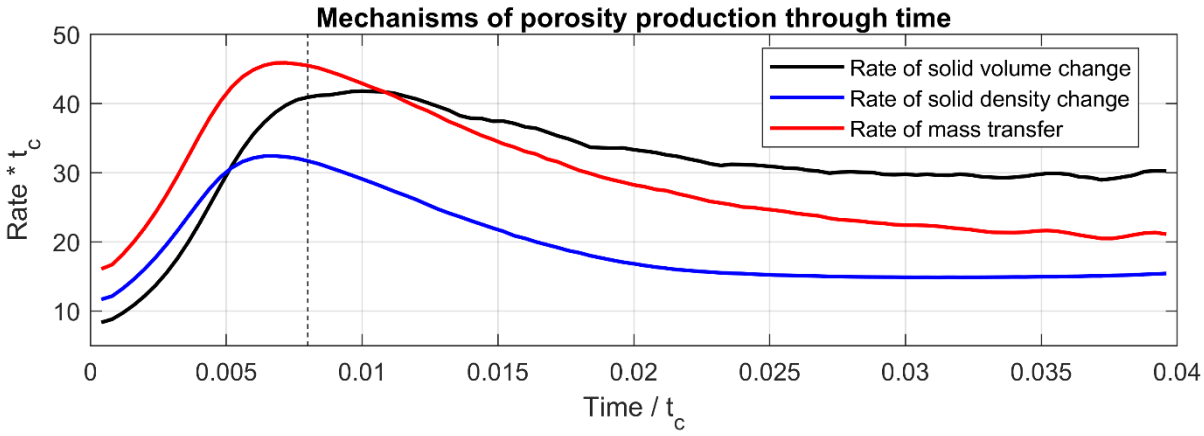

1444

1445 Figure 14. Time evolution of the maximum (per each time step) values of the rate of solid
1446 volume change (quantity labelled C in Fig. 13), rate of solid density change (quantity labelled
1447 D in Fig. 13) and rate of mass transfer (quantity labelled E in Fig. 13). Time is dimensionless
1448 and normalized by t_C for the ambient porosity (eqn. (15)). The vertical dashed line indicates
1449 the time for which results are displayed in figure 13.

1450

1451

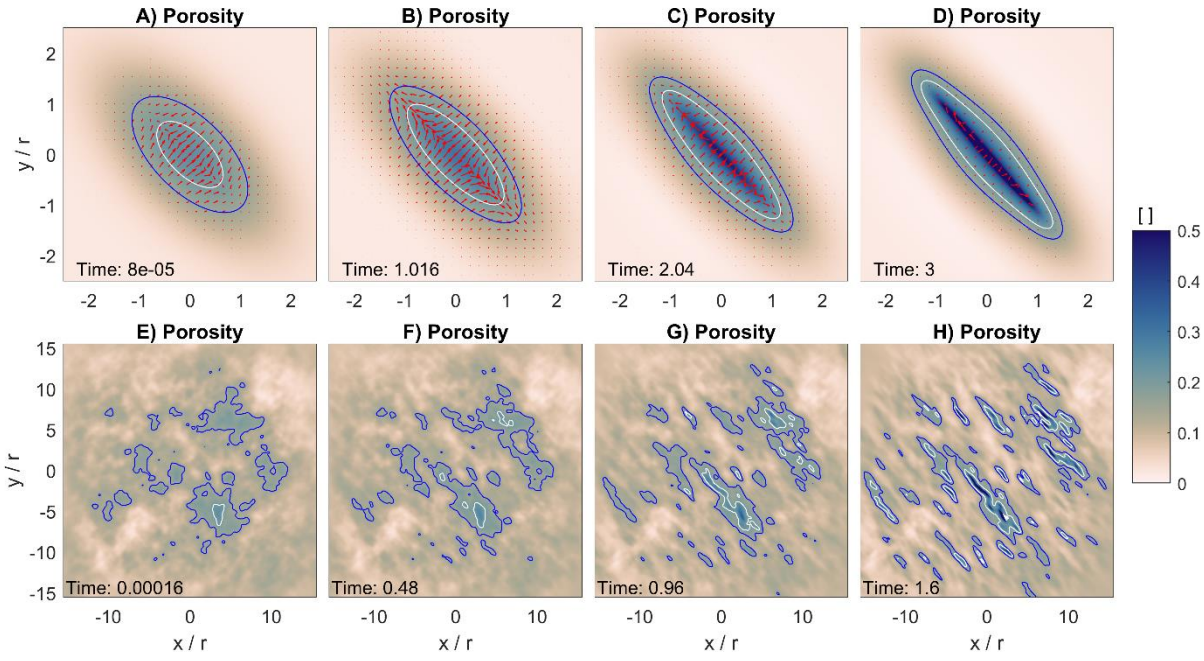

Figure 15. Colorplots of porosity, ϕ, show the formation of localized, high-porosity fluid bands without dehydration reaction. In all panels, time is dimensionless and normalized by t_C, blue contours indicate ϕ = 0.15 and white contours indicate small viscosities for η_s / η_{sa} = 1/40. A) to D) shows colorplots of ϕ for the simulation presented in figure 6A to D, but with Ω_1 = 0.33. Red arrowas indicate fluid velocity. E) to H) shows the simulation shown in figure 11, but for p_a = 14.5 kbar and Ω_1 = 0.33. The total area within white contour lines is increasing, indicating and effective weakening of the model domain due to the increase in areas with η_s / η_{sa} < 1/40. Regions with high ϕ become elongated and parallel to the orientation of σ_1 (see Fig. 4).

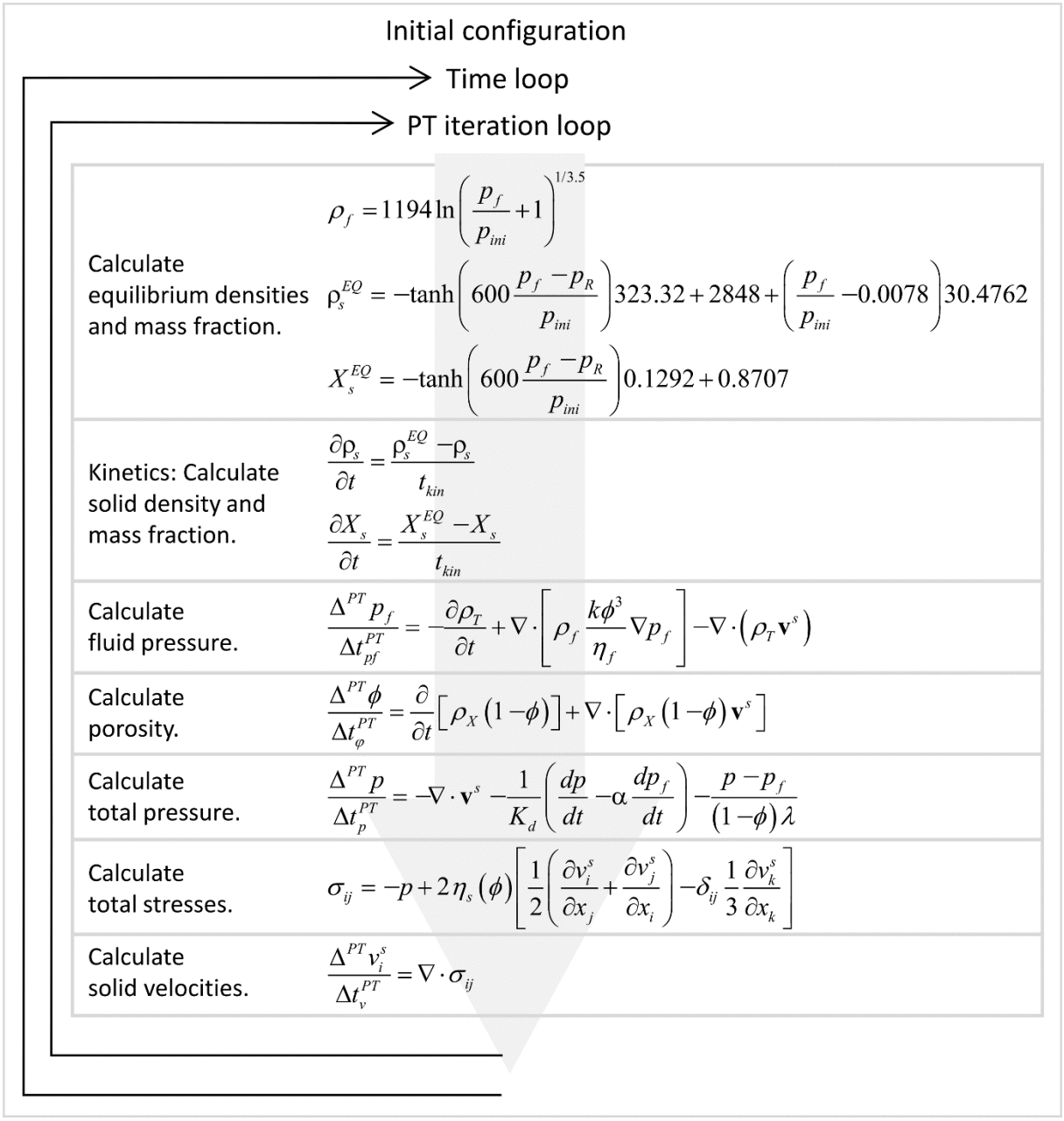

Figure A1. Simplifed flow chart of the applied numerical algorithm and the order of the governing equations in which they are solved inside the pseudo-transient (PT) iteration loop. The PT iteration loop calculates the unknowns and simultaneously treats the various nonlinearites, such as porosity-dependent shear viscosity and permeability, while the time loop calculates the evolution of the unknows with time. Parameters are explained in Table 1.

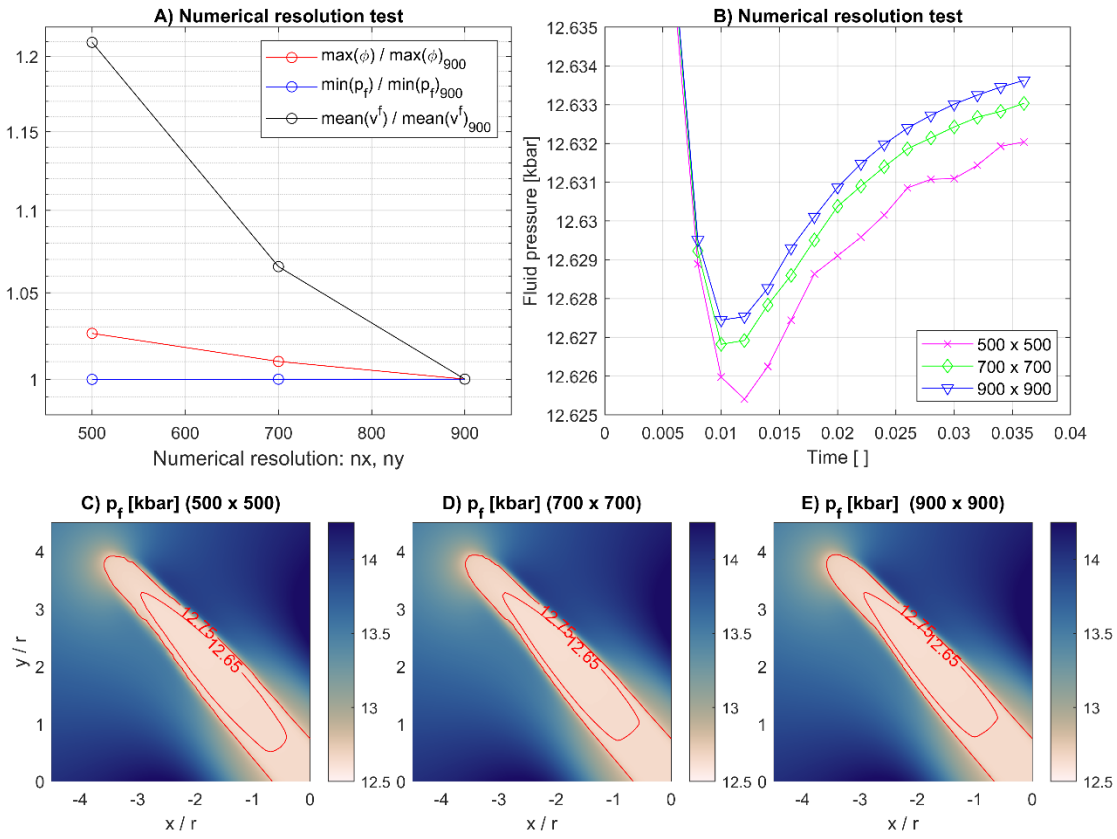

Figure A2. Numerical resolution test for the simulation shown in figure 7E to H . A) For a dimensionless model time of 1.21, the ratio of the maximum porosity in the model domain divided by the maximum porosity for a simulation with a resolution of 900 × 900 grid points is plotted versus the corresponding resolution for simulations with different resolution. Similar ratios are plotted for the minimum fluid pressure in the model domain and the mean value of the fluid velocity. The larger the resolution, the less the three ratios vary. B) Evolution of minimum fluid pressure in the model domain with time for different numerical resolutions (see legend). With larger resolution, the evolution of fluid pressure varies less. C) to D) At a dimensionless model time of 0.036, the colormap of the fluid pressure is displayed for three different resolutions (see numbers in panel titles). Two contour lines of fluid pressure are displayed for better comparability. A resolution of 900×900 was applied in the simulations presented in the main text.

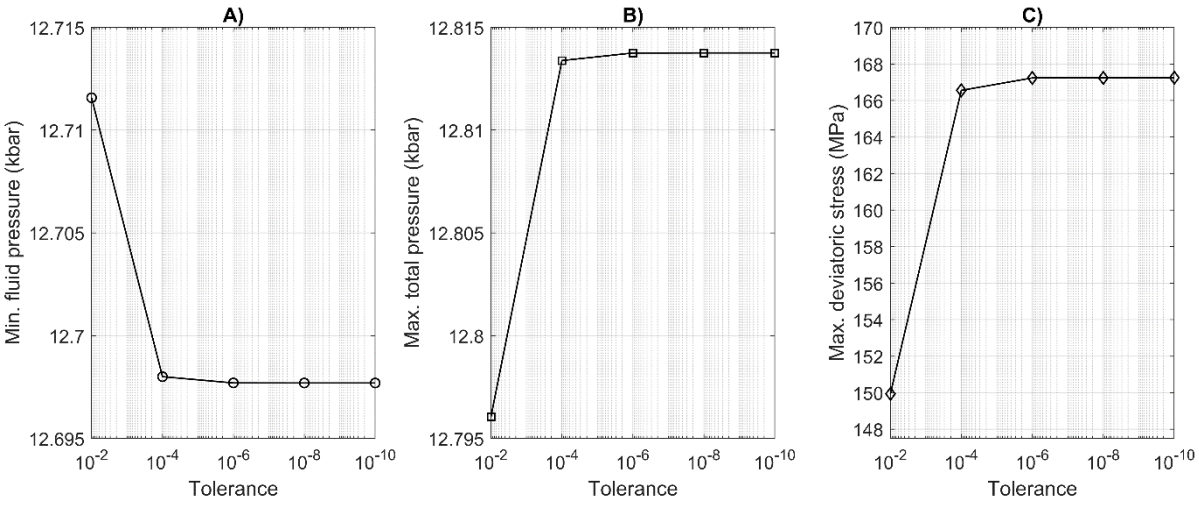

Figure A3. Numerical accuracy test for the simulation shown in figure 7E to H after the first numerical time step. A) The minimum value of the fluid pressure in the model domain versus the applied tolerance of the iterative Pseudo-Transient solver. B) Maximum value of total pressure versus tolerance. C) Maximum value of second invariant of deviatorc stress tensor versus tolerance. Once the tolerance is smaller than 10^{-6} the three numerical values do not change anymore. A tolerance of 10^{-6} was used in the presented simulations.

Table 1. Model variables and parameters.

Symbol	Name / Definition	Units
t_c	Characterstic time	$[s]$
t_{kin}	Kinetic time	$[s]$
δ	Compaction length	$[m]$
p_f	Fluid pressure	$[Pa]$
p	Total pressure	$[Pa]$
p_a	Ambient pressure	$[Pa]$
ϕ	Porosity	$[\ ]$
ϕ_a, ϕ_0	Ambient, initial porosity	$[\ ]$
ρ_s	Solid density	$\left[kg \cdot m^{-3}\right]$
ρ_f	Fluid density	$\left[kg \cdot m^{-3}\right]$
X_s	Mass fraction MgO	$[\ ]$
Γ	Mass transfer rate	$\left[kg \cdot m^{-3} \cdot s^{-1}\right]$
$v_x^s,\ v_y^s$	Solid velocities	$\left[m \cdot s^{-1}\right]$
$v_x^f,\ v_y^f$	Fluid velocities	$\left[m \cdot s^{-1}\right]$
$\tau_{xx}, \tau_{yy}, \tau_{xy}$	Deviatoric stresses	$[Pa]$
τ_{II}	Deviatoric stress invariant	$[Pa]$
k	Permeability	$\left[m^2\right]$
η_f	Fluid viscosity	$[Pa \cdot s]$
η_s	Shear viscosity solid	$[Pa \cdot s]$
λ	Bulk viscosity solid	$[Pa \cdot s]$
K_s	Bulk modulus solid	$[Pa]$
K_d	Bulk modulus drained	$[Pa]$
$\bar{D}_{xy}$	Far-field shearing rate	$\left[s^{-1}\right]$
r	Bandwidth of Gaussian	$[m]$
w	Model width	$[m]$
$\Omega_{1,2,3,4,5}$	Dimensionless ratios	$[\ ]$

Figure1.

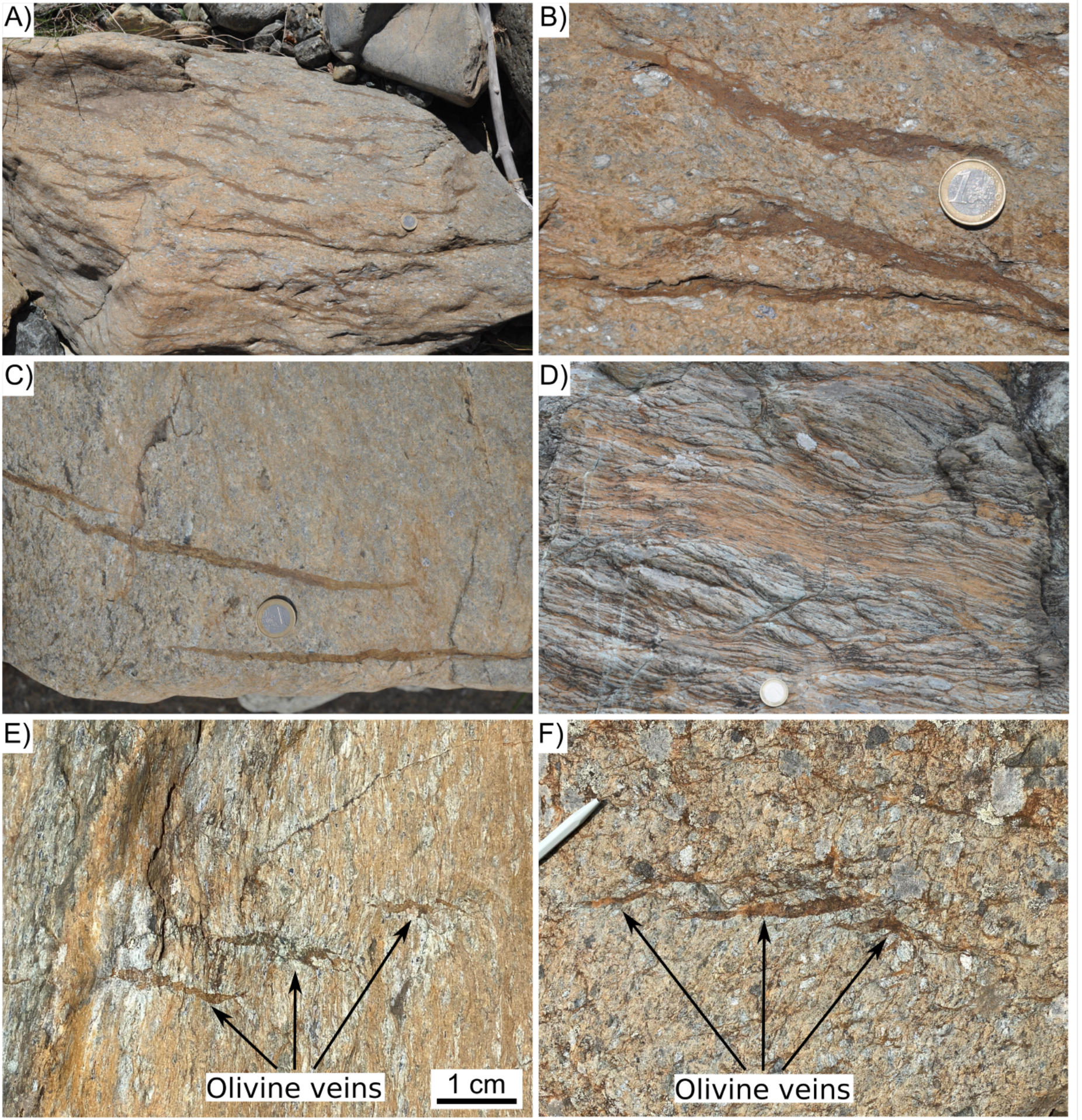
A)
B)
C)
D)
E)
Olivine veins
1 cm
F)
Olivine veins

Figure2.

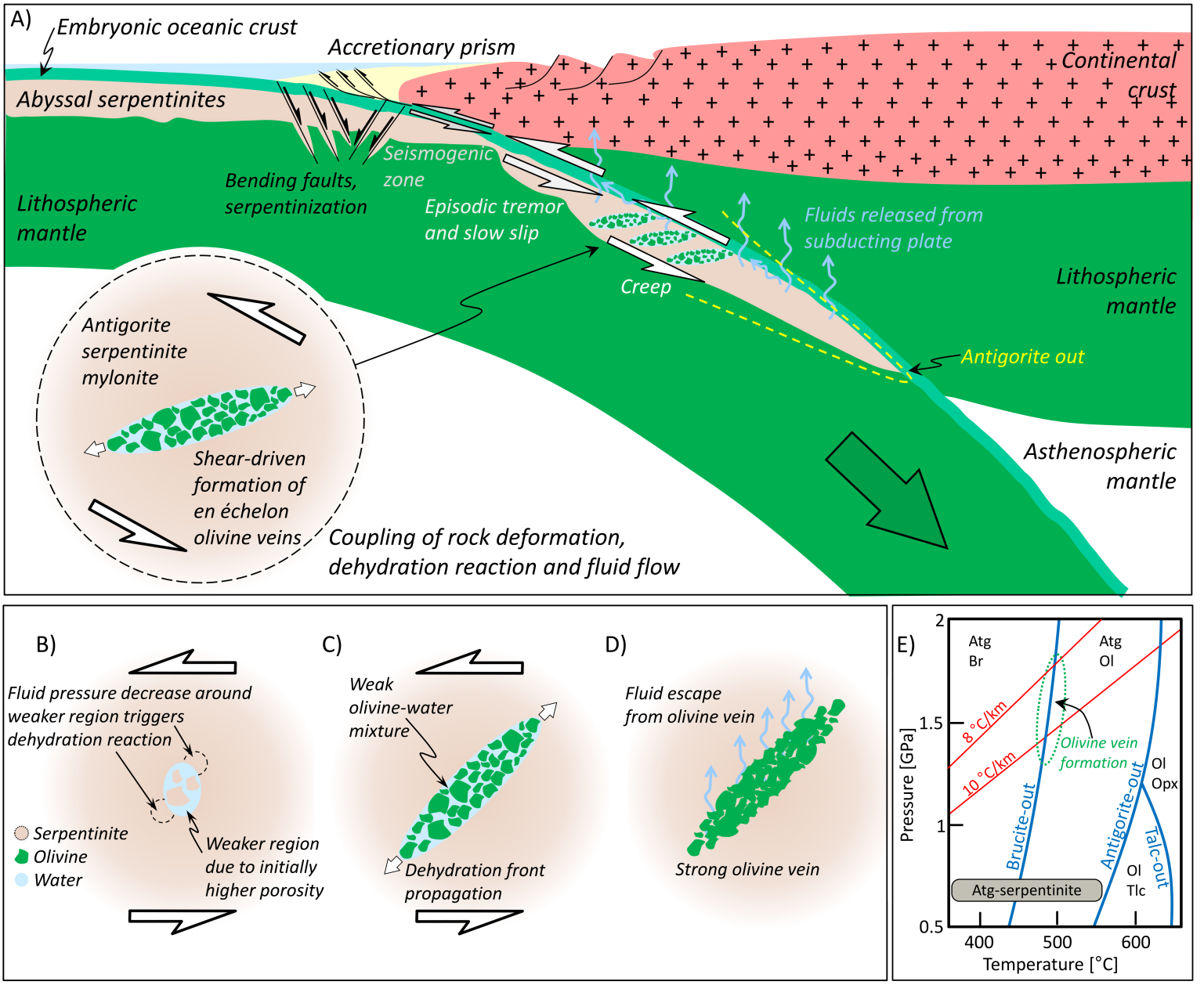
A)
Embryonic oceanic crust
Accretionary prism
Continental crust
Abyssal serpentinites
Seismogenic zone
Bending faults, serpentinization
Episodic tremor and slow slip
Fluids released from subducting plate
Lithospheric mantle
Creep
Lithospheric mantle
Antigorite out
Antigorite serpentinite mylonite
Shear-driven formation of en échelon olivine veins
Asthenospheric mantle
Coupling of rock deformation, dehydration reaction and fluid flow
B)
Fluid pressure decrease around weaker region triggers dehydration reaction
Serpentinite
Olivine
Water
Weaker region due to initially higher porosity
C)
Weak olivine-water mixture
Dehydration front propagation
D)
Fluid escape from olivine vein
Strong olivine vein
E)
Atg Br
Atg Ol
8 °C/km
10 °C/km
Olivine vein formation
Ol Opx
Brucite-out
Antigorite-out
Talc-out
Ol Tlc
Atg-serpentinite
Pressure [GPa]
Temperature [°C]
2
1.5
1
0.5
400
500
600

Figure3.

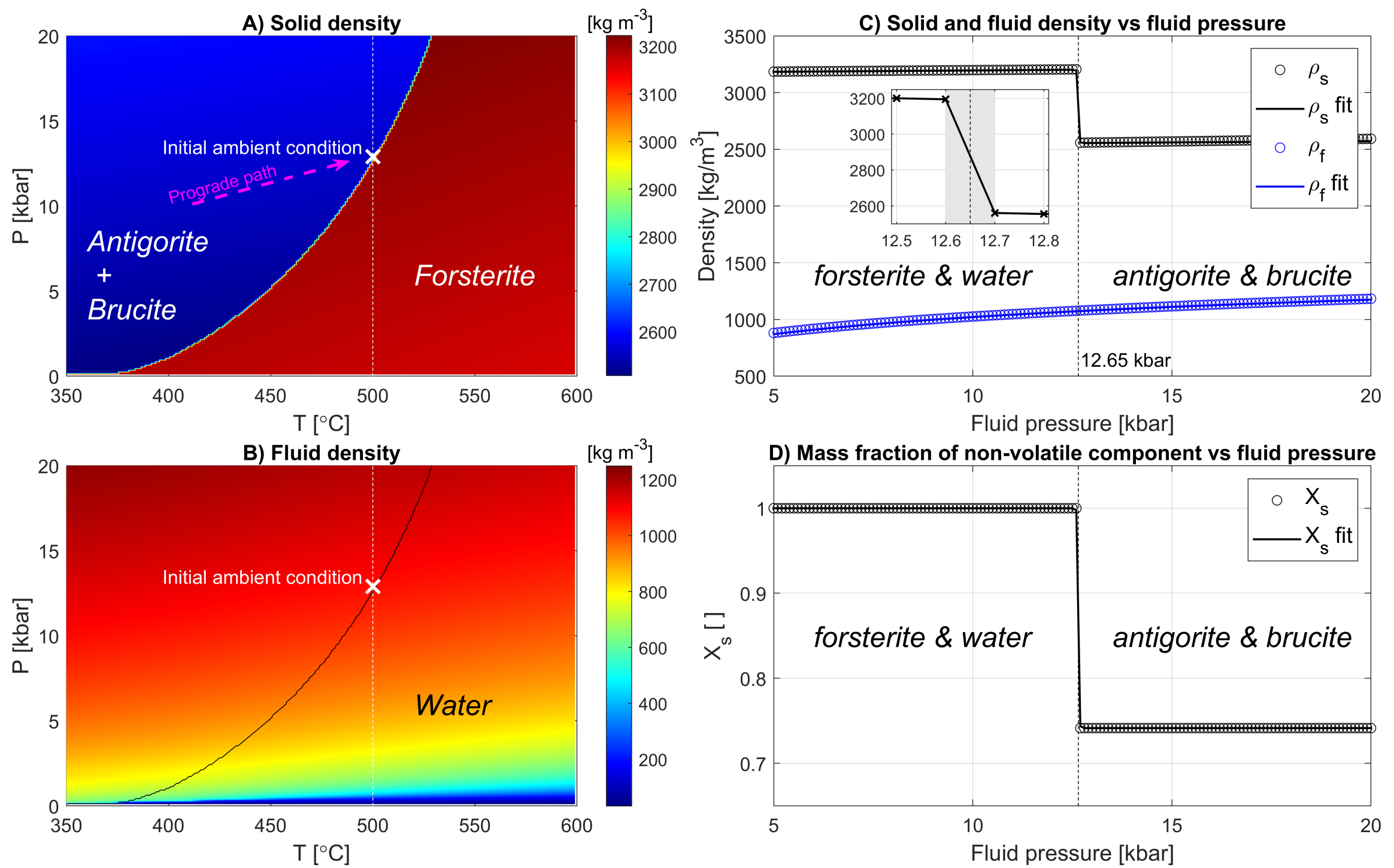
A) Solid density
[kg m-3]
3200
3100
3000
2900
2800
2700
2600
Initial ambient condition
Prograde path
Antigorite
+
Brucite
Forsterite
P [kbar]
T [°C]
C) Solid and fluid density vs fluid pressure
Density [kg/m3]
Fluid pressure [kbar]
ρs
ρs fit
ρf
ρf fit
forsterite & water
antigorite & brucite
12.65 kbar
B) Fluid density
[kg m-3]
1200
1000
800
600
400
200
Initial ambient condition
Water
D) Mass fraction of non-volatile component vs fluid pressure
Xs [ ]
Xs
Xs fit
forsterite & water
antigorite & brucite

Figure4.

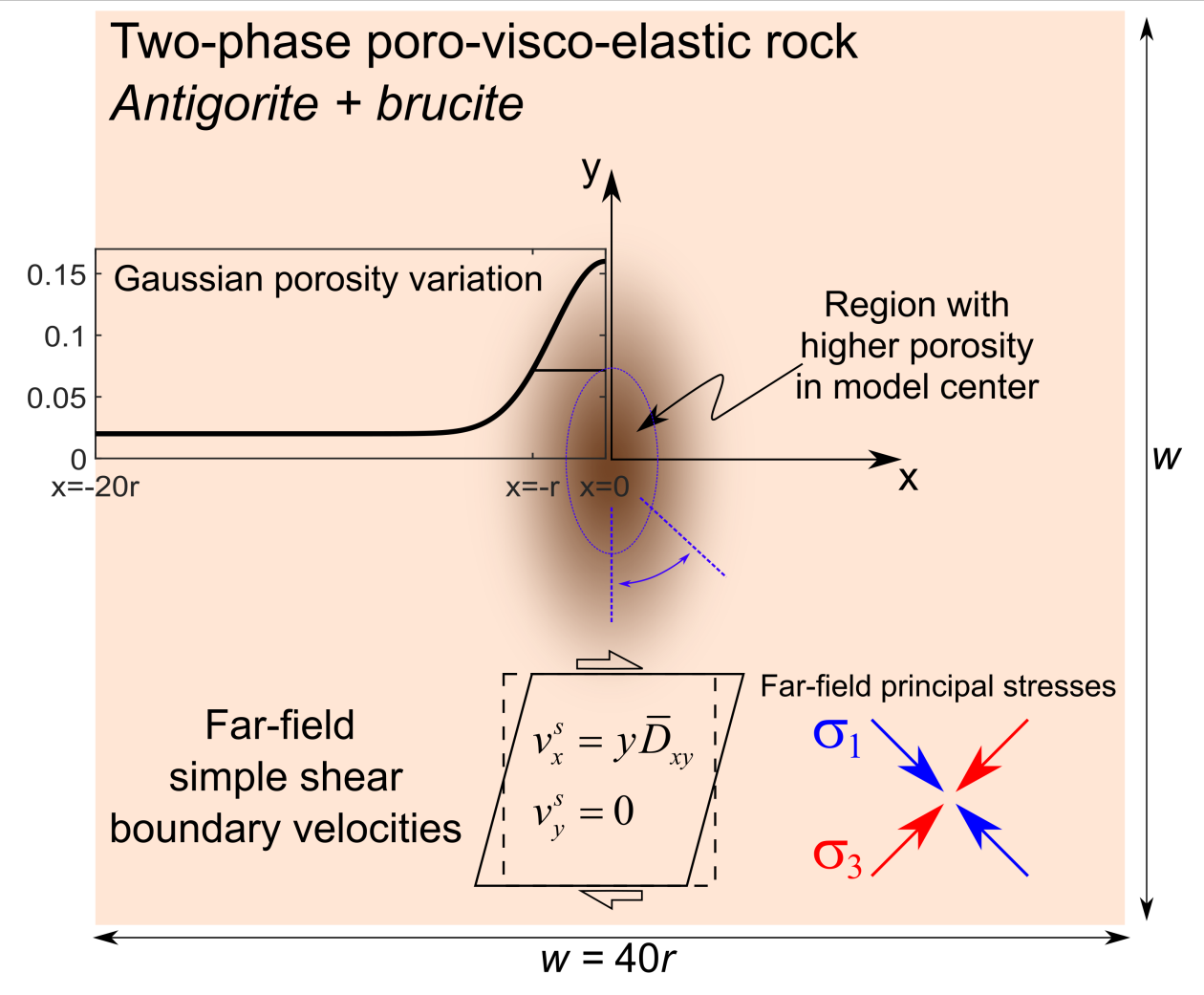
Two-phase poro-visco-elastic rock
Antigorite + brucite
y
Gaussian porosity variation
0.15
0.1
0.05
0
x=-20r
x=-r
x=0
x
Region with
higher porosity
in model center
w
Far-field
simple shear
boundary velocities
$v_x^s = y\bar{D}_{xy}$
$v_y^s = 0$
Far-field principal stresses
σ_1
σ_3
w = 40r

Figure5.

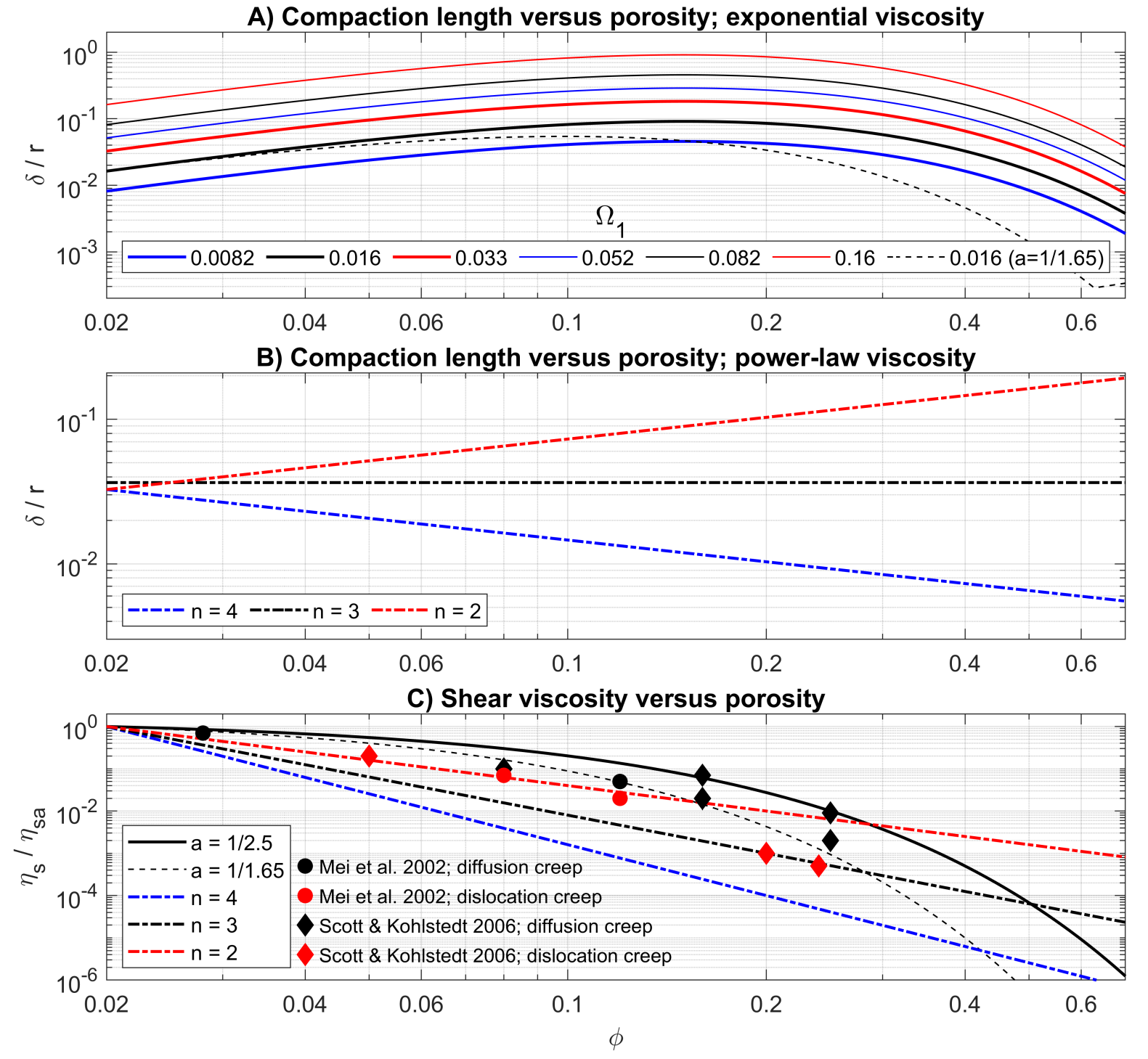
A) Compaction length versus porosity; exponential viscosity
δ / r
Ω1
0.0082
0.016
0.033
0.052
0.082
0.16
0.016 (a=1/1.65)
B) Compaction length versus porosity; power-law viscosity
δ / r
n = 4
n = 3
n = 2
C) Shear viscosity versus porosity
ηs / ηsa
a = 1/2.5
a = 1/1.65
n = 4
n = 3
n = 2
Mei et al. 2002; diffusion creep
Mei et al. 2002; dislocation creep
Scott & Kohlstedt 2006; diffusion creep
Scott & Kohlstedt 2006; dislocation creep
ϕ

Figure6.

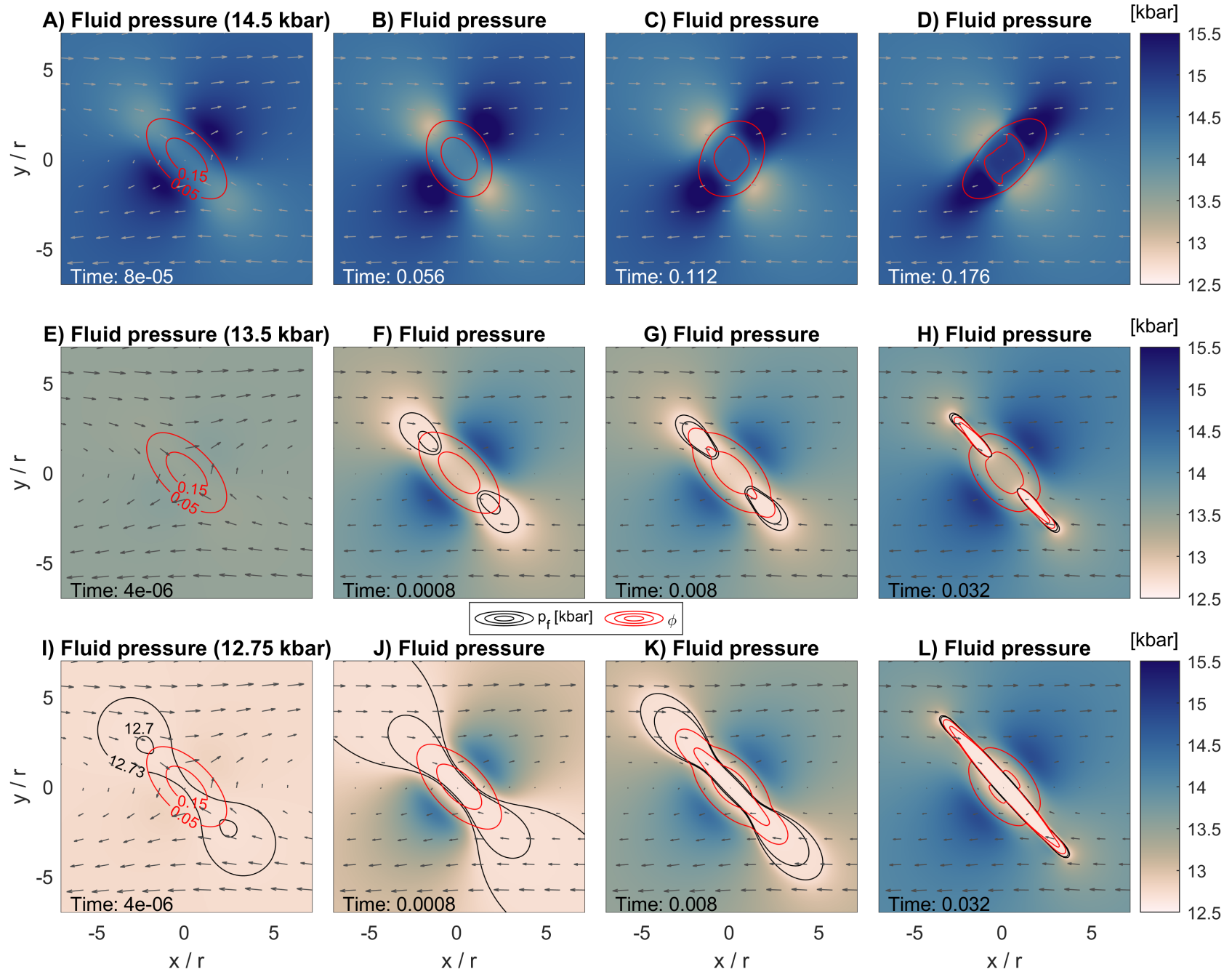
A) Fluid pressure (14.5 kbar)
B) Fluid pressure
C) Fluid pressure
D) Fluid pressure
[kbar]
15.5
15
14.5
14
13.5
13
12.5
y / r
5
0
-5
0.15
0.05
Time: 8e-05
Time: 0.056
Time: 0.112
Time: 0.176
E) Fluid pressure (13.5 kbar)
F) Fluid pressure
G) Fluid pressure
H) Fluid pressure
Time: 4e-06
Time: 0.0008
Time: 0.008
Time: 0.032
p_f [kbar]
ϕ
I) Fluid pressure (12.75 kbar)
J) Fluid pressure
K) Fluid pressure
L) Fluid pressure
12.7
12.73
x / r

Figure7.

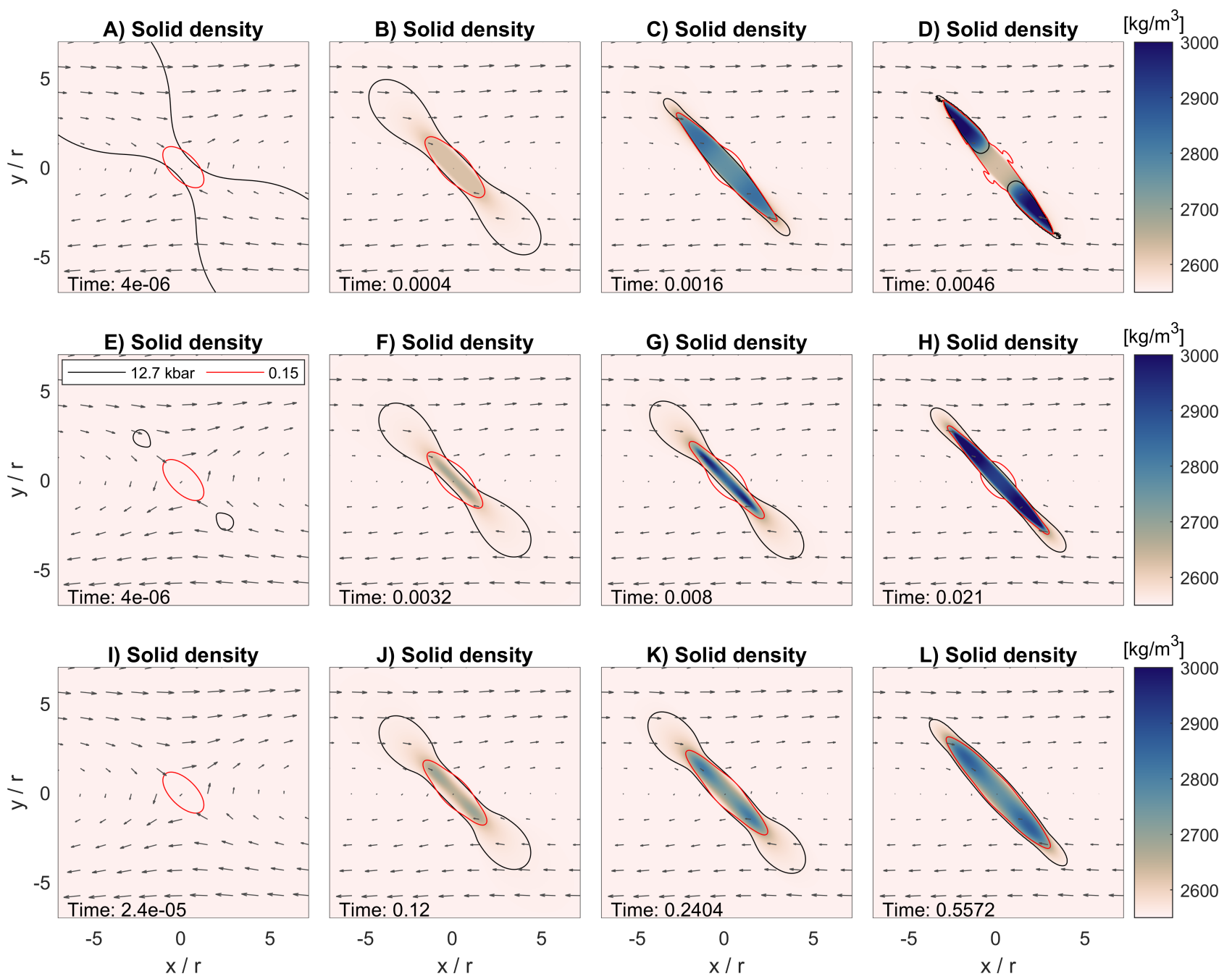
A) Solid density
B) Solid density
C) Solid density
D) Solid density
E) Solid density
F) Solid density
G) Solid density
H) Solid density
I) Solid density
J) Solid density
K) Solid density
L) Solid density
[kg/m3]
3000
2900
2800
2700
2600
12.7 kbar
0.15
Time: 4e-06
Time: 0.0004
Time: 0.0016
Time: 0.0046
Time: 4e-06
Time: 0.0032
Time: 0.008
Time: 0.021
Time: 2.4e-05
Time: 0.12
Time: 0.2404
Time: 0.5572
y / r
x / r
5
0
-5

Figure8.

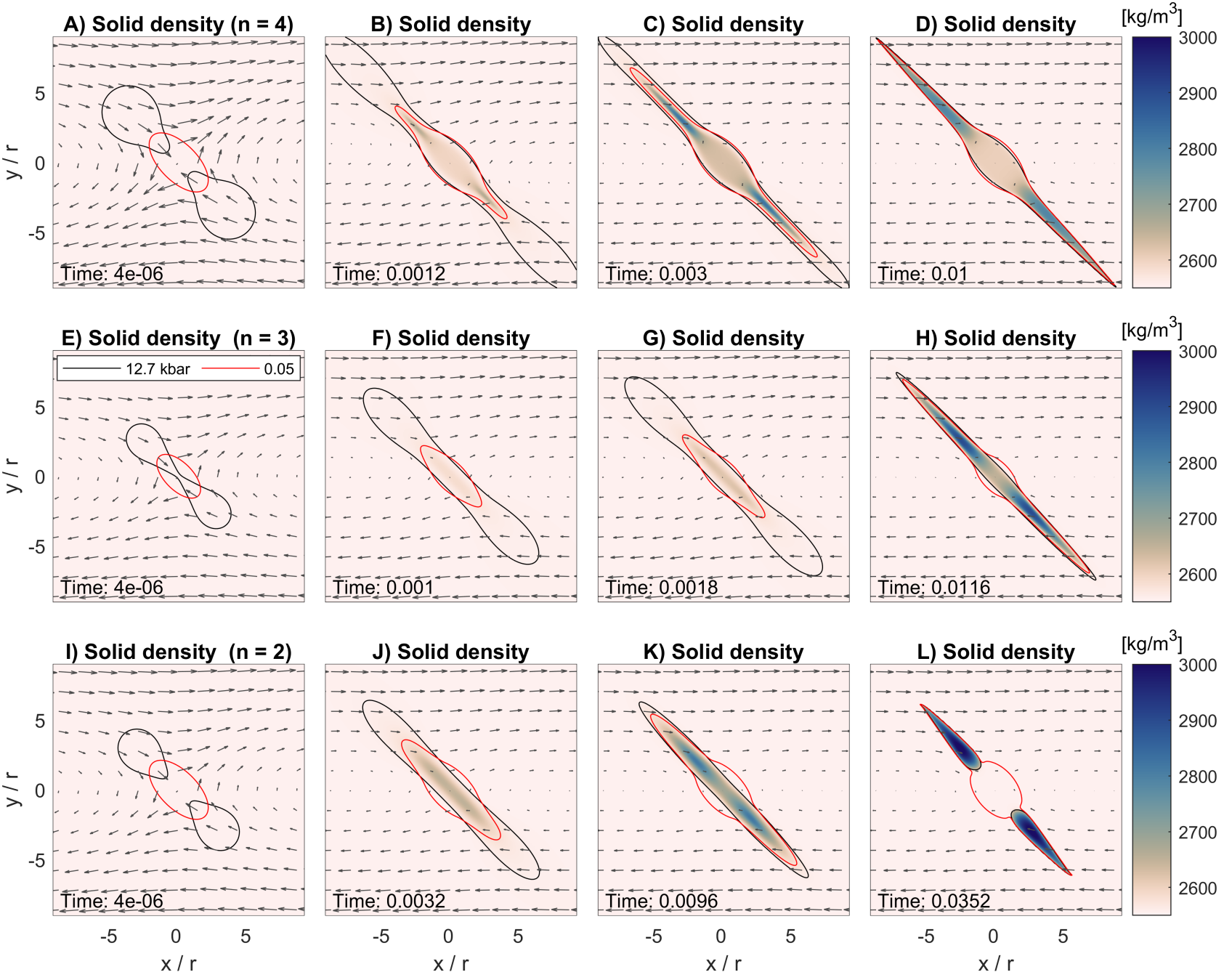
A) Solid density (n = 4)
B) Solid density
C) Solid density
D) Solid density
[kg/m3]
3000
2900
2800
2700
2600
y / r
5
0
-5
Time: 4e-06
Time: 0.0012
Time: 0.003
Time: 0.01
E) Solid density (n = 3)
12.7 kbar
0.05
F) Solid density
G) Solid density
H) Solid density
Time: 4e-06
Time: 0.001
Time: 0.0018
Time: 0.0116
I) Solid density (n = 2)
J) Solid density
K) Solid density
L) Solid density
Time: 4e-06
Time: 0.0032
Time: 0.0096
Time: 0.0352
x / r

Figure9.

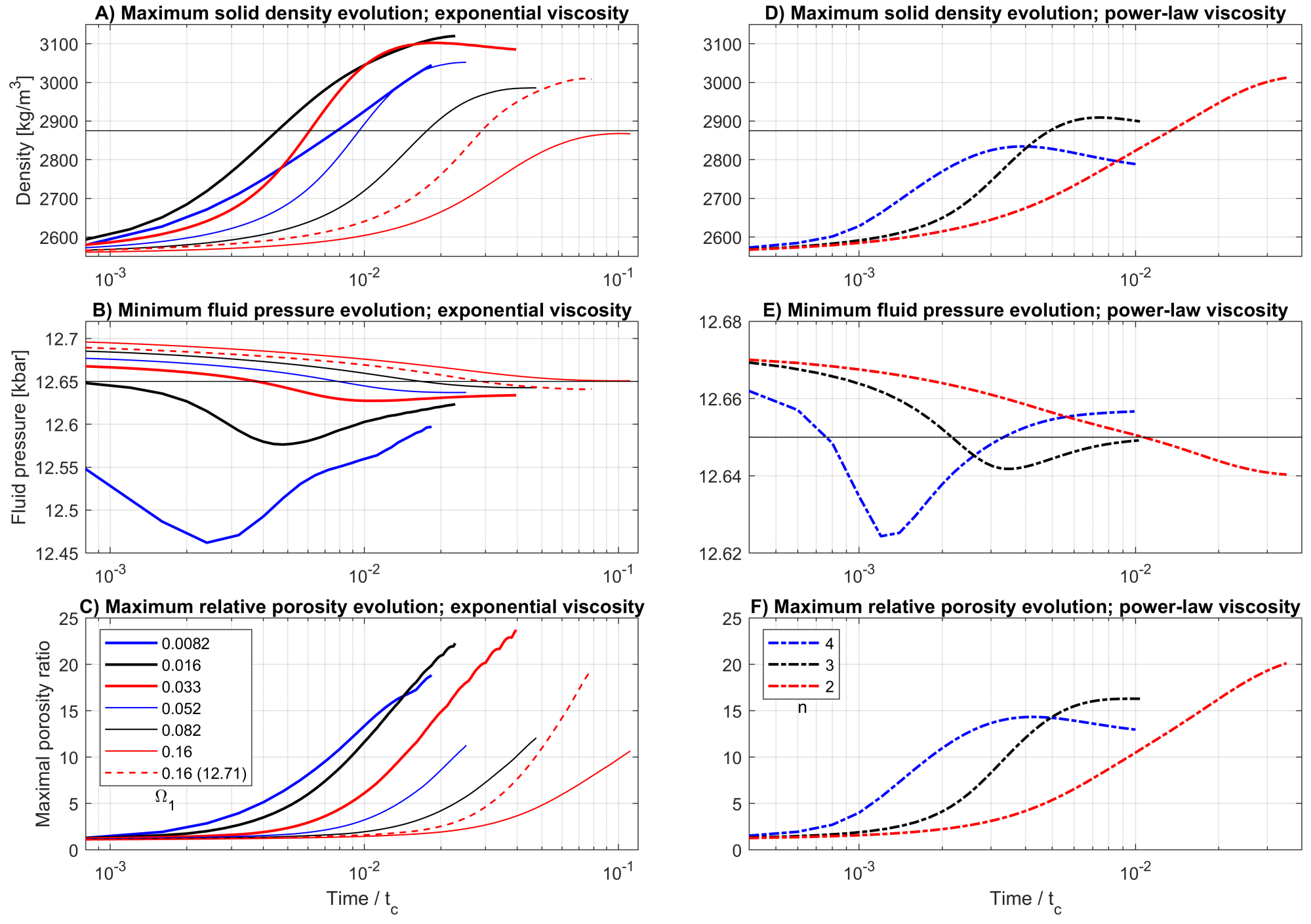
A) Maximum solid density evolution; exponential viscosity
Density [kg/m3]
3100
3000
2900
2800
2700
2600
10-3
10-2
10-1
D) Maximum solid density evolution; power-law viscosity
B) Minimum fluid pressure evolution; exponential viscosity
Fluid pressure [kbar]
12.7
12.65
12.6
12.55
12.5
12.45
E) Minimum fluid pressure evolution; power-law viscosity
12.68
12.66
12.64
12.62
C) Maximum relative porosity evolution; exponential viscosity
Maximal porosity ratio
25
20
15
10
5
0
0.0082
0.016
0.033
0.052
0.082
0.16
0.16 (12.71)
Ω1
Time / tc
F) Maximum relative porosity evolution; power-law viscosity
4
3
2
n

Figure10.

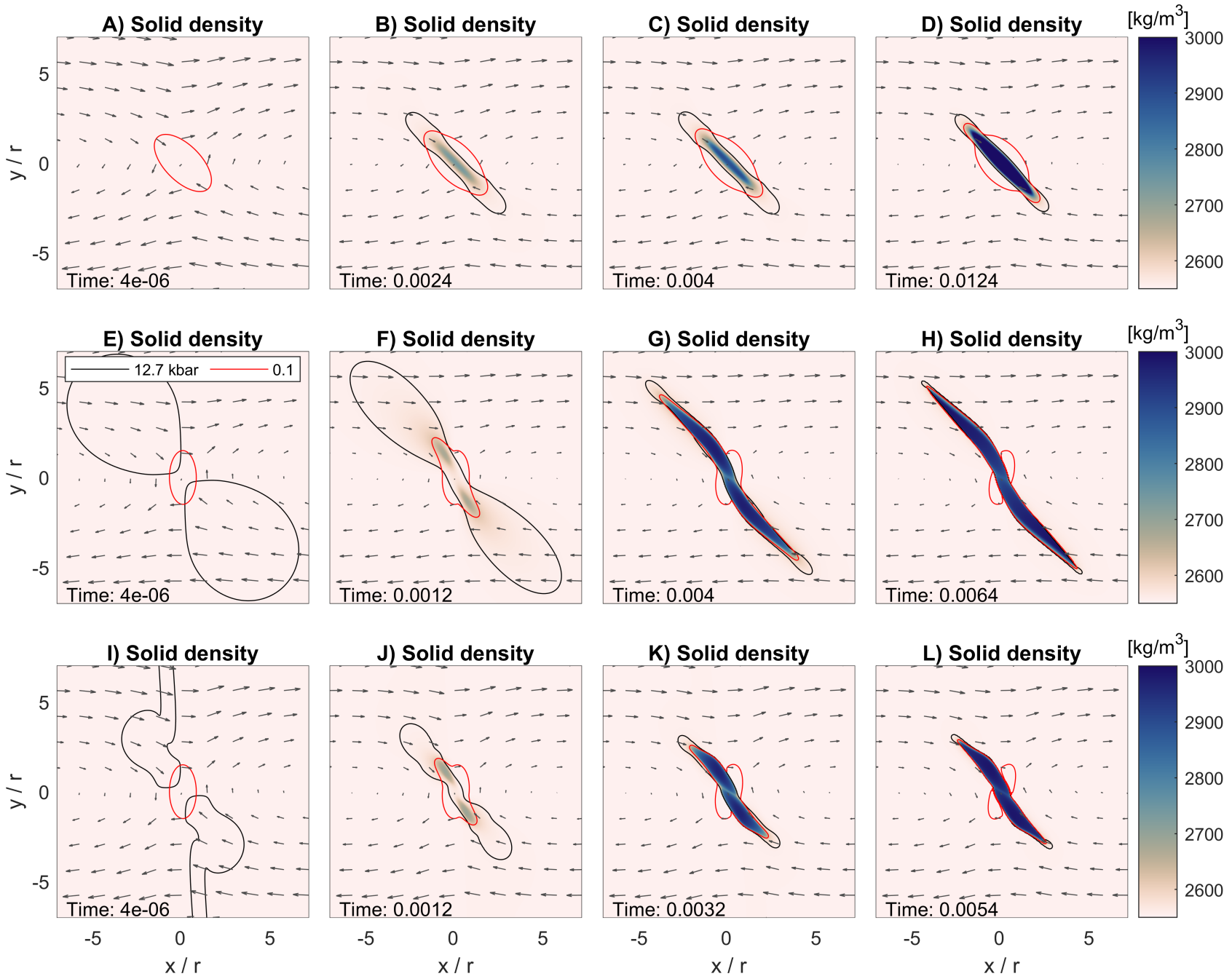
A) Solid density
B) Solid density
C) Solid density
D) Solid density
E) Solid density
F) Solid density
G) Solid density
H) Solid density
I) Solid density
J) Solid density
K) Solid density
L) Solid density
[kg/m3]
3000
2900
2800
2700
2600
12.7 kbar
0.1
Time: 4e-06
Time: 0.0024
Time: 0.004
Time: 0.0124
Time: 4e-06
Time: 0.0012
Time: 0.004
Time: 0.0064
Time: 4e-06
Time: 0.0012
Time: 0.0032
Time: 0.0054
y / r
x / r
5
0
-5

Figure11.

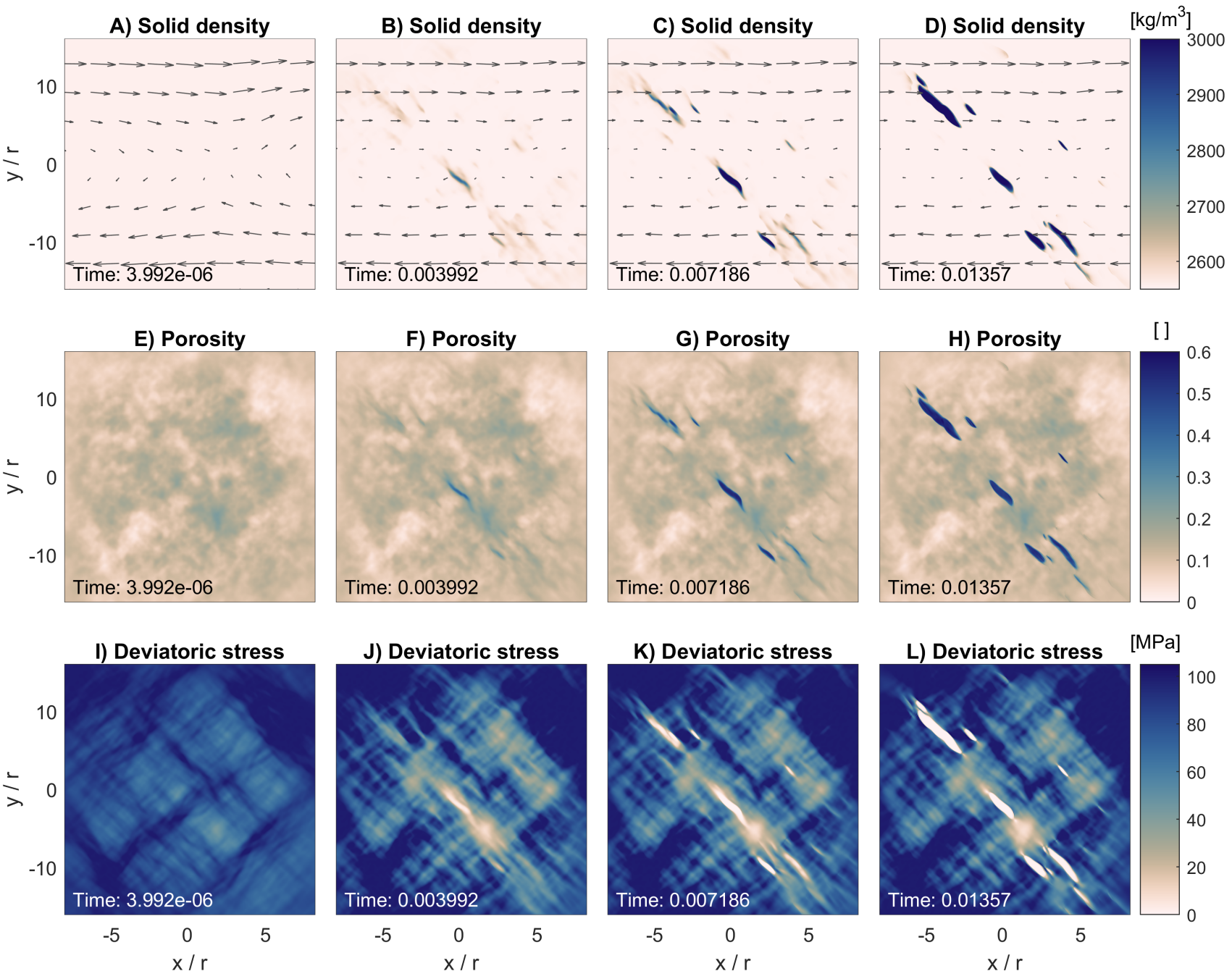
A) Solid density
B) Solid density
C) Solid density
D) Solid density
[kg/m3]
3000
2900
2800
2700
2600
Time: 3.992e-06
Time: 0.003992
Time: 0.007186
Time: 0.01357
E) Porosity
F) Porosity
G) Porosity
H) Porosity
[ ]
0.6
0.5
0.4
0.3
0.2
0.1
0
I) Deviatoric stress
J) Deviatoric stress
K) Deviatoric stress
L) Deviatoric stress
[MPa]
100
80
60
40
20
0
y / r
10
0
-10
x / r
-5
0
5

Figure12.

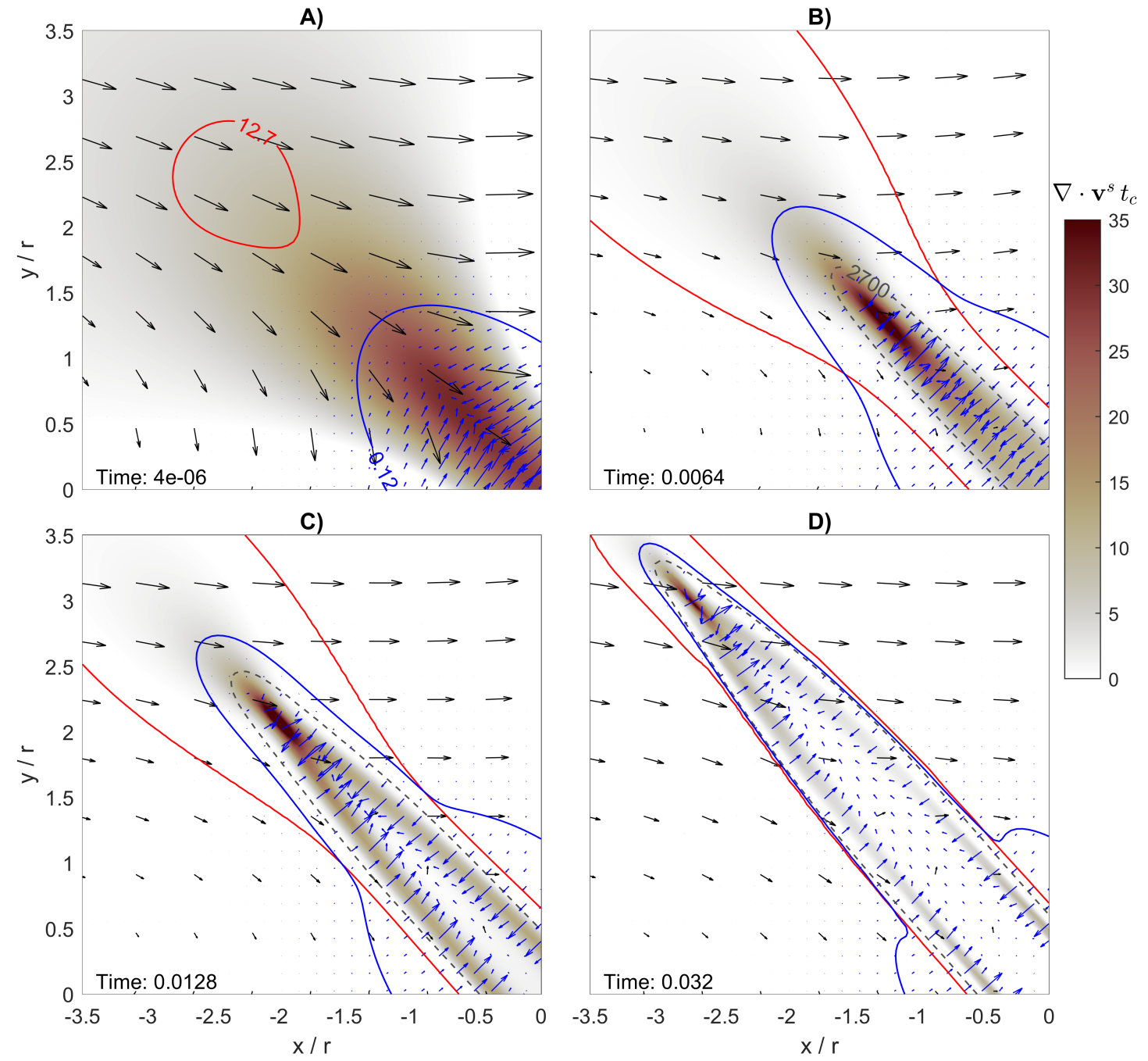
A)
B)
C)
D)
12.7
2700
Time: 4e-06
Time: 0.0064
Time: 0.0128
Time: 0.032
y / r
x / r
$\nabla \cdot \mathbf{v}^s \, t_c$
35
30
25
20
15
10
5
0
3.5
3
2.5
2
1.5
1
0.5
0
-3.5
-3
-2.5
-2
-1.5
-1
-0.5
0

Figure13.

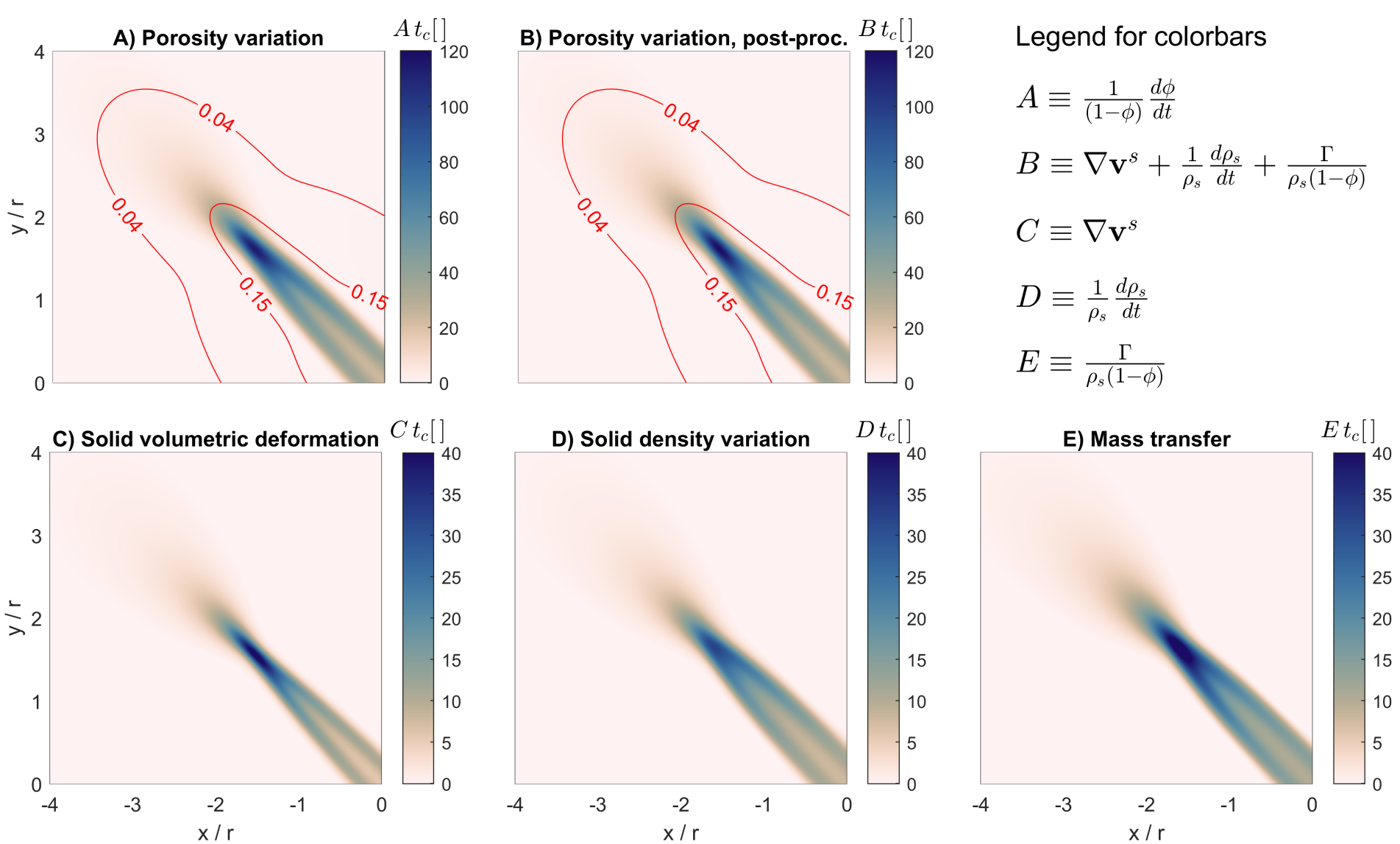
A) Porosity variation
$A\,t_c[\,]$
B) Porosity variation, post-proc.
$B\,t_c[\,]$
C) Solid volumetric deformation
$C\,t_c[\,]$
D) Solid density variation
$D\,t_c[\,]$
E) Mass transfer
$E\,t_c[\,]$
0.04
0.15
y / r
x / r
Legend for colorbars
$A \equiv \frac{1}{(1-\phi)}\frac{d\phi}{dt}$
$B \equiv \nabla \mathbf{v}^s + \frac{1}{\rho_s}\frac{d\rho_s}{dt} + \frac{\Gamma}{\rho_s(1-\phi)}$
$C \equiv \nabla \mathbf{v}^s$
$D \equiv \frac{1}{\rho_s}\frac{d\rho_s}{dt}$
$E \equiv \frac{\Gamma}{\rho_s(1-\phi)}$

Figure14.

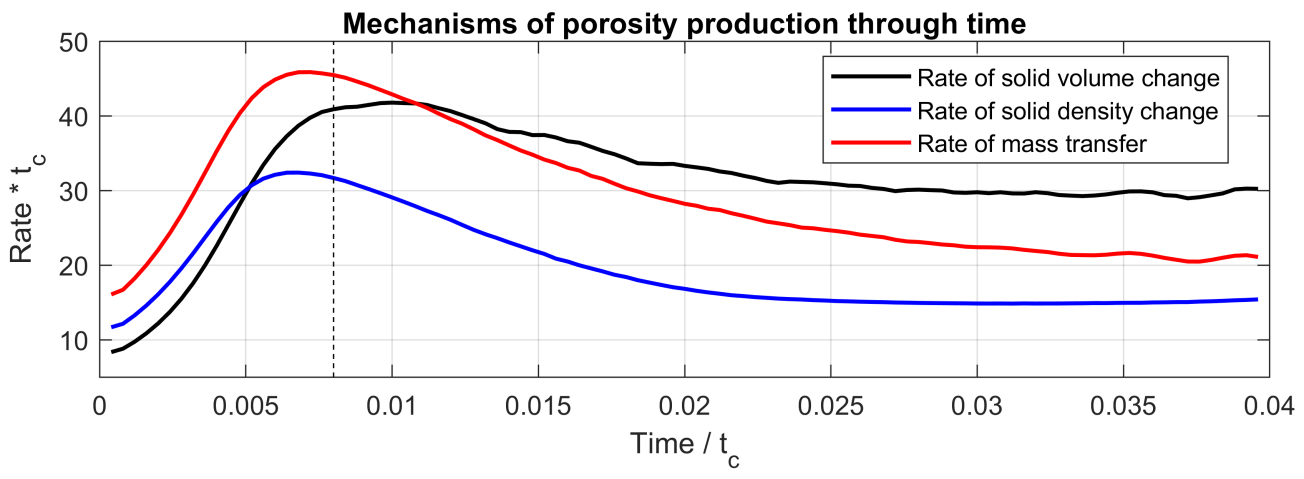
Mechanisms of porosity production through time
Rate of solid volume change
Rate of solid density change
Rate of mass transfer
Rate * t_c
Time / t_c
50
40
30
20
10
0
0.005
0.01
0.015
0.02
0.025
0.03
0.035
0.04

Figure15.

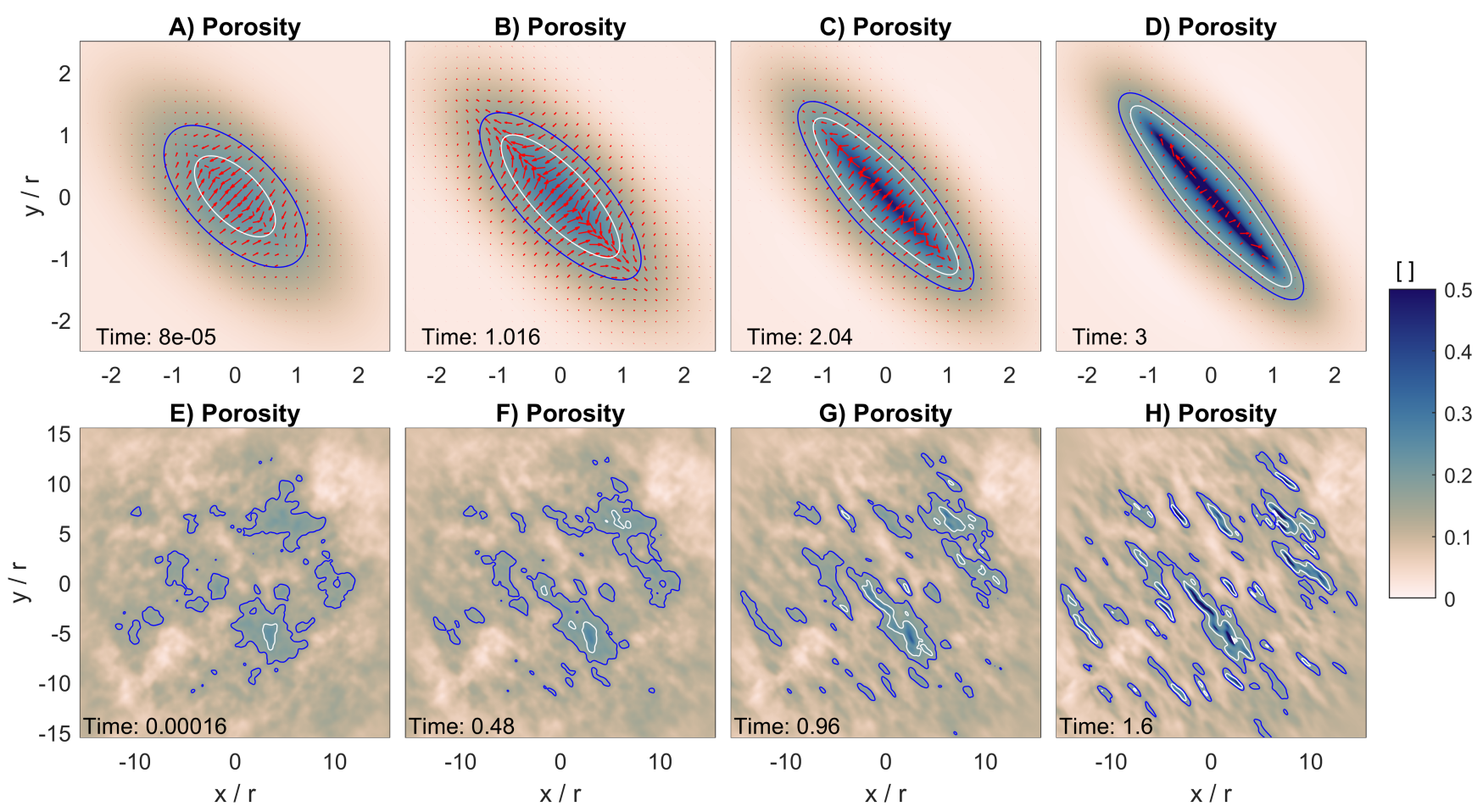
A) Porosity
B) Porosity
C) Porosity
D) Porosity
E) Porosity
F) Porosity
G) Porosity
H) Porosity
Time: 8e-05
Time: 1.016
Time: 2.04
Time: 3
Time: 0.00016
Time: 0.48
Time: 0.96
Time: 1.6
y / r
x / r
[ ]
0.5
0.4
0.3
0.2
0.1
0

FigureA1.

Initial configuration

Time loop

PT iteration loop

Calculate equilibrium densities and mass fraction.	$\rho_f = 1194 \ln\left(\frac{p_f}{p_{ini}} + 1\right)^{1/3.5}$ $\rho_s^{EQ} = -\tanh\left(600\frac{p_f - p_R}{p_{ini}}\right)323.32 + 2848 + \left(\frac{p_f}{p_{ini}} - 0.0078\right)30.4762$ $X_s^{EQ} = -\tanh\left(600\frac{p_f - p_R}{p_{ini}}\right)0.1292 + 0.8707$
Kinetics: Calculate solid density and mass fraction.	$\frac{\partial \rho_s}{\partial t} = \frac{\rho_s^{EQ} - \rho_s}{t_{kin}}$ $\frac{\partial X_s}{\partial t} = \frac{X_s^{EQ} - X_s}{t_{kin}}$
Calculate fluid pressure.	$\frac{\Delta^{PT} p_f}{\Delta t_{pf}^{PT}} = -\frac{\partial \rho_T}{\partial t} + \nabla \cdot \left[\rho_f \frac{k\phi^3}{\eta_f} \nabla p_f\right] - \nabla \cdot \left(\rho_T \mathbf{v}^s\right)$
Calculate porosity.	$\frac{\Delta^{PT} \phi}{\Delta t_{\varphi}^{PT}} = \frac{\partial}{\partial t}\left[\rho_X (1-\phi)\right] + \nabla \cdot \left[\rho_X (1-\phi)\mathbf{v}^s\right]$
Calculate total pressure.	$\frac{\Delta^{PT} p}{\Delta t_p^{PT}} = -\nabla \cdot \mathbf{v}^s - \frac{1}{K_d}\left(\frac{dp}{dt} - \alpha \frac{dp_f}{dt}\right) - \frac{p - p_f}{(1-\phi)\lambda}$
Calculate total stresses.	$\sigma_{ij} = -p + 2\eta_s(\phi)\left[\frac{1}{2}\left(\frac{\partial v_i^s}{\partial x_j} + \frac{\partial v_j^s}{\partial x_i}\right) - \delta_{ij}\frac{1}{3}\frac{\partial v_k^s}{\partial x_k}\right]$
Calculate solid velocities.	$\frac{\Delta^{PT} v_i^s}{\Delta t_v^{PT}} = \nabla \cdot \sigma_{ij}$

FigureA2.

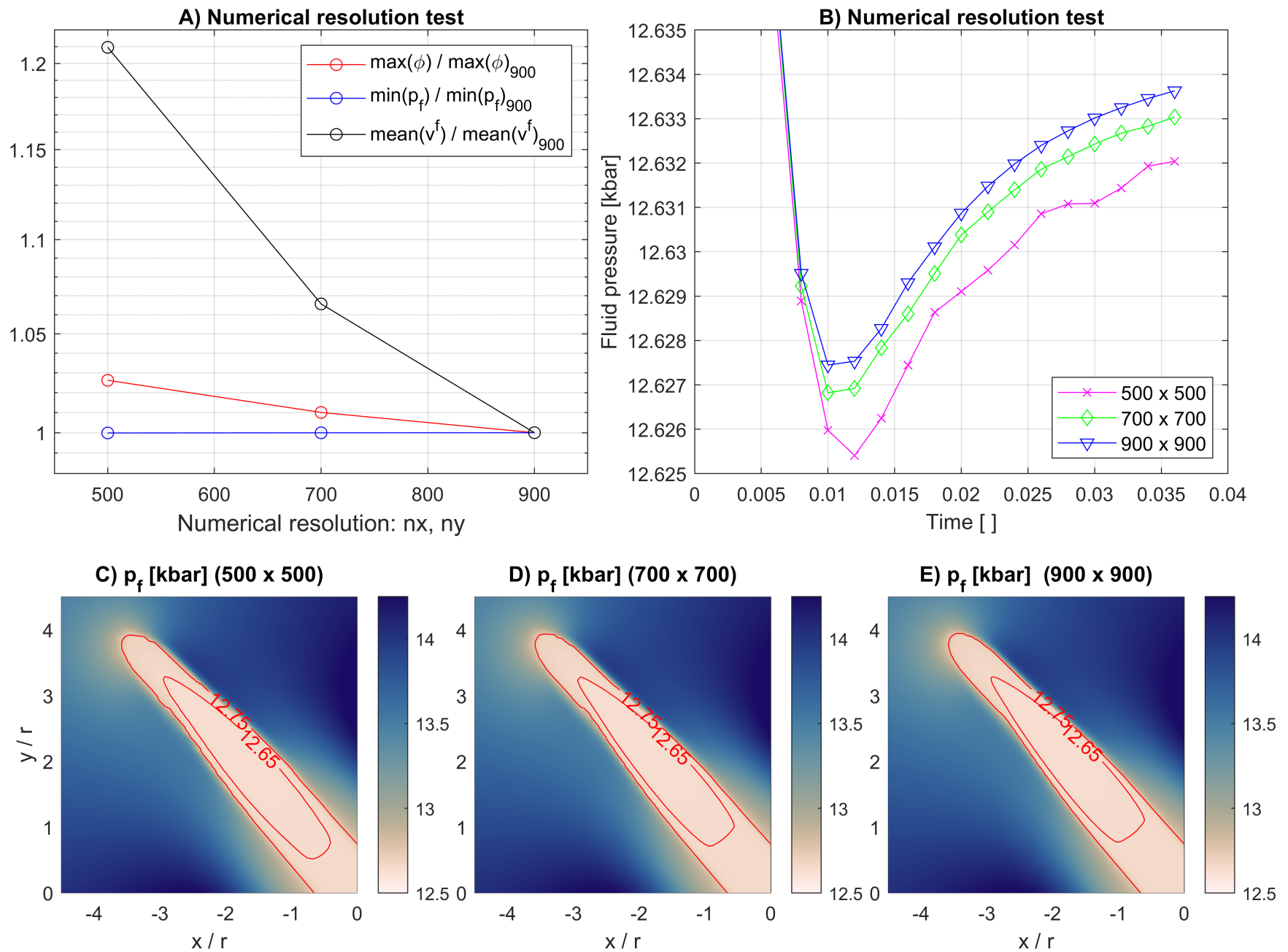
A) Numerical resolution test
max(ϕ) / max(ϕ)900
min(pf) / min(pf)900
mean(vf) / mean(vf)900
Numerical resolution: nx, ny
B) Numerical resolution test
Fluid pressure [kbar]
Time [ ]
500 x 500
700 x 700
900 x 900
C) pf [kbar] (500 x 500)
D) pf [kbar] (700 x 700)
E) pf [kbar] (900 x 900)
12.5
12.65
y / r
x / r

FigureA3.

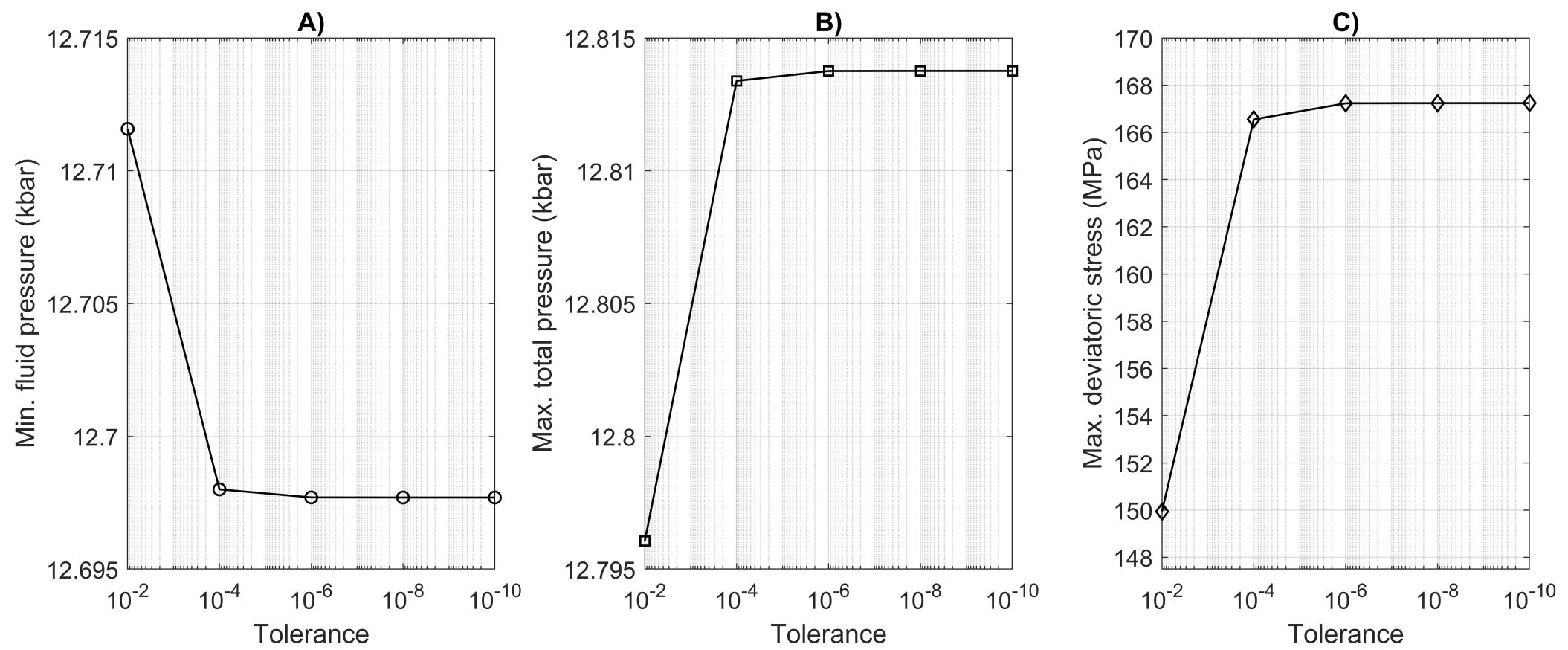
A)
B)
C)
Min. fluid pressure (kbar)
Max. total pressure (kbar)
Max. deviatoric stress (MPa)
Tolerance
Tolerance
Tolerance
12.715
12.71
12.705
12.7
12.695
12.815
12.81
12.805
12.8
12.795
170
168
166
164
162
160
158
156
154
152
150
148
10^{-2}
10^{-4}
10^{-6}
10^{-8}
10^{-10}